The Dissertation Committee for Georgios Stamokostas
certifies that this is the approved version of the following dissertation:

Theoretical studies of local moment magnetism with strong spin-orbit coupling

Committee:

Gregory A. Fiete, Supervisor

Allan H. Macdonald

Qian Niu

Jianshi Zhou

Theoretical studies of local moment magnetism with strong spin-orbit coupling

by

Georgios Stamokostas

DISSERTATION

Presented to the Faculty of the Graduate School of

The University of Texas at Austin

in Partial Fulfillment

of the Requirements

for the Degree of

DOCTOR OF PHILOSOPHY

THE UNIVERSITY OF TEXAS AT AUSTIN

December 2017

Στον Άγιο Παΐσιο, and to science.

Acknowledgments

I would like to thank my supervisor Gregory A. Fiete for working with me all these years and "building" me slowly from student to researcher. I would also like to thank my fellow Ph.D. student Panteleimon Lapas for the challenging questions that we were constantly posing to each other, which gave useful feedback for the progress of our work, and to my officemate Pontus Laurell for fruitful discussions as well. Also, to the staff of the university of Texas at Austin, Matt Erwin and Michele Landfield of the center of complex quantum systems, that helped me to everything I needed all these years. Furthermore, I would like to thank all these people that were always next to me, my father Lampros, my mother Manto, my brother Sotiris, my friends in USA, Manos Chatzopoulos, and Giannis Keramidas, Lucy Sharp, my undergrad friends Leonardos Gouvelis, and Giannis Gennarakis who shared together the same enthusiasm about physics.

This research was supported in part by National Science Foundation (NSF) grants DMR-1507621, MRSEC DMR-1720595 and from ARO grant W911NF-14-1-0579.

Theoretical studies of local moment magnetism with strong spin-orbit coupling

Publication No. _____

Georgios Stamokostas, Ph.D.
The University of Texas at Austin, 2017

Supervisor: Gregory A. Fiete

We study the magnetic and lattice contributions to the thermal conductivity of electrically insulating strongly spin-orbit coupled magnetically ordered phases on a two-dimensional honeycomb lattice using the Kitaev-Heisenberg model. Depending on model parameters, such as the relative strength of the spin-orbit induced anisotropic coupling, a number of magnetically ordered phases are possible. We study two distinct regimes of thermal transport depending on whether the characteristic energy of the phonons or the magnons dominates, and focus on two different relaxation mechanisms, boundary scattering and magnon-phonon scattering. For spatially anisotropic magnetic phases, the thermal conductivity tensor can be highly anisotropic when the magnetic energy scale dominates, since the magnetic degrees of freedom dominate the thermal transport for temperatures well below the magnetic transition temperature. In the opposite limit in which the phonon energy scale dominates, the thermal conductivity will be nearly isotropic, reflecting the

isotropic (at low temperatures) phonon dispersion assumed for the honeycomb lattice. We further discuss the extent to which thermal transport properties are influenced by strong spin-orbit induced anisotropic coupling in the local moment regime of insulating magnetic phases. The developed methodology can be applied to any 2D magnon-phonon system, and more importantly to systems where an analytical Bogoliubov transformation cannot be found and magnon bands are not necessarily isotropic.

Furthermore, using exact diagonalization, we study the spin-orbit coupling and interaction- induced mixing between t_{2g} and e_g d-orbital states in a cubic crystalline environment, as commonly occurs in transition metal oxides. We make a direct comparison with the widely used t_{2g} only or e_g only model, depending on electronic filling. We consider all electron fillings of the d-shell and compute the total magnetic moment, the spin, the occupancy of each orbital, and the effective spin-orbit coupling strength (renormalized through interaction effects) in terms of the bare interaction parameters, spin-orbit coupling, and crystal field splitting, focusing on the parameter ranges relevant to 4d and 5d transition metal oxides. In various limits we provide perturbative results consistent with our numerical calculations. We find that the t_{2g}-e_g mixing can be large, with up to 20% occupation of orbitals that are nominally "empty", which has experimental implications for the interpretation of the branching ratio in experiments, and can impact the effective local moment Hamiltonian used to study magnetic phases and magnetic excitations in transition metal oxides. Our results can aid the theoretical interpretation

of experiments on these materials, which often fall in a regime of intermediate coupling with respect to electron-electron interactions.

Table of Contents

List of Figures

Chapter 1

Introduction

In recent years, the intense research activity around topological insulators [77, 34, 83, 8] has drawn increased attention to the influence of spin-orbit coupling in the solid state, and demonstrated that qualitatively new phases of band insulators can appear.[13, 12, 43, 42] In the limit of strong electron-electron interactions, spin-orbit coupling can also have a profound influence on the phase diagram of Hamiltonians potentially relevant to correlated topological materials.[68] In the context of correlated materials with strong spin-orbit coupling, transition metal oxides containing iridium atoms, known as iridates, have been a focus of research.[44, 46, 81, 89, 107, 31, 108, 105, 85, 1] In particular, unusual magnetic orders have been suggested in a number of them.[84, 45, 86, 17, 40, 16, 48, 52, 91, 84, 110, 51, 36, 72, 41, 57, 63, 87, 25, 59] The studies we focus in this dissertation is in part motivated by theoretical work on iridates.

Another area in which spin-orbit coupling has played a leading role is spintronics,[26, 101, 38] where the coupling of spin and orbital motion allows for an electrical detection of spin properties. Spintronic devices offer the possibility of low-power components of computing elements, and may also exhibit

longer coherence times than conventional devices, which may prove useful for quantum architectures.[33] In spin caloritronic devices the additional element of a thermal gradient is included and the relationship between thermal gradients, spin currents, and spin-orbit induced voltages is investigated.[5, 2, 102]

In this work, in chapter 2, we focus on the thermal transport properties of a 2D strong spin-orbit driven magnetic insulator. In these systems, the thermal transport is dominated (at low temperatures) by magnetic and lattice excitations that carry heat. We study these systems using local moment models that are coupled to phonons (lattice distortions) through exchange constants that depend on the relative distance between nearby moments. The main role of the spin-orbit coupling is to induce unusual, and sometimes highly spatially anisotropic magnetic orders. The thermal transport is computed within the Boltzmann approach (in the relaxation time approximation) which takes as inputs the magnon spectrum of the various magnetic orders, and the phonon spectrum of the underlying lattice. For concreteness, we focus on a well-known two-dimensional model, the so-called Heisbenberg-Kitaev (HK) model,[16, 17, 90, 41] on the honeycomb lattice. The HK model has a rich, established magnetic phase diagram that provides a useful starting point for investigating the magnetic fluctuations within the $1/S$ expansion, where S is the magnitude of the local moment.[10] Previous studies of thermal transport in insulating magnetic materials indicated that the magnetic and thermal contributions to the thermal conductivity can be comparable.[27, 65, 74, 75, 21, 22] Our main result in this work is to show that the spatially anisotropic magnetic

states that can arise from strong spin-orbit coupling can dramatically affect the thermal transport, or have a rather small effect depending on the relative size of magnon and phonon thermal conductivities. In some cases, the thermal transport may help identify the symmetries of the magnetically ordered state if other measurements are difficult or problematic.

An other reason that transition metal oxides have undergone intensive study, is because of their remarkably rich phase diagrams and sensitivity to external fields, strain, disorder, and doping.[11, 64, 100, 30] High-temperature superconductors (e.g., cuprates) and colossal magnetoresistance materials (e.g., manganites) are two notable examples, but both of these have light transition elements drawn from the 3d series.[69, 39] On the other hand, as mentioned earlier, the study of topological insulators has brought attention to the importance of large spin-orbit coupling in general. As a result, some focus has shifted to the heavier transition metals from the 4d and 5d series, which have significantly enhanced spin-orbit coupling relative to those in the 3d series.[107, 85, 88]

Iridates, that were mentioned above, in particular, have undergone much theoretical and experimental study.[107, 85, 88] However, in some of the iridates even the nature of the conventional order, such as the magnetic order (and the underlying microscopic spin Hamiltonian), is not easy to determine,[16, 41, 57, 97, 6, 106, 14, 20, 91] in part due to the large neutron absorption cross-section which makes neutron scattering experiments challenging.[23] An experimental tool known as resonant inelastic X-ray scat-

tering (RIXS) is particularly well suited to studies of the iridates.[7, 60, 32, 67, 79, 55, 78] While there is some understanding of the microscopic details revealed in the RIXS signal, the theory is still under development.[3] Our work in chapter 3 will facilitate that development.

A further challenge to understanding the iridates and other 4d/5d transition metal oxides is that the materials fall into a regime of comparable energy scales where it is difficult to argue *a priori* that a particular term in the Hamiltonian is small compared to the others: The typical kinetic energy, interaction energies, Hund's coupling, spin-orbit coupling, and crystal field splitting are all on the scale of an electron volt.[107, 85, 88] With respect to theoretical analysis, this means it is not clear if one should approach the iridates from a weak-coupling band-like description in which correlations are included within the band description,[37, 19, 113, 114, 105] or from the strong-coupling limit in which a local moment model[36, 50, 76, 56, 80, 96, 73, 111, 62] is natural to describe the various types of magnetic orders that typically occur in the 4d/5d transition metal oxides (characteristic magnetic transition temperatures are on the order of 100K).[107, 85, 88] In this work, in chapter 3, we start from an atomic limit of the transition metal ions and treat the interaction effects non-pertubatively using exact diagonalization. In this way, we are able to work within an intermediate regime that reduces to a tight-binding-type Hamiltonian (for multiple ions) in the limit of vanishing interactions and a local moment model in the limit of strong interactions.

In a large class of transition metal oxides, the local oxygen environment

of the transition metal ions is an octahedral cage (see Fig. 3.1) that produces a cubic environment that splits the d-orbitals into a lower lying triply degenerate t_{2g} set of orbitals and a higher lying doubly-degenerate e_g set of orbitals. A feature that is shared by nearly all weak (aside from *ab initio* studies) *and* strong-coupling theoretical studies of the heavy transition metal oxides is that they assume the t_{2g}-e_g mixing is negligible.[36, 50, 76, 56, 80, 96, 73, 111, 62] In addition, many theoretical studies motivated by the iridates assume the infinite spin-orbit coupling limit which splits the t_{2g} orbitals into a total angular moment $J_{\text{eff}} = 3/2$ and $J_{\text{eff}} = 1/2$ set of states (that do not mix). For iridates with a nominal d-shell filling of 5 electrons, this results in a half-filled $J_{\text{eff}} = 1/2$ band, and thus reduces the Hamiltonian to a one-band model that often helps theoretical studies that rely on methods developed in the context of the cuprates.

In chapter 3, we revisit the assumption of negligible t_{2g}-e_g mixing and study the single ion limit in detail using exact diagonalization that allows a non-perturbative treatment of interaction effects. We consider all d-shell fillings and find the neglect of t_{2g}-e_g mixing is not in general justified, with the greatest mixing occurring for fillings of 5,6, and 7 electrons. Our work has implications for the interpretation of RIXS and X-ray absorption spectroscopy (XAS) data for the heavier elements with strong spin-orbit coupling, and the spectra of transition metal ions in oxides more generally. Our work can also be used as a more realistic starting point for determining the best form of the magnetic interactions between two nearby ions: Exchange interactions,

exchange anistropies, and the size of local moments differ as a consequence of t_{2g}-e_g mixing.

Finally in chapter 4, we summarized the main results of this work, and we provide some possible routes for further study.

Chapter 2

Thermal conductivity of local moment models with strong spin-orbit coupling

This chapter is organized as follows.[1] In Sec.2.1 we introduce the local moment model we study, and describe how the phonons are incorporated into the exchange constants of the model. In Sec.2.2 the magnon spectrum for various ordered phases of the local moment model is computed, which will be used as an input for the thermal conductivity. In Sec.2.3 the magnon and phonon scattering rates are computed, and in Sec.2.4 we present the results for the thermal conductivity in various regimes and for various phases of our model. The main conclusions are left to be summarized all together in chapter 4, whereas several lengthy technical details are relegated to the appendices.

2.1 Model Hamiltonian

We consider a total Hamiltonian for local moments coupled to the lattice as $\hat{\mathcal{H}} = \hat{\mathcal{H}}^{\text{spin}} + \hat{\mathcal{H}}^{\text{pho}}$, where the coupling between spin and lattice (phonon) degrees of freedom will be made explicit below. We study a local moment

[1] This chapter is based on the published paper: Phys. Rev. B 95, 064410 (2017) [93]. G. A. Fiete suggested the project, and G. Stamokostas and P. Lapas performed the calculations.

model with an established phase diagram, the Heisenberg-Kitaev (HK) model defined on a two-dimensional honeycomb lattice with nearest neighbor (NN) interactions:[16, 17, 90, 41]

$$\hat{\mathcal{H}}^{\text{spin}} = \sum_{\langle i,j \rangle} \hat{H}_{ij}^{(\gamma)} = \sum_{\langle i,j \rangle} \Big(J_{ij} \mathbf{S}_i \cdot \mathbf{S}_j + 2K_{ij} S_i^{\gamma} S_j^{\gamma} \Big), \tag{2.1}$$

where $\gamma = \{x, y, z\}$ labels the three distinct types of NN bonds, as shown in Fig.2.1, i and j label sites of the lattice, and S_i^{γ} is the γ^{th} component of the local moment on site i. The first term in Eq.(2.1) describes a Heisenberg interaction between nearest-neighbor spins and the second term is the so-called "Kitaev" term [58] that describes bond-direction-dependent anisotropic spin interactions. One may view it as originating from an underlying spin-orbit coupling.[45] The exchange constants, J_{ij} and K_{ij} describe the relative strengths of the Heisenberg and Kitaev terms respectively.

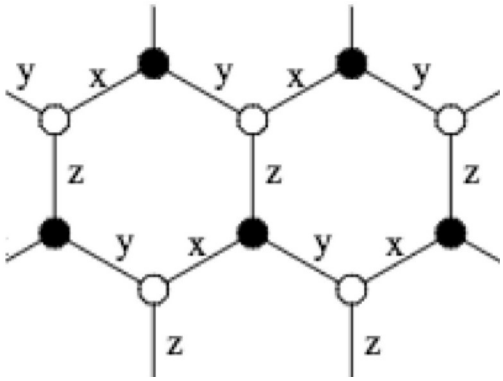

Figure 2.1: Honeycomb lattice with bond labels, $\gamma = \{x, y, z\}$, used for the Kitaev terms in Eq.(2.1).

The HK Hamiltonian of Eq.(2.1), using $A = \sqrt{K^2 + J^2}$ (where K and J are the magnitudes of the nearest neighbor Kitaev and Heisenberg exchange

couplings), can be expressed in terms of a parameter φ such that $K = A\sin\varphi$, $J = A\cos\varphi$ and $\varphi \in [0, 2\pi]$, as[17]

$$\hat{\mathcal{H}}^{\text{spin}} = \sum_{\langle i,j \rangle} A(\cos\varphi \mathbf{S}_i \cdot \mathbf{S}_j + 2\sin\varphi S_i^\gamma S_j^\gamma), \tag{2.2}$$

and its phase diagram is shown in Fig.2.2. For fixed A (which sets an overall energy scale), there are a wide range of magnetic (and non-magnetic spin-liquid) phases. In this work, we focus on the ferromagnetic, Néel, stripy, and zig-zag phases. The presence of the Kitaev couplings additionally renders the low energy magnetic excitations of the various magnetically ordered phases spatially anisotropic, as a result of which the thermal conductivity, especially if it is magnon dominated, is generally expected to be different "along" the stripe (or zig-zag) compared to the direction "perpendicular" to it.

In this work, we are interested in the heat carried by both magnetic and lattice degrees of freedom. We consider only temperatures lower than the Debye temperature, and retain the energy of the lattice displacements to quadratic order to obtain a phonon spectrum.[9] The generic resulting phonon Hamiltonian (in the absence of coupling to magnons) is given by

$$\hat{\mathcal{H}}^{\text{pho}} = \sum_{\mathbf{q},s} \hbar\omega_{\mathbf{q}s} c^\dagger_{\boldsymbol{q}s} c_{\boldsymbol{q}s}, \tag{2.3}$$

where s labels the type of phonon polarization, $c^\dagger_{\boldsymbol{q}s}$ ($c_{\boldsymbol{q}s}$) the creation (annihilation) operator of a phonon of wavevector $\boldsymbol{q}$ and polarization s, and $\omega_{\boldsymbol{q}s}$ is its eigenfrequency. At temperatures much lower than the Debye temperature, we can use the Debye model for acoustic phonons (that are of interest in this

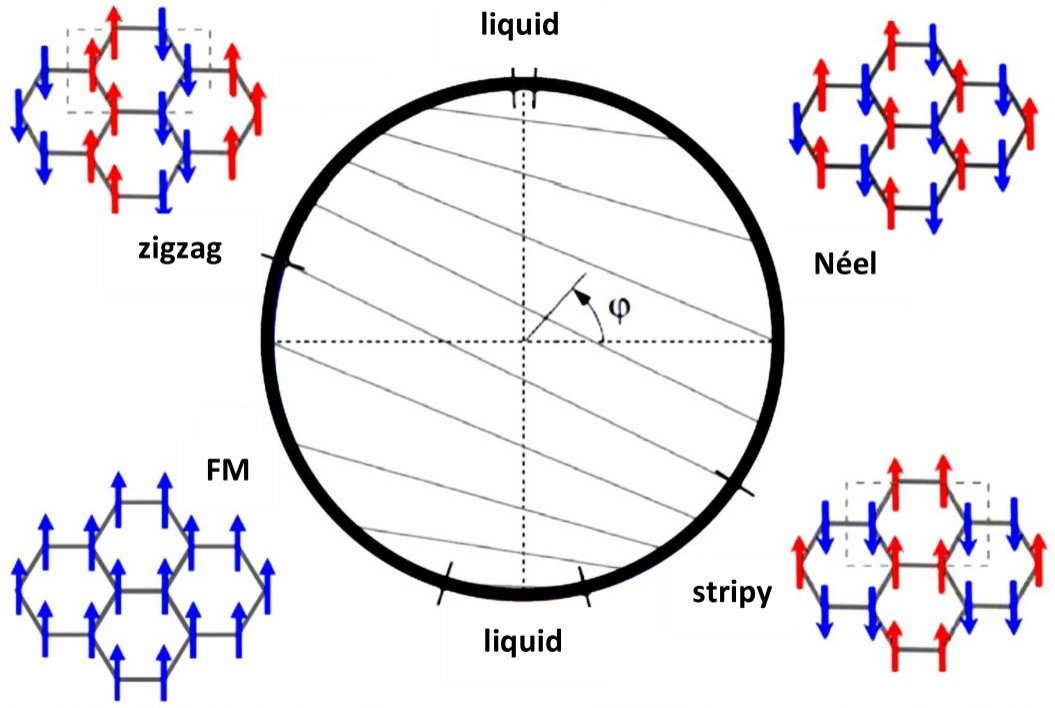

Figure 2.2: Phase diagram of the Kitaev-Heisenberg model with the parametrization of Eq.(2.2). A variety of magnetic and non-magnetic "liquid" phases are present as a function of the angle φ.[17] A schematic of the various ordered states is shown. The magnetic unit cell for the zigzag and the stripy phase is shown as a dashed rectangle.

work), which assumes that $\omega_{\boldsymbol{q}s} = v|\boldsymbol{q}|$, i.e. the phonon dispersion is spatially isotropic. We further assume the phonons are two-dimensional, and therefore they only disperse within the plane of the honeycomb lattice.

The coupling between the phonons and the magnons enters through the distance dependence of the exchange constants, $J_{ij} = J(\boldsymbol{r}_i - \boldsymbol{r}_j)$, $K_{ij} = K(\boldsymbol{r}_i - \boldsymbol{r}_j)$, where $\boldsymbol{r}_i$ and $\boldsymbol{r}_j$ denote the dynamic position of the ions at the i^{th} and j^{th} lattice sites. Assuming a small displacement of the ions from

their equilibrium positions (long phonon wavelength approximation consistent also with the linear isotropic phonon dispersion given above), the exchange constants can be approximated as[27]

$$J_{ij} = J(\boldsymbol{R}_i + \boldsymbol{u}_i - \boldsymbol{R}_j - \boldsymbol{u}_j) = J(\boldsymbol{R}_{ij}) + \boldsymbol{u}_{ij} \cdot \boldsymbol{J}'_{ij} + ..., \tag{2.4}$$

$$K_{ij} = K(\boldsymbol{R}_i + \boldsymbol{u}_i - \boldsymbol{R}_j - \boldsymbol{u}_j) = K(\boldsymbol{R}_{ij}) + \boldsymbol{u}_{ij} \cdot \boldsymbol{K}'_{ij} + ..., \tag{2.5}$$

where

$$\boldsymbol{J}'_{ij} = \nabla_{\boldsymbol{r}_{ij}} J(\boldsymbol{r}_{ij})\big|_{\boldsymbol{r}_{ij}=\boldsymbol{R}_{ij}},\ \boldsymbol{K}'_{ij} = \nabla_{\boldsymbol{r}_{ij}} K(\boldsymbol{r}_{ij})\big|_{\boldsymbol{r}_{ij}=\boldsymbol{R}_{ij}},$$

are gradients with respect to $\boldsymbol{r}_{ij}$ evaluated at the equilibrium magnetic ion distances $\boldsymbol{R}_{ij}$. Here, $\boldsymbol{u}_{ij} \equiv \boldsymbol{u}_i - \boldsymbol{u}_j$, $\boldsymbol{r}_{ij} \equiv \boldsymbol{r}_i - \boldsymbol{r}_j = \boldsymbol{R}_i + \boldsymbol{u}_i - \boldsymbol{R}_j - \boldsymbol{u}_j$, and $\boldsymbol{R}_{ij} \equiv \boldsymbol{R}_i - \boldsymbol{R}_j$.

The ionic displacement from its equilibrium position is expressed in terms of phonon creation and annihilation operators as[70, 92]

$$\boldsymbol{u}_{i\tau} = \sum_{\boldsymbol{q},s} \sqrt{\frac{\hbar}{2NM\omega_{\boldsymbol{q}s}}} \left(c^{\dagger}_{-\boldsymbol{q}s} + c_{\boldsymbol{q}s}\right) e^{i\boldsymbol{q}\cdot\boldsymbol{R}_i} \hat{\boldsymbol{e}}_{\boldsymbol{q}s\tau}, \tag{2.6}$$

where N is the total number of chemical unit cells, M the mass of the magnetic atoms (assumed of the same type on each sublattice), and $\hat{\boldsymbol{e}}_{\boldsymbol{q}s\tau}$ the direction of the displacement of the magnetic ion at the i^{th} lattice position of the τ^{th} sublattice (the honeycomb lattice has two sublattice sites), relative to a phonon of polarization s and direction of propagation given by $\boldsymbol{q}$.

Within the long wavelength approximation valid for the acoustic phonons, ionic displacements from their equilibrium positions are taken sublattice inde-

pendent, and denoted as

$$\boldsymbol{u}_i = \frac{1}{\sqrt{N}} \sum_{\boldsymbol{q}} e^{i\boldsymbol{q}\cdot\boldsymbol{R}_i} \vec{u}_{\boldsymbol{q}}, \tag{2.7}$$

where $\boldsymbol{R}_i$ denotes the lattice equilibrium position of a magnetic ion, and we have defined

$$\vec{u}_{\boldsymbol{q}} = \sum_s \sqrt{\frac{\hbar}{2M\omega_{\boldsymbol{q}s}}} \left(c^\dagger_{-\boldsymbol{q}s} + c_{\boldsymbol{q}s}\right) \hat{\boldsymbol{e}}_{\boldsymbol{q}s}. \tag{2.8}$$

Substituting Eqs.(2.4) and (2.5) into Eq.(2.1), one finds an expansion of the magnetic part of the total Hamiltonian in powers of phonon operators,

$$\hat{\mathcal{H}}^{\text{pho}}_{\text{spin}} = \hat{\mathcal{H}}^{\text{0pho}}_{\text{spin}} + \hat{\mathcal{H}}^{\text{1pho}}_{\text{spin}} + \hat{\mathcal{H}}^{\text{2pho}}_{\text{spin}} + ... \tag{2.9}$$

where the first term of the spin-phonon Hamiltonian has magnetic ions at their lattice equilibrium positions,and thus it is spin only, the second term is the coupling of one power of phonon operators with the spin system, the third term the coupling of two powers of phonon operators with the spin system and so on.

In the low temperature regime and under the assumption of weak magnon-phonon coupling, one-phonon processes are more important than multiple phonon processes, and therefore we truncate the infinite expansion of Eq.(2.9) up to the $\hat{\mathcal{H}}^{\text{1pho}}_{\text{spin}}$ term. More specifically, we retain the following two terms of Eq.(2.9),

$$\hat{\mathcal{H}}^{\text{0pho}}_{\text{spin}} = \sum_{\langle ij\rangle} J(\boldsymbol{R}_{ij})\ \boldsymbol{S}_i \cdot \boldsymbol{S}_j + \sum_{\langle ij\rangle} 2K(\boldsymbol{R}_{ij})\ S^\gamma_i S^\gamma_j, \tag{2.10}$$

$$\hat{\mathcal{H}}^{\text{1pho}}_{\text{spin}} = \sum_{\langle ij\rangle} \left(\boldsymbol{u}_{ij} \cdot \boldsymbol{J}'_{ij}\right) \boldsymbol{S}_i \cdot \boldsymbol{S}_j + 2 \sum_{\langle ij\rangle} \left(\boldsymbol{u}_{ij} \cdot \boldsymbol{K}'_{ij}\right)\ S^\gamma_i S^\gamma_j. \tag{2.11}$$

In our Boltzmann approach to the thermal transport, Eq.(2.11) will be treated perturbatively as a term that scatters magnons and phonons, leading to a finite lifetime (and scattering rate) of each.

2.2 Magnons and Scattering Amplitudes

The phase diagram of Eq.(2.1) and its extension, Eq.(2.2), has been obtained previously in the literature.[16, 17, 90, 41] Here, we are interested in the magnetic excitations above the ground state, which are needed to compute the thermal transport due to the magnetic degrees of freedom.

We compute the magnon spectrum by representing the three Hermitian spin operators $\boldsymbol{S}_i = (S_i^x, S_i^y, S_i^z)$ with Bose operators using the Holstein-Primakoff (HP) representation[10] (see below) which employs a Taylor expansion in powers of $1/S$ in the spin operators around the classical ground state, as a result of which the $\hat{\mathcal{H}}_{\text{spin}}^{0\text{pho}}$ and $\hat{\mathcal{H}}_{\text{spin}}^{1\text{pho}}$ terms are decomposed as

$$\hat{\mathcal{H}}_{\text{spin}}^{0\text{pho}} = \hat{\mathcal{H}}_{0\text{mag}}^{0\text{pho}} + \hat{\mathcal{H}}_{1\text{mag}}^{0\text{pho}} + \hat{\mathcal{H}}_{2\text{mag}}^{0\text{pho}} + ... \tag{2.12}$$

$$\hat{\mathcal{H}}_{\text{spin}}^{1\text{pho}} = \hat{\mathcal{H}}_{0\text{mag}}^{1\text{pho}} + \hat{\mathcal{H}}_{1\text{mag}}^{1\text{pho}} + \hat{\mathcal{H}}_{2\text{mag}}^{1\text{pho}} + ... \tag{2.13}$$

In Eq.(2.12) the first term represents a classical spin background, and the rest of the terms are one magnon, two magnon (and so on) terms. In Eq.(2.13), the first term represents the propagation of one power of phonon operator in a classical spin background, the second term the coexistence of one phonon and one magnon (that for non-collinear phases leads to magnon-phonon hybridization), the third term the coexistence of one phonon and two magnons and so

on.

At temperatures much lower than the magnetic transition temperature (which we assume throughout our analysis), the linear spin wave approximation for the magnon energies can be used. The terms trilinear, quadrilinear and higher order in the magnon operators lead to a renormalization of the magnon bands via magnon-magnon interactions in Eq.(2.12), and are assumed to be negligible in the low-temperature limit. Furthermore, due to the smallness of the magnon and phonon populations in the temperature regime of interest, we similarly discard terms of higher order in the magnon operators in Eq.(2.13). We further note that the $\hat{\mathcal{H}}^{0\text{pho}}_{1\text{mag}}$ and $\hat{\mathcal{H}}^{1\text{pho}}_{1\text{mag}}$ terms are zero for collinear magnetic orders (all the magnetic orders in Fig.2.2 are collinear), which can be seen straightforwardly by using the HP representation in the the linear spin wave approximation. Therefore, the remaining dominant interaction term is $\hat{\mathcal{H}}^{1\text{pho}}_{2\text{mag}}$.

Since the magnetic phase diagram of our spin Hamiltonian includes only collinear states, we define a positive z-direction (choice is arbitrary) for the ordered moments, and in the linear spin wave approximation, local moments that are in the positive direction are expanded as

$$S_i^{||} = S - a_i^\dagger a_i, \tag{2.14}$$

$$S_i^{+} \approx \sqrt{2S} a_i, \tag{2.15}$$

$$S_i^{-} \approx \sqrt{2S} a_i^\dagger, \tag{2.16}$$

while local moments that lie in the opposite direction are expanded as

$$S_i^{||} = -S + b_i^\dagger b_i, \tag{2.17}$$

$$S_i^+ \approx \sqrt{2S} b_i^\dagger, \tag{2.18}$$

$$S_i^- \approx \sqrt{2S} b_i, \tag{2.19}$$

where $a_i^\dagger a_i$ creates a spin deviation of the local moment that lies along the positive z-direction and is located at the i^{th} lattice position, at the a-sublattice, and correspondingly for $b_j^\dagger b_j$, which refers to a local moment aligned along the negative z-direction. We can switch to a $\boldsymbol{k}$-space (momentum space) representation by using the following Fourier transform conventions

$$a_i = \sqrt{\tfrac{4}{N}} \sum_{\boldsymbol{k}} e^{i\vec{k}\cdot\vec{\alpha}_0} a_{\boldsymbol{k}}, a_i^\dagger = \sqrt{\tfrac{4}{N}} \sum_{\boldsymbol{k}} e^{-i\vec{k}\cdot\vec{\alpha}_0} a_{\boldsymbol{k}}^\dagger, \tag{2.20}$$

$$b_j = \sqrt{\tfrac{4}{N}} \sum_{\boldsymbol{k}} e^{i\vec{k}\cdot\vec{\beta}_0} b_{\boldsymbol{k}}, b_j^\dagger = \sqrt{\tfrac{4}{N}} \sum_{\boldsymbol{k}} e^{-i\vec{k}\cdot\vec{\beta}_0} b_{\boldsymbol{k}}^\dagger, \tag{2.21}$$

where $\vec{\alpha}_0$, $\vec{\beta}_0$ are the equilibrium positions of the magnetic ions on the a^{th} and b^{th} sublattice, and we take into account the fact that we have four magnetic sublattices for the stripy and the zig-zag phase, each of $N/4$ magnetic ions, and two magnetic sublattices for the Néel and the ferromagnetic phase, each of $N/2$ magnetic ions (in which case the prefactor in Eqs. (2.20) and (2.21) is $\sqrt{2/N}$), given that the Néel and the ferromagnetic phase have a magnetic unit cell that is the same as the chemical unit cell of the honeycomb lattice whereas the magnetic unit cell of the stripy and the zig-zag phase is twice the size of the chemical unit cell of the honeycomb lattice.

Our total Hamiltonian $\hat{\mathcal{H}} = \hat{\mathcal{H}}_0 + \hat{\mathcal{H}}_{\text{int}}$ decomposes into the non-interacting part $\hat{\mathcal{H}}_0 = \hat{\mathcal{H}}_{0\text{mag}}^{0\text{pho}} + \hat{\mathcal{H}}_{2\text{mag}}^{0\text{pho}} + \hat{\mathcal{H}}^{\text{pho}}$, and the lowest order interacting term

$\hat{\mathcal{H}}_{\rm int} = \hat{\mathcal{H}}^{\rm 1pho}_{\rm 2mag}$, where $\hat{\mathcal{H}}^{\rm pho}$ is given by Eq.(2.3), and $\hat{\mathcal{H}}^{\rm 0pho}_{\rm 0mag} = \mathcal{H}_{classical}$. The non-diagonal two magnon part of $\hat{\mathcal{H}}_0$ is compactly given in a matrix form (that takes into account easier the four magnetic sublattices),

$$\hat{\mathcal{H}}^{\rm 0pho}_{\rm 2mag} = \frac{S}{2}\sum_{\boldsymbol{k}} \Psi^{\dagger}(\boldsymbol{k}) M(\boldsymbol{k}) \Psi(\boldsymbol{k}), \tag{2.22}$$

The sum in Eq.(2.22) extends over all wavevectors $\boldsymbol{k}$ in the first magnetic Brillouin zone, and $\Psi^{\dagger}(\boldsymbol{k}) = \left[\ a^{\dagger}_{\boldsymbol{k}},\ \ b^{\dagger}_{\boldsymbol{k}},\ \ c^{\dagger}_{\boldsymbol{k}},\ \ d^{\dagger}_{\boldsymbol{k}},\ \ a_{-\boldsymbol{k}},\ \ b_{-\boldsymbol{k}},\ \ c_{-\boldsymbol{k}},\ \ d_{-\boldsymbol{k}}\ \right]$, is the defined raw vector, and $\Psi(\boldsymbol{k})$ is the complex conjugate column vector, with $a^{\dagger}_{\boldsymbol{k}}$ ($a_{\boldsymbol{k}}$), creating (annihilating) a plane-wave magnon mode on sublattice a and so on, and $M(\boldsymbol{k})$ is an 8×8 (or 4×4 in the case of the Néel and ferromagnetic phases) matrix containing information about the spin wave modes of each magnetic phase (see Appendix A).

In the same magnon operator representation, the interacting Hamiltonian for the one phonon-two magnon processes is written as

$$\hat{\mathcal{H}}^{\rm 1pho}_{\rm 2mag} = \frac{S}{2\sqrt{N}}\sum_{\boldsymbol{k},\boldsymbol{q}} \Psi^{\dagger}(\boldsymbol{k}) \Lambda(\boldsymbol{k},\boldsymbol{q}) \Psi(\boldsymbol{k}-\boldsymbol{q}), \tag{2.23}$$

for phonons with wavevector $\boldsymbol{q}$ and magnons with wave-vectors $\boldsymbol{k}$, and $\boldsymbol{k}-\boldsymbol{q}$ respectively, where momentum conservation has been taken into account, and $\Lambda(\boldsymbol{k},\boldsymbol{q})$ is an 8×8 (or 4×4 for the Néel and ferromagnetic phases) matrix that contains information about the magnon-phonon interaction (it encompasses the gradient terms appearing in Eqs.(2.4) and (2.5)). To switch from the non-diagonal Hamiltonian $\frac{S}{2}\sum_{\boldsymbol{k}} \Psi^{\dagger}(\boldsymbol{k}) M(\boldsymbol{k}) \Psi(\boldsymbol{k})$ of Eq.(2.22) to a diagonal one that

uses non-interacting magnon modes, we symbolically introduce a Bogoliubov-Valatin transformation,[4]

$$\Psi(\boldsymbol{k}) = U(\boldsymbol{k})\Phi(\boldsymbol{k}), \tag{2.24}$$

where

$$\Phi^{\dagger}(\boldsymbol{k}) = \left[\ \alpha^{\dagger}_{\boldsymbol{k}},\ \ \beta^{\dagger}_{\boldsymbol{k}},\ \ \gamma^{\dagger}_{\boldsymbol{k}},\ \ \delta^{\dagger}_{\boldsymbol{k}},\ \ \alpha_{-\boldsymbol{k}},\ \ \beta_{-\boldsymbol{k}},\ \ \gamma_{-\boldsymbol{k}},\ \ \delta_{-\boldsymbol{k}}\ \right]. \tag{2.25}$$

The 8×8 (or 4×4 in the case of the Néel and ferromagnetic phases) coefficient matrix $U(\boldsymbol{k})$ of Eq.(2.24) satisfies the following properties for all momenta in the first magnetic Brillouin zone,

$$U^{\dagger}(\boldsymbol{k})M(\boldsymbol{k})U(\boldsymbol{k}) =$$

$$Diag\left\{\omega_1(\boldsymbol{k}), ..., \omega_4(\boldsymbol{k}), -\omega_5(\boldsymbol{k}), ..., -\omega_8(\boldsymbol{k})\right\},$$

where $\omega_5 = -\omega_1,\ \omega_6 = -\omega_2,\ \omega_7 = -\omega_3,\ \omega_8 = -\omega_4$, and

$$U^{\dagger}(\boldsymbol{k})\ I_{-}\ U(\boldsymbol{k}) = I_{-},$$

$$I_{-} = \begin{bmatrix} I_{4\times4} & 0_{4\times4} \\ 0_{4\times4} & -I_{4\times4} \end{bmatrix},\ I = \begin{bmatrix} I_{4\times4} & 0_{4\times4} \\ 0_{4\times4} & I_{4\times4} \end{bmatrix}.$$

That is, $U(\boldsymbol{k})$ acts as a unitary transformation that diagonalizes the M-matrix, and it also preserves the bosonic nature of the magnon operators.

Under the symbolic Bogoliubov-Valatin transformation of Eq.(2.24) the $\hat{\mathcal{H}}^{\rm 0pho}_{\rm 2mag}$ term becomes

$$\hat{\mathcal{H}}^{\rm 0pho}_{\rm 2mag} = \frac{S}{2}\sum_{\boldsymbol{k}} \Psi^{\dagger}(\boldsymbol{k})M(\boldsymbol{k})\Psi(\boldsymbol{k}) = \frac{S}{2}\sum_{\boldsymbol{k}} \Phi^{\dagger}(\boldsymbol{k})U^{\dagger}(\boldsymbol{k})M(\boldsymbol{k})U(\boldsymbol{k})\Phi(\boldsymbol{k}) =$$

$$S\sum_{\boldsymbol{k}}\Big(\omega_1(\boldsymbol{k})\alpha^{\dagger}_{\boldsymbol{k}}\alpha_{\boldsymbol{k}} + \omega_2(\boldsymbol{k})\beta^{\dagger}_{\boldsymbol{k}}\beta_{\boldsymbol{k}} + \omega_3(\boldsymbol{k})\gamma^{\dagger}_{\boldsymbol{k}}\gamma_{\boldsymbol{k}} + \omega_4(\boldsymbol{k})\delta^{\dagger}_{\boldsymbol{k}}\delta_{\boldsymbol{k}} + \omega_1(\boldsymbol{k})\alpha^{\dagger}_{-\boldsymbol{k}}\alpha_{-\boldsymbol{k}}$$

$$+ \omega_2(\boldsymbol{k})\beta^{\dagger}_{-\boldsymbol{k}}\beta_{-\boldsymbol{k}} + \omega_3(\boldsymbol{k})\gamma^{\dagger}_{-\boldsymbol{k}}\gamma_{-\boldsymbol{k}} + \omega_4(\boldsymbol{k})\delta^{\dagger}_{-\boldsymbol{k}}\delta_{-\boldsymbol{k}}\Big), \tag{2.26}$$

where $\omega_i(\boldsymbol{k}),\ i = \{1, ..., 8\}$ (or $i = \{1, ..., 4\}$ for the Néel and ferromagnetic phases) are the solutions of the secular equation $|D(\boldsymbol{k}) - \omega(\boldsymbol{k})I| = 0$, in which

$$D(\boldsymbol{k}) = I_{-}M(\boldsymbol{k}) \tag{2.27}$$

is the so called dynamical matrix of Ref.[4].

The multiplication with the I_{-} matrix is necessary in order to preserve the Bose commutation relations for the new magnon operators. We mention just for comparison that in the case of Fermi systems, where anticommutation relations are used, this is not necessary because the latter are satisfied automatically, and the dynamical matrix for fermions is equal to the M-matrix, rendering the diagonalization process easier since M is always a Hermitian matrix (as is the original Hamiltonian), while the dynamical matrix is not guaranteed to be Hermitian in all cases since it differs from the original Hamiltonian.[4] The unitary transformation $U(\boldsymbol{k})$ is constructed by taking the eigenvectors of the dynamical matrix $[\upsilon(\omega_i(\boldsymbol{k}))]_{1\times 8}$ and using them as column vectors as below,[4]

$$U(\boldsymbol{k}) = [\upsilon(\omega_1(\boldsymbol{k})), ..., \upsilon(\omega_4(\boldsymbol{k})), \upsilon(\omega_5(\boldsymbol{k})), ..., \upsilon(\omega_8(\boldsymbol{k}))]_{8\times 8}. \tag{2.28}$$

We next express the interaction Hamiltonian $\hat{\mathcal{H}}_{\text{int}}$ in terms of the new magnon quasiparticle operators (by applying the Bogoliubov-Valatin transformation of Eq.(2.24)) as

$$\hat{\mathcal{H}}^{\text{1pho}}_{\text{2mag}} = \frac{S}{2\sqrt{N}} \sum_{\boldsymbol{k},\boldsymbol{q},s} \sqrt{\frac{\hbar}{2M\omega_{\boldsymbol{q}s}}} \Big(c^{\dagger}_{-\boldsymbol{q}s} \Psi^{\dagger}(\boldsymbol{k}) \Lambda'(\boldsymbol{k},\boldsymbol{q}) \Psi(\boldsymbol{k}-\boldsymbol{q}) + c_{\boldsymbol{q}s} \Psi^{\dagger}(\boldsymbol{k}) \Lambda'(\boldsymbol{k},\boldsymbol{q}) \Psi(\boldsymbol{k}-\boldsymbol{q}) \Big)$$
$$= \frac{S}{2\sqrt{N}} \sum_{\boldsymbol{k},\boldsymbol{q},s} \sqrt{\frac{\hbar}{2M\omega_{\boldsymbol{q}s}}} \Big(c^{\dagger}_{-\boldsymbol{q}s} \Phi^{\dagger}(\boldsymbol{k}) U^{\dagger}(\boldsymbol{k}) \Lambda'(\boldsymbol{k},\boldsymbol{q}) U(\boldsymbol{k}-\boldsymbol{q}) \Phi(\boldsymbol{k}-\boldsymbol{q})$$
$$+ c_{\boldsymbol{q}s} \Phi^{\dagger}(\boldsymbol{k}) U^{\dagger}(\boldsymbol{k}) \Lambda'(\boldsymbol{k},\boldsymbol{q}) U(\boldsymbol{k}-\boldsymbol{q}) \Phi(\boldsymbol{k}-\boldsymbol{q}) \Big), \tag{2.29}$$

where the matrix $\Lambda'(\boldsymbol{k},\boldsymbol{q})$ and the matrix $\Lambda(\boldsymbol{k},\boldsymbol{q})$ of Eq.(2.23) are related as

$$\Lambda(\boldsymbol{k},\boldsymbol{q}) = \sum_{s} \sqrt{\frac{\hbar}{2M\omega_{\boldsymbol{q}s}}} \Big(c^{\dagger}_{-\boldsymbol{q}s} + c_{\boldsymbol{q}s} \Big) \Lambda'(\boldsymbol{k},\boldsymbol{q}). \tag{2.30}$$

The Hamiltonian of Eq.(2.29) describes interactions between non-interacting magnons and non-interacting phonons. For later convenience we define the 8×8 *magnon- phonon scattering matrix* (4×4 for the Néel and ferromagnetic phases),

$$T(\boldsymbol{k},\boldsymbol{q}) = \frac{S}{2} \sqrt{\frac{\hbar}{2NM\omega_{\boldsymbol{q}s}}} U^{\dagger}(\boldsymbol{k}) \Lambda'(\boldsymbol{k},\boldsymbol{q}) U(\boldsymbol{k}-\boldsymbol{q}). \tag{2.31}$$

The magnon-phonon scattering matrix can be partitioned as,

$$T(\boldsymbol{k},\boldsymbol{q}) = \begin{bmatrix} [T_{+-}(\boldsymbol{k},\boldsymbol{q})]_{4\times4} & [T_{++}(\boldsymbol{k},\boldsymbol{q})]_{4\times4} \\ [T_{--}(\boldsymbol{k},\boldsymbol{q})]_{4\times4} & [T_{-+}(\boldsymbol{k},\boldsymbol{q})]_{4\times4} \end{bmatrix}_{8\times8}, \tag{2.32}$$

where the submatrices

$$T_{+-}(\boldsymbol{k},\boldsymbol{q}) = [\text{magnon creation + annihilation}]_{4\times4},$$

$$T_{++}(\boldsymbol{k},\boldsymbol{q}) = [\text{two} - \text{magnon creation}]_{4\times4},$$

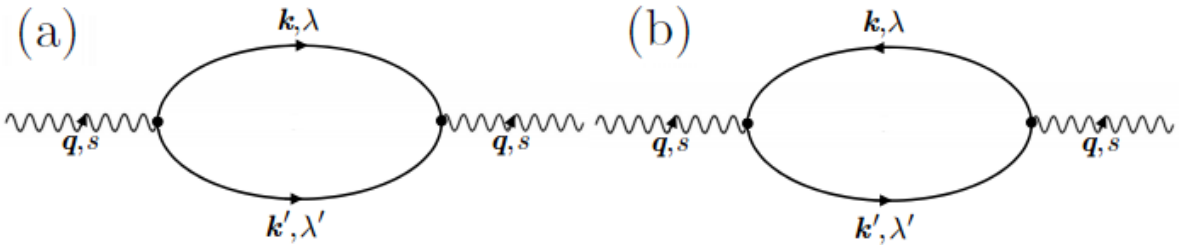

Figure 2.3: Lowest order magnon-phonon scattering diagrams used for the calculation of the transport relaxation times in the regime in which thermal transport is phonon-dominated. Wavy lines represent phonon propagators whereas straight lines are magnon propagators. Fig.(a) represents C-processes which involve two magnon creations or annihilations, where-as Fig.(b) represents R-processes that involve phonon emission or absorption.

$$T_{--}(\boldsymbol{k},\boldsymbol{q}) = [\text{two} - \text{magnon annihilation}]_{4\times4},$$

$$T_{-+}(\boldsymbol{k},\boldsymbol{q}) = [\text{magnon annihilation} + \text{creation}]_{4\times4},$$

are related to the Feynman diagram processes discussed in the next section.

As seen from Eqs.(2.29) and (2.32) one-phonon two-magnon processes can be classified into two main categories: (a) *radiation processes* (denoted as R-processes) and (b) *conversion processes* (denoted as C-processes), where the R-processes are described by the submatrices $T_{+-}(\boldsymbol{k},\boldsymbol{q})$ and $T_{-+}(\boldsymbol{k},\boldsymbol{q})$ in which two magnons of the same or different branch (one created, one annihilated), whereas the C-processes are described by the submatrices $T_{++}(\boldsymbol{k},\boldsymbol{q})$ and $T_{--}(\boldsymbol{k},\boldsymbol{q})$ in which two magnons of the same or different branch, are either created by a phonon or annihilated into a phonon. Processes described by three boson creation or annihilation operators are not taken into account as they do not conserve energy, which is assumed to be exchanged only between the magnons and the phonons. Concluding this section, it should be noted

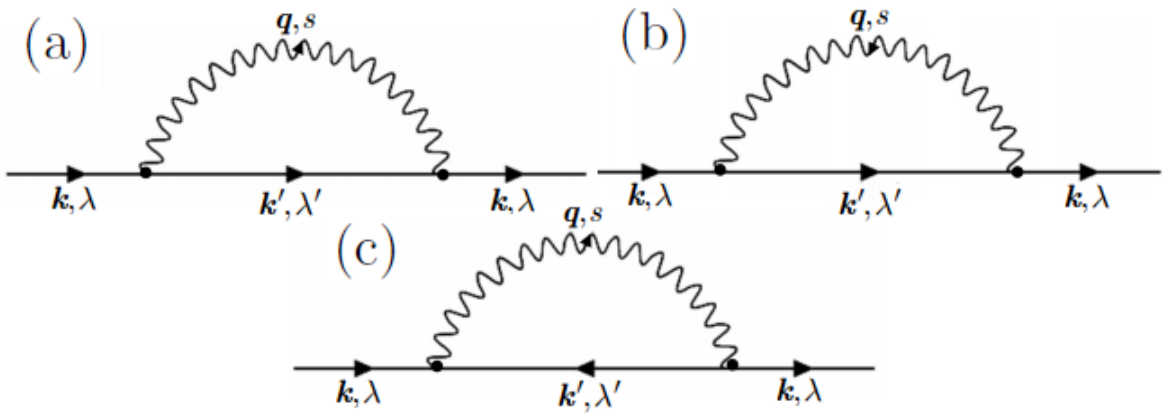

Figure 2.4: Lowest order magnon-phonon scattering diagrams used for the calculation of the transport relaxation times in the regime in which thermal transport is magnon-dominated. Straight lines represent magnon propagators whereas wavy lines are phonon propagators. Figures (a) and (b) represent R-processes which involve phonon emissions or absorptions. Fig.(c) represents C-processes which involve phonon emission or absorption.

that the summations over the phonon and magnon wavevectors in the previous equations extend over the corresponding first Brillouin zones (but in the low temperature regime the main contributions come from the regions around the valleys (minima) of the phonon and the magnon bands), and that only *normal processes* are taken into account (see Ref.[92], section 6.2.4).

2.3 Transport relaxation times

As mentioned previously, in this work we study two distinct thermal transport regimes depending on whether the magnon or the phonon energy scale dominates. In either case, given the matrix elements of the two magnon-one phonon scattering processes, Eq.(2.31), one can proceed to calculate the

respective transport relaxation times using the Fermi's Golden Rule for each (bare) interaction vertex

$$\tau_{I\to F}^{-1} = \frac{2\pi}{\hbar}\sum_{F}\left|\langle F|\,\hat{\mathcal{H}}_{\rm int}\,|I\rangle\right|^2\delta(E_F - E_I), \tag{2.33}$$

where $|I\rangle$ and $|F\rangle$ denote the initial and the final state. In the following, we will repeatedly refer to the diagrams of the Figs. 2.3 and 2.4, denoting a phononic channel as $(\boldsymbol{q}, s)$, and two distinct magnonic channels as $(\boldsymbol{k}, \lambda)$ and $(\boldsymbol{k}', \lambda')$. The final state $|F\rangle$ for a two-magnon annihilation C-process is

$$|F\rangle = |..., n_s(\boldsymbol{q}) + 1, ...\rangle \otimes |..., n_\lambda(\boldsymbol{k}) - 1,..., n_{\lambda'}(\boldsymbol{k}') - 1, ...\rangle\,, \tag{2.34}$$

and for a two-magnon creation C-process is

$$|F\rangle = |..., n_s(\boldsymbol{q}) - 1, ...\rangle \otimes |..., n_\lambda(\boldsymbol{k}) + 1,..., n_{\lambda'}(\boldsymbol{k}') + 1, ...\rangle\,, \tag{2.35}$$

whereas, for a phonon annihilation R-process is

$$|F\rangle = |..., n_s(\boldsymbol{q}) - 1, ...\rangle \otimes |..., n_\lambda(\boldsymbol{k}) - 1,..., n_{\lambda'}(\boldsymbol{k}') + 1, ...\rangle\,, \tag{2.36}$$

and for a phonon creation R-process is

$$|F\rangle = |..., n_s(\boldsymbol{q}) + 1, ...\rangle \otimes |..., n_\lambda(\boldsymbol{k}) - 1,..., n_{\lambda'}(\boldsymbol{k}') + 1, ...\rangle\,, \tag{2.37}$$

where λ and λ' denote the same or different magnon bands/branches, s represents any of the two-dimensional acoustic phonons, and finally, momentum conservation (not momentum equivalence as in the *umklapp processes*) is applied to each interaction vertex.

In the rest of this section, the transport relaxation times for phonons and magnons are calculated, and are afterwards used in the calculation of the diagonal components of the phonon and magnon conductivity tensor respectively. In this study, we focus only on two relaxation mechanisms appearing during the thermal transport: the magnon-phonon scattering mechanism and the always existent boundary scattering (for either the phonons or the magnons). Depending on the relative strength of the characteristic energy scales of the two types of heat carriers, we further distinguish between two limiting thermal transport regimes, the *phonon dominated* and the *magnon dominated*, which in turn consist of three subregimes each, the *diffusive*, the *intermediate*, and the *ballistic* subregime.

2.3.1 Transport relaxation times for magnon-dominated thermal transport

In the case in which the magnon characteristic energy dominates, phonons play the role of a bath, and given the assumed weak magnon-phonon coupling, the problem translates into a problem of a system weakly interacting with a bath. The lowest order non-equivalent Feynmann diagrams to be used for the calculation of the transport relaxation times are those appearing in Fig. 2.4, and focusing on the magnonic channel $(\boldsymbol{k}, \lambda)$, their total contribution is ($s = 1$, since as discussed in the subsection 2.4.2.2 below, only the longitudinal acoustic phonon is of interest)

$$\left.\frac{1}{\tau_\lambda(\boldsymbol{k})}\right|_{mp} = \frac{2\pi}{\hbar}\sum_{\boldsymbol{q},\lambda'}\Big\{\left|T^{\lambda\lambda'}_{-+}(-\boldsymbol{k},-\boldsymbol{q})\right|^2 \times$$
$$\times\,(n_{\boldsymbol{q}}+n_{\boldsymbol{k}-\boldsymbol{q},\lambda'}+1)\delta(\epsilon_{\boldsymbol{k}-\boldsymbol{q},\lambda'}+\hbar\omega_{\boldsymbol{q}}-\epsilon_{\boldsymbol{k},\lambda})+$$
$$\left|T^{\lambda\lambda'}_{-+}(-\boldsymbol{k},\boldsymbol{q})\right|^2(n_{\boldsymbol{q}}-n_{\boldsymbol{k}+\boldsymbol{q},\lambda'})\delta(\epsilon_{\boldsymbol{k}+\boldsymbol{q},\lambda'}-\hbar\omega_{\boldsymbol{q}}-\epsilon_{\boldsymbol{k},\lambda})+$$
$$\left|T^{\lambda\lambda'}_{--}(\boldsymbol{k},-\boldsymbol{q})\right|^2(n_{\boldsymbol{q}-\boldsymbol{k},\lambda'}-n_{\boldsymbol{q}})\delta(\hbar\omega_{\boldsymbol{q}}-\epsilon_{\boldsymbol{q}-\boldsymbol{k},\lambda'}-\epsilon_{\boldsymbol{k},\lambda})\Big\} \qquad (2.38)$$

where the first term on the right hand side (RHS) of Eq.(2.38) corresponds to the Feynmann diagram of the Fig. 2.4(a), the second term to the Feynmann diagram of the Fig. 2.4(b), and the last term to the Feynmann diagram of the Fig. 2.4(c), and for the magnon-phonon scattering matrix elements we used the convention that follows Eq.(2.32). Notice that the above result is directly related to the collision integral of the semiclassical Boltzmann transport theory as applied to the system of the magnons within the relaxation time approximation (see Eq.(B.12)).

The calculation of the RHS of Eq.(2.38) proceeds by turning the summation over the phonon wavevectors into an integral using the well-known formula (A stands for the area)

$$\frac{1}{A}\sum_{\boldsymbol{q}}F(\boldsymbol{q}) = \int\frac{d^2\boldsymbol{q}}{(2\pi)^2}F(\boldsymbol{q}).$$

It should be noticed though, that the highly anisotropic nature of the magnon band structure (as opposed to the phonon band structure) precludes the analytical solution of the energy constraints imposed by the presence of the Dirac δ functions in Eq.(2.38), and one can proceed with the calculation by taking

advantage of the δ function to reduce the dimensionality of the integral by one, by employing the well-known result that $\int_V f(\boldsymbol{r})\delta[g(\boldsymbol{r})]d\boldsymbol{r} = \int_S \frac{f(\boldsymbol{r})}{|\nabla g(\boldsymbol{r})|}d\sigma$, where S is the $(n-1)$-dim surface inside the n-dim volume V, defined by the constraint $g(\boldsymbol{r}) = 0$, under the condition that $\nabla g(\boldsymbol{r}) \neq 0$. This way, the aforementioned two-dimensional integrals turn into one-dimensional integrals over the lines that satisfy the energy constraints imposed by the respective Dirac δ functions. These calculations require a numerical treatment, since neither the Bogoliubov-Valatin transformation nor the energy constraints admit an analytical solution. For more details the reader is referred to the Appendix C.

In Eq.(2.38) it was implicitly assumed that the different scattering events, represented by the non-equivalent Feynmann diagrams of Fig. 2.4, proceed independently. Including further the effect of the boundary scattering of the magnons and assuming that the magnon-phonon scattering processes proceed independently of the boundary scattering, the total probability of scattering for the magnonic channel $(\boldsymbol{k}, \lambda)$ obeys the following Matthiessen's rule:[9]

$$\frac{1}{\tau_\lambda(\boldsymbol{k})} = \frac{1}{\tau_\lambda(\boldsymbol{k})}\bigg|_{mp} + \frac{1}{\tau_\lambda(\boldsymbol{k})}\bigg|_{b}, \tag{2.39}$$

where the boundary scattering transport relaxation time (for the magnons) was defined as $\frac{1}{\tau_\lambda(\boldsymbol{k})}\Big|_b = \frac{|\vec{v}_\lambda(\boldsymbol{k})|}{L}$, where L is the length of the crystal and $\vec{v}_\lambda(\boldsymbol{k})$ the group velocity of the $(\boldsymbol{k}, \lambda)$ magnonic channel. Notice that λ (or λ') is $\{1, .., 4\}$ for the zig-zag and the stripy phase, and $\{1, 2\}$ for the Néel and the ferromagnetic phase.

2.3.2 Transport relaxation times for phonon-dominated thermal transport

In the case in which the phonon characteristic energy dominates, magnons play the role of a bath, and we again have a problem of a system weakly interacting with a bath. The lowest order non-equivalent Feynmann diagrams to be used for the calculation of the respective transport relaxation times are those appearing in Fig. 2.3, and focusing on the phononic channel $\boldsymbol{q}$ (no band index is used here since we focus only on the transverse acoustic phonon, i.e. $s = 1$, and the justification for focusing on the tranverse acoustic phonon only is given in the subsection 2.4.2.1 below), their total contribution is

$$\begin{aligned}\frac{1}{\tau(\boldsymbol{q})}\bigg|_{mp} = \frac{2\pi}{\hbar}\sum_{\boldsymbol{k}}\sum_{\lambda,\lambda'}\Big\{ \Big|T^{\lambda\lambda'}_{++}(\boldsymbol{k},\boldsymbol{q})\Big|^2 \times \\ \times (n_{\boldsymbol{k},\lambda} + n_{\boldsymbol{q}-\boldsymbol{k},\lambda'} + 1)\delta(\epsilon_{\boldsymbol{k},\lambda} + \epsilon_{\boldsymbol{q}-\boldsymbol{k},\lambda'} - \hbar\omega_{\boldsymbol{q}}) + \\ \Big|T^{\lambda\lambda'}_{-+}(-\boldsymbol{k},\boldsymbol{q})\Big|^2 (n_{\boldsymbol{k},\lambda} - n_{\boldsymbol{k}+\boldsymbol{q},\lambda'})\delta(\epsilon_{\boldsymbol{k}+\boldsymbol{q},\lambda'} - \hbar\omega_{\boldsymbol{q}} - \epsilon_{\boldsymbol{k},\lambda})\Big\}\end{aligned} \tag{2.40}$$

where the first term on the RHS of Eq.(2.40) corresponds to the Feynmann diagram of the Fig. 2.3(a), and the second term to the Feynmann diagram of the Fig. 2.3(b). For the magnon-phonon scattering matrix elements we again used the convention that follows Eq.(2.32). Notice that the above result is directly related to the collision integral of the semiclassical Boltzmann transport theory as applied to the system of phonons within the relaxation time approximation (see Eq.(B.12)).

The calculation of the RHS of Eq.(2.40) proceeds as in the previous

section, i.e. by turning the summation over the magnon wavevector into a two dimensional integral. In Eq.(2.40) it was implicitly assumed that the different scattering mechanisms, represented by the non-equivalent Feynmann diagrams of Fig. 2.3, proceed independently. Including the effect of the boundary scattering of phonons, and assuming that the magnon-phonon scattering processes proceed independently of the boundary scattering, the total probability of scattering for the phononic channel $\boldsymbol{q}$ obeys the following Matthiessen's rule:

$$\frac{1}{\tau(\boldsymbol{q})} = \frac{1}{\tau(\boldsymbol{q})}\bigg|_{mp} + \frac{1}{\tau(\boldsymbol{q})}\bigg|_{b}, \tag{2.41}$$

where the boundary scattering transport relaxation time (for the phonons) was defined as $\frac{1}{\tau(\boldsymbol{q})}\Big|_b = \frac{|\vec{v}_s|}{L}$, where $\vec{v_s}$ denotes the phonon group velocity, within the approximation of the Debye model, is the Debye velocity v_D. Notice that λ (or λ') is $\{1, ..., 4\}$ for the zig-zag and the stripy phase, and $\{1, 2\}$ for the Néel and the ferromagnetic phase.

2.3.3 Computational details of the calculation of the transport relaxation times within different transport subregimes

The calculation of the transport relaxation times requires, via the magnon-phonon scattering matrix elements, knowledge of the spatial derivatives of the Heisenberg and the Kitaev exchange couplings, denoted as J' and K' respectively. For simplicity the derivatives of the exchange couplings are taken as direction independent, and further they are approximated as [109] $J' \approx \frac{\Delta J}{\alpha} \approx \frac{J}{\alpha}$ and $K' \approx \frac{\Delta K}{\alpha} \approx \frac{K}{\alpha}$, respectively, where α denotes the interionic distance. Based on those definitions, one can convert the integrals appearing in

the *total transport relaxation times* (magnonic or phononic) into dimensionless integrals as below

$$\frac{1}{\tau_{mp}} \simeq \frac{SA}{E_D}\frac{1}{N_u\alpha^2} \times 2 \times 10^{12}(secs^{-1}) \times I, \tag{2.42}$$

where, for a specific material, different magnon-phonon scattering processes are encapsulated in the parameter I. S denotes the spin of the local moments, A is the energy scale parameter defined in Eq.(2.2), and further, SA defines an appropriate magnonic energy scale dictated by the interaction term of Eq.(2.23), $E_D \equiv \hbar \upsilon_D q_D = \hbar \upsilon_D 2\pi/\alpha\sqrt{3}$ is the Debye energy scale, N_u the number of nucleons of the ions that form the honeycomb lattice, α the interionic distance in Angstroms, and finally I is the dimensionless form of the *total transport relaxation time* (magnonic or phononic).

The relative strength of the magnon-phonon and the boundary scattering for the case of the magnon-dominated thermal transport, can also be written in terms of the dimensionless parameter I mentioned above, as

$$\left.\frac{\tau_b}{\tau_{mp}}\right|_{mag} \simeq c_{mag} \times \frac{1}{\upsilon_{mag}} \times I, \tag{2.43}$$

where $c_{mag} \equiv 55 \times \frac{1}{\Theta_D(K)} \times \frac{L}{\alpha} \times \frac{1}{N_u\alpha^2}$, L is the length of the crystal in the direction of the applied temperature gradient, and Θ_D the Debye temperature in Kelvin. In addition, $\vec{v}_{mag}(\boldsymbol{k})$ is the dimensionless magnon group velocity which is extracted from the dimensional magnon group velocity $\vec{V}_{mag}(\boldsymbol{k})$ as

below (i.e. their magnitudes are related as)

$$
\begin{aligned}
|\vec{V}_{mag}(\boldsymbol{K})| &= |\nabla_{\boldsymbol{K}}\Omega(\boldsymbol{K})| \\
&= \frac{1}{\hbar}\sqrt{\left(\frac{\partial(\hbar\Omega(\boldsymbol{K}))}{\partial K_x}\right)^2 + \left(\frac{\partial(\hbar\Omega(\boldsymbol{K}))}{\partial K_y}\right)^2} \\
&= \frac{SA\alpha\sqrt{3}}{2\pi\hbar}\sqrt{\left(\frac{\partial(\hbar\omega(\boldsymbol{k}))}{\partial k_x}\right)^2 + \left(\frac{\partial(\hbar\omega(\boldsymbol{k}))}{\partial k_y}\right)^2} \\
&\equiv \frac{SA\alpha\sqrt{3}}{2\pi\hbar}|\vec{v}_{mag}(\boldsymbol{k})|,
\end{aligned} \tag{2.44}
$$

where $\hbar\Omega(\boldsymbol{K})$ denotes the dimensional magnon energy and $\hbar\omega(\boldsymbol{k})$ the dimensionless magnon energy, the two related as $\hbar\Omega(\boldsymbol{K}) = SA \times \hbar\omega(\boldsymbol{k})$. $\boldsymbol{K}$ denotes the dimensional magnon wavevector and $\boldsymbol{k}$ the dimensionless one, the two related as $\boldsymbol{K} = \frac{2\pi}{\alpha\sqrt{3}}\boldsymbol{k}$ (α is the interionic distance on the honeycomb lattice).

On the other hand, the relative strength of the magnon-phonon and the boundary scattering for the case of the phonon-dominated thermal transport can be written in terms of the dimensionless parameter I mentioned above as

$$
\left.\frac{\tau_b}{\tau_{mp}}\right|_{pho} \simeq \frac{SA}{E_D} \times c_{mag} \times I, \tag{2.45}
$$

where the various the parameters were defined previously. By varying the parameter c_{mag} above, either by using different systems or by changing the dimensions of a particular system (the length of the crystal), one can tune the relative strength of the magnon-phonon and boundary scattering, and enter the *ballistic* (boundary scattering dominated), the *diffusive* (magnon-phonon scattering dominated) or the *intermediate* (competing magnon-phonon and boundary scattering) heat transport subregime.

2.4 Calculation of the diagonal components of the thermal conductivity tensor

In the previous sections we introduced the low energy magnetic degrees of freedom via the Hamiltonian of Eq.(2.1), the low energy ionic degrees of freedom via the Hamiltonian of Eq.(2.3), and the magnon-phonon coupling via the Eqs. (2.4) and (2.5). In the next step, the magnon spectra of the various ordered phases were computed within the linear spin wave approximation leading to Eq.(2.22), and those spectra were then used as inputs for the lowest order magnon-phonon scattering processes encompassed in the Hamiltonian of Eq.(2.29). The last information was then used to determine via the Fermi's Golden rule the momentum-dependent total transport relaxation times given by Eqs.(2.39) and (2.41), and in the final step all those results are patched together to compute the diagonal components of the thermal conductivity tensor for each one of the ordered magnetic states, by using the semiclassical Boltzmann transport theory.

As shown in the Appendix B [see Eq.(B.17)], the *thermal conductivity tensor per unit area*, for heat transport dominated by one type of carriers, is given by

$$\kappa_{\alpha\beta} = \sum_{\Lambda} \int \frac{d^2\boldsymbol{K}}{(2\pi)^2} \hbar\Omega_{\Lambda}(\boldsymbol{K}) v^{\alpha}_{\Lambda}(\boldsymbol{K}) v^{\beta}_{\Lambda}(\boldsymbol{K}) \tau_{\Lambda}(\boldsymbol{K}) \frac{\partial n^0_{\Lambda}(\boldsymbol{K})}{\partial T}, \tag{2.46}$$

where Λ denotes the band index, $\boldsymbol{K}$ the wavevector of the quasiparticle, and from which we see that the thermal conductivity is proportional to the energy $\hbar\Omega_{\Lambda}(\boldsymbol{K})$ that the quasiparticles carry, proportional to their velocity $v^{\alpha}_{\Lambda}(\boldsymbol{K})$

in the α-th direction of propagation, proportional to the mean free path $v_\Lambda^\beta(\boldsymbol{K})\tau_\Lambda(\boldsymbol{K})$ that they travel before they scatter, while travelling a total time between two succesive collisions $\tau_\Lambda(\boldsymbol{K})$, and proportional to the total number of quasiparticles that deviate from equilibrium $\frac{\partial n_\Lambda^0(\boldsymbol{K})}{\partial T}$ due to a temperature gradient ∂T, where $n_\Lambda^0(\boldsymbol{K})$ denotes the equilibrium Bose-Einstein distribution function of a quasiparticle in the band Λ. We also note, that since spin-orbit coupling creates anisotropy in the magnon bands, and since the magnon dispersions are involved in the thermal conductivity expression, then it is a useful quantity in this case to study the anisotropy of the thermal conductivity tensor, which will reveal information about the various magnetically ordered phases. Therefore the diagonal components of the thermal conductivity tensor per unit area κ_{xx} and κ_{yy} (with the spatial directions x and y defined as in Fig.A.1, Appendix A) are studied.

In the following sections, we study first the pure boundary scattering on the heat transport by taking both the magnon and the phonon heat carriers into account. Then we slowly change the ratio of boundary scattering to magnon-phonon scattering mechanisms and study the transition from the purely balistic regime(boundary scattering only) to diffusive regive(mostly magnon-phonon scattering). For simplicity we consider only one type of heat carriers in the thermal conductivity, considering the heat that carried from the other carrier as negligible. That means, that we study the limiting cases, first that the energy of the phonons is much greater than the energy of the magnons, and the main heat is carried by the phonons only(where the heat

carried from magnons is considered negligible), and magnons in this case are treated as scatterers only, and second, the opposite case, that the magnons have much higher energy that the phonons, and the heat is carried solely from them, and phonons act as their scatters.

2.4.1 Boundary scattering only regime

In this section, we study the thermal conductivity κ_{xx}, κ_{yy} in in x, y directions respectively, of all the ordered phases of the Heisenberg-Kitaev model, versus temperature. We focus on three characteristic energy ratios between phonon and magnon characteristic energy scales, phonon over magnon energy scale, (i) twice, (ii) equal, and (iii) half. To make the treatment easier and the results more physically meaningful, we convert the thermal conductivity quantities that we plot to dimensionless, by pulling up front all characteristic constants. Thus we have for the magnon thermal conductivity,

$$\kappa_{mag}^{ball} = \frac{1}{2\pi}\frac{L}{a}\frac{k_B S A}{\hbar} \times \tilde{\kappa}_{mag}^{ball}, \tag{2.47}$$

where S is the spin quantum number, k_B is Boltzmann constant, $\tilde{\kappa}_{mag}^{ball}$ is the dimensionless ballistic magnon thermal conductivity per unit area and $a = \alpha\sqrt{3}$, where α denotes the interionic distance, A the magnetic energy scale defined in Eq.(2.2), and temperature is measured in the relevant units of the problem, $[T] = \frac{SA}{k_B}$.

Converting the ballistic phonon thermal conductivity in dimensionless

as well, measuring it in the same units as the magnon one we have,

$$\kappa_{pho}^{ball} = \left(\frac{E_D}{SA}\right)^3 \frac{1}{2\pi}\frac{L}{a}\frac{k_B SA}{\hbar} \times \tilde{\kappa}_{pho}^{ball}, \tag{2.48}$$

where $\tilde{\kappa}_{pho}^{ball}$ is the dimensionless part of the ballistic phonon thermal conductivity.

The *total ballistic thermal conductivity* is

$$\kappa_{tot}^{ball} = \kappa_{mag}^{ball} + \kappa_{pho}^{ball}. \tag{2.49}$$

Eqs.(2.47), (2.48) and (2.49) are applied to each of the diagonal components of the conductivity tensor independently, and the results are shown in Figs. 2.5 and 2.6 below.

In order to have well defined quasiparticles and neglect higher order processes of phonon-phonon, magnon-phonon, and magnon-phonon scattering, we consider temperatures well below the Debye temperature for phonons, and the magnetic critical temperature for magnons, in Figs. 2.5 and 2.6.

Since the heat carriers, phonons, and magnons, are scattered only from the boundaries of the crystal, where a square crystal is assumed for simplicity, the mean free path of the quasiparticles is equal to the length of the crystal L. In this case, differences on thermal conductivity reflect differences of the magnon bands, since all the remaining quantities in the expression of the thermal conductivity (2.46) depends on the magnon dispersions, i.e. the magnon

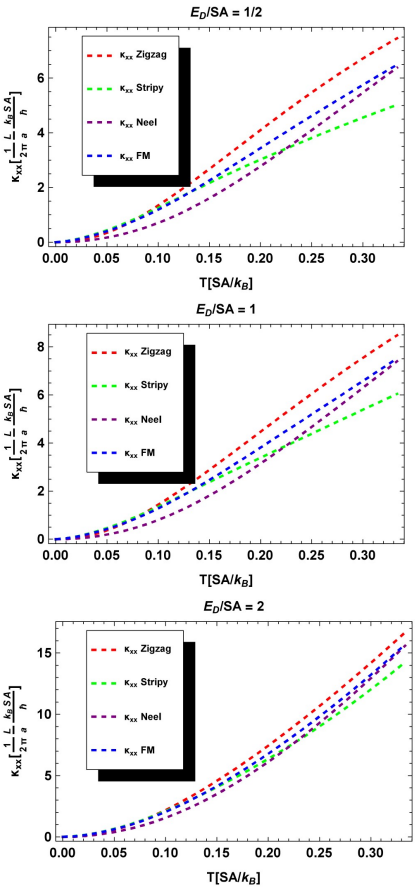

Figure 2.5: κ_{xx} component of the total fully ballistic thermal conductivity per unit area, for each ordered phase (see the legend of each subfigure), for different relative strengths of the Debye energy E_D to the magnon characteristic energy SA (given on top of each subfigure), versus temperature. The temperature region is well below the lowest of the two characteristic energy scales (phononic or magnonic). Notice that the conductivity components are measured in the units given by the prefactor on the RHS of Eq.(2.47). The spatial direction x is defined as in Fig.A.1, Appendix A.

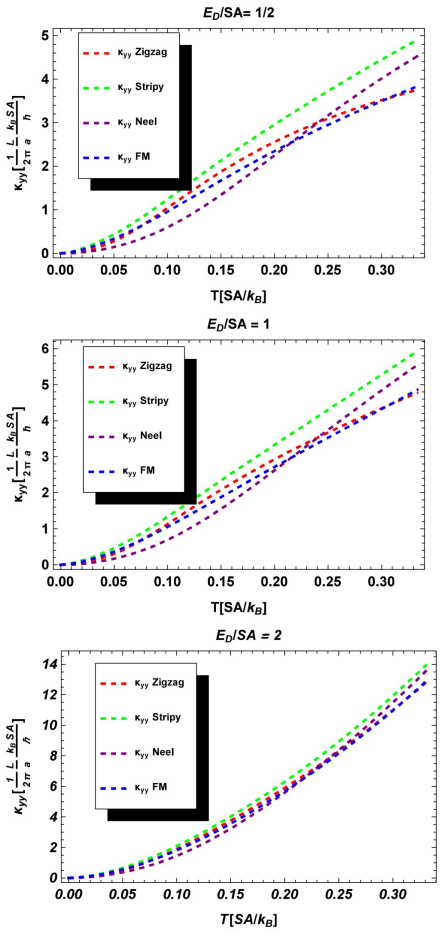

Figure 2.6: κ_{yy} component of the total ballistic thermal conductivity per unit area, for each ordered phase (see the legend of each subfigure), for different relative strengths of the Debye energy E_D to the magnon characteristic energy SA (given on top of each subfigure), versus temperature. The temperature region is well below the lowest of the two characteristic energy scales (phononic or magnonic). Notice that the conductivity components are measured in the units given by the prefactor on the RHS of Eq.(2.47). The spatial direction y is defined as in Fig.A.1, Appendix A.

energies, velocities, and Bose occupation factors, where the phonon band structure is common for all the magnetically collinear phases of our model.

For the phonons we treat the one longitudinal and one transverse phonons in two dimensions, with the Debye model, for which in 2D the low temperature thermal conductivity is proportional to T^2, instead of T^3 in 3D.

In Figs. 2.5 and 2.6, we see the κ_{xx}, and κ_{yy} conductivities for all the collinear phases of Heisenberg-Kitaev model, for three characteristic energy ratios between magnon and phonon energy scales: (i) $E_D/SA = 1/2$, (ii) $E_D/SA = 1$, (iii) $E_D/SA = 2$. In case (i) since the magnon energy is greater than the phonon one, the magnonic conductivity dominates, and since the magnon spectra for all the phases are different in x and y directions, this is reflected in the conductivities as well, which are also different in different directions.

Looking specifically the behavior for each phase, the Neel phase, has few low energy excitations and thus it has the lowest conductivity of all phases, in the temperature window $T = (0.05 - 0.20)SA/k_B$. By looking more carefully the spinwave spectrum of this phase in Fig. A.6, we see one very anisotropic band, that become more important at higher temperatures. Thus at higher temperatures we see very different group velocities and consequently conductivities as well, in x and y direction, with approximately $\kappa_{xx} \approx \frac{3}{2}\kappa_{yy}$. However due to this very steep magnon band that continues even at higher energy, there is no saturation sign of the thermal conductivity.

In contrast, the stripy phase as seen from its low energy spinwave Fig. A.4, has a quadratic and isotropic dispersion $\omega(\boldsymbol{k}) \propto k^2$ at $\omega(\boldsymbol{k}) \to 0$, and the occupation of low energy magnons is much greater (through the Bose occupation factors), thus at low temperatures has the greater conductivity of all the phases. Also it has softer bands (lower in energy) than the other phases, and they can be easier occupied with increasing temperature. The isotropic dispersion, gives isotropic group velocities, which in turn give isotropic conductivities, $\kappa_{xx} \approx \kappa_{yy}$. Since all other phases are anisotropic, with anisotropic conductivities in x and y directions, stripy phase can be easily distinguished from them due to its isotropic character.

Turning our attention into the zig-zag phase, we see that it has the greater conductivity in x direction, and specifically in higher temperature, from all the other phases. Although it has linear dispersion $\omega(\boldsymbol{k}) \propto k$ at $\omega(\boldsymbol{k}) \to 0$, it has enough low energy bands to have excited heat carriers at low temperatures as seen in Fig. A.2, which they show a nearly isotropic dispersion, but mainly in higher temperatures the higher energy excitations in Fig. A.3 show a very anisotropic velocities in x and y directions, giving the highest conductivity in the x direction of all the phases, and the lowest of all in the y direction, and signs of saturation in this direction as well. As the most anisotropic phase of all, at higher temperatures it gives nearly twice the conductivity in x than in y direction $\kappa_{xx} \approx 2\kappa_{yy}$.

The ferromagnetic phase as seen from Fig. A.7 has quadratic dispersions $\omega(\boldsymbol{k}) \propto k^2$ at $\omega(\boldsymbol{k}) \to 0$, with much smaller group velocities in y-direction

that in x-direction, which gives a similar an anisotropic conductivity behavior $\kappa_{yy} \approx \frac{2}{3}\kappa_{xx}$.

In case (ii) where the magnon and phonon energy scales are equal, $E_D/SA = 1$, they both carry heat equally well, and the result shown in the middle figure of Figs. 2.5 and 2.6 is a combination of phonon conduction and magnon conduction, retaining in part the anisotropic features of the magnon conductivities but smoothen out partially due to the isotropic phonon conductivity.

In case (iii), bottom figure of Figs. 2.5 and 2.6, where the phonon energy scale dominates over the magnonic one, $E_D/SA = 2$, the thermal conductivity shows features which are mainly phononic. That means, that it becomes isotropic in x and y directions, and it is quadratic, reminiscent the Debye model in 2D.

Having discussed in this section the boundary scattering regime, and having it as a reference point for further studies, we can now slowly change the ratio of boundary scattering to magnon-phonon scattering mechanisms and study in the next section their effect in heat conduction

2.4.2 Magnon-phonon dominated regime

2.4.2.1 Phonon dominated thermal transport

In this section we consider the limit that the phonon energy scale is much larger than the magnon one, and the heat can be approximated that is carried from phonons only, and the magnons are treated only as scatterers to

the phonons. A ratio of phonon energy scale(E_D) to magnon energy scale(SA), $E_D/SA = 7$ suffice for the heat to be described as carried predominately from phonons.

Since all the factors in the thermal conductivity expression Eq. (2.46) are the same except the relaxation times for boundary scattering, and for magnon-phonon scattering, any difference from the boundary scattering thermal conductivity is attributed to magnon-phonon scattering.

At low enough temperatures, the displacement of the ions from their equilibrium positions are small compared to the interionic distance α ($u/\alpha \ll 1$), and consequently the magnon-phonon couplings $g^J_{mp} \propto \vec{u}_{\boldsymbol{q}} \cdot \boldsymbol{J'}(\boldsymbol{R}_{ij})$ and $g^K_{mp} \propto \vec{u}_{\boldsymbol{q}} \cdot \boldsymbol{K'}(\boldsymbol{R}_{ij})$ (reminding to ourselves that $J' \approx J/\alpha$, and $K' \approx K/\alpha$) are always much smaller than the exchange couplings $\boldsymbol{J}(\boldsymbol{R}_{ij})$ and $\boldsymbol{K}(\boldsymbol{R}_{ij})$, respectively, thus the magnon-phonon interaction term in the Hamiltonian is much smaller that the spin part only(Heisenberg and Kitaev terms), and the interaction can be treated perturbatively in lowest order safely.

As mentioned above, the magnon-phonon coupling g_{mp} depends on the displacement of the ions from their equilibrium positions, and since longitudinal acoustic phonons create greater displacement than the transverse ones, which mostly change the angle between the ions, and less their distance, they should be coupled stronger to the magnons than the transverse ones. This effect can be taken into account by denoting to the transverse acoustic phonons a *reduced coupling constant* $\tilde{g}_{mp}(\boldsymbol{k}, \boldsymbol{q}) = g_{mp}(\boldsymbol{k}, \boldsymbol{q})/\gamma$, where $g_{mp}(\boldsymbol{k}, \boldsymbol{q})$ is the magnon-phonon coupling constant used for the longitudinal acoustic phonons,

and γ is a reduction factor such that $\gamma \sim 10$. That means that as far as phonon conduction concerns, we need to consider only the transverse acoustic phonon, since the longitudinal one will be scattered more strongly and it will not conduct.

In transitioning from the boundary scattering regime to the magnon-phonon dominating regime, we consider the ratio of the two scattering mechanisms which for phonon conduction is,

$$\left.\frac{\tau_b}{\tau_{mp}}\right|_{pho} \simeq \frac{SA}{E_D} \times c_{mag} \times \frac{1}{\gamma^2} \times I, \tag{2.50}$$

where for convenience we set

$$c_{pho} \equiv \frac{SA}{E_D} \times c_{mag} \times \frac{1}{\gamma^2}. \tag{2.51}$$

and I is the dimensionless integral of the scattering rate.

To study the transition from the boundary scattering/ballistic regime, to intermediate, and finally to magno-phonon dominated/diffusive regime, we can increase slowly the length of the crystal L, and unmask the magnon-phonon scattering mechanisms. Numerically we can do that but changing the relative ratio of the two scattering mechanisms, by treating c_{pho} as a tunable parameter, and express it as $c_{pho} = 10^l$, $l \in \mathbb{Z}$.

In order to neglect higher order processes (phonon-phonon, magnon-magnon, and higher order of magnon-phonon) and keep as the dominant one, only the lowest order one phonon-two magnon processes, we go up to temperatures of one third of the energy scale of the lowest energy quasiparticles,

here magnons, thus we take as a maximum temperature $T_{max} = \frac{1}{3}\frac{SA}{k_B}$. These units of temperature guide us, as the natural units to measure the thermal conductivity to be $\frac{1}{2\pi}\frac{L}{a}\frac{k_B SA}{\hbar}$.

Turning our attention now to Fig. 2.7, we see in the black dashed curve the boundary scattering only mechanism, which goes as T^2, as a reference, and then by gradually increasing the strength of the magnon-phonon scattering mechanism, compared to the boundary one, we go first in the mostly ballistic regime, which is mainly boundary scattering but not only, then to the intermediate regime, and finally to the magnon-phonon dominated regime completely. In Fig.2.8 we divide by T^2, to see more clearly the deviation from the boundary scattering mechanism.

One key feature seen in Figs. 2.7, 2.8, is that the conductivities κ_{xx}, and κ_{yy} are isotropic even in the deeply diffusive regime. Exact matching cannot be possible because of the anisotropic character of the magnon bands. This can tell us, that no-matter how anisotropic the magnon bands are, phonon thermal conductivity retains its isotropic character. Second, we can see that even at low temperatures, high energy phonons can be scattered efficiently from low energy magnons, leading to a deviation of the thermal conductivity from the boundary scattering term T^2 even at very low temperatures. The only phase that magnon-phonon scattering starts at higher temperature is the stripy phase, and this is because at low temperatures, the high energy phonons with small wavevector, cannot conserve energy and momentum to scatter to two magnons since the minimum of the magnon bands are far away from the

the center of the first Brillouin zone, the magnon bands are isotropic, and have quadratic dispersion, while the phonons have linear dispersion, and thus one phonon-two magnon processes do not satisfy both energy and momentum conservation. Thus in stripy phase, magnon-phonon scattering starts at higher temperatures where there are more options for scattering.

Last thing to say in this section, is that since the temperatures we study are $T_{max} \ll J$, and there exist high energy excitations compared to T_{max}, up to the temperatures that we go, there is no saturation of the thermal conductivity as well as of the magnon-phonon scattering mechanism.

2.4.2.2 Magnon dominated thermal transport

As in the previous section, we use as a reference the boundary scattering for magnon conduction. Any deviation from that is attributed to magnon-phonon scattering mechanism.

In order thermal conduction to be magnon dominated by order of magnitude different than the phonon one, and as a result to focus only on one type of heat carriers again, in this case magnons only carry heat, and phonons are treated as scatterers only, the energy scale difference between magnons and phonons was taken as $SA/E_D = 7$.

Furthermore, the argument that was given in the previous section, that the magnon-phonon coupling is stronger for the longitudinal acoustic phonons and weaker for the transverse can be used here as well. However in this section we are interested in phonons as scatterers, thus we can take only the

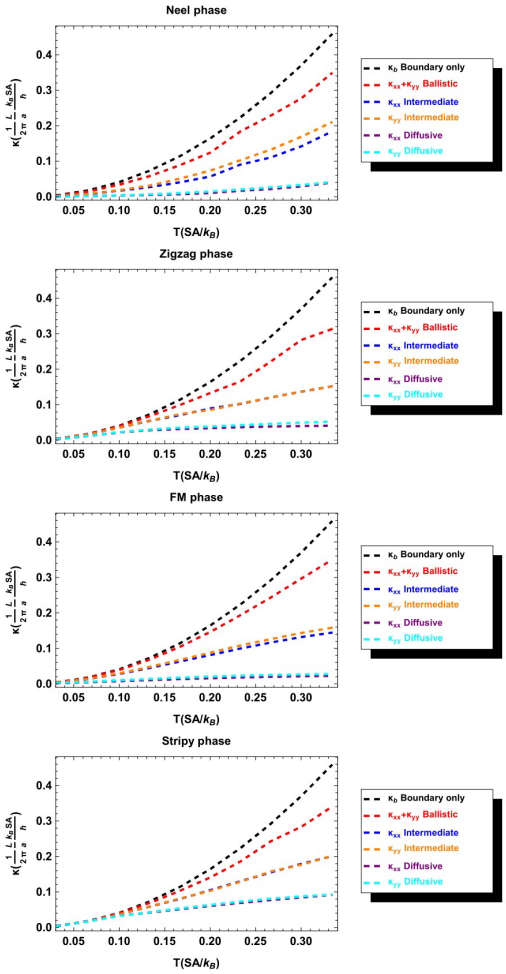

Figure 2.7: Phonon dominated transport: κ_{xx} and κ_{yy} component of the phononic thermal conductivity per unit area, for each ordered phase, for three different subregimes: ballistic, intermediate and diffusive (see the legend of each subfigure) as well as pure boundary scattering, versus temperature. The spatial directions x and y are defined as in Fig.A.1, Appendix A.

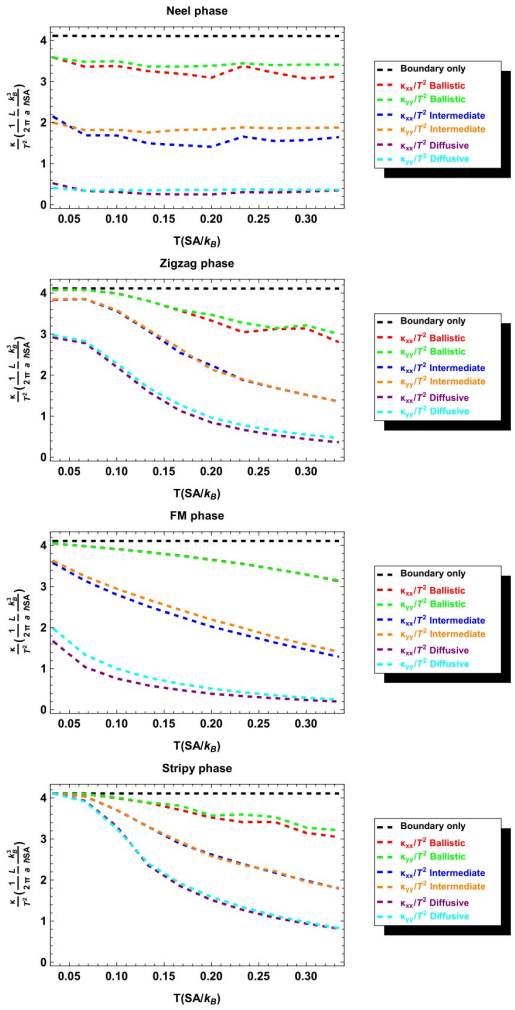

Figure 2.8: Phonon dominated transport: κ_{xx}/T^2 and κ_{yy}/T^2 component of the phononic thermal conductivity per unit area, for each ordered phase, for three different subregimes: ballistic, intermediate and diffusive (see the legend of each subfigure) as well as pure boundary scattering, versus temperature. The spatial directions x and y are defined as in Fig.A.1, Appendix A.

stronger scatterers of the two, and neglect the other one. That means we neglect scattering from the transverse acoustic phonons and we consider only scattering of the magnons by the longitudinal acoustic phonons only.

Also, we mention that in order to neglect higher order processes again, i.e. phonon-phonon, magnon-magnon, higher order magnon-phonon, we go up to temperatures of 1/3rd of the lowest energy scale, which here is the phonon one. Thus we consider temperatures up to $\frac{1}{3}E_D/k_B$ as seen from Figs. 2.9, 2.10.

To study the transition from the boundary scattering only magnonic thermal conductivity, to the magnon-phonon scattering regime, we increase again slowly the length of the crystal and the magnon-phonon scattering is unmasked, or equivalently we increase the ratio of the magnon-phonon to boundary scattering strength, as given from Eq.(2.43), by treating $c_{mag} = 10^l$ as a parameter, and slowly change its value to enter gradually from the one regime to the other.

Turning our attention now to Figs. 2.9, 2.10, we see plots of the magnonic thermal conductivity for boundary scattering only, ballistic regime (which is mainly boundary scattering but not only), intermediate regime, and finally diffusive regime in which scattering is mainly magnon-phonon driven. In Fig. 2.10, the conductivities are divided by a temperature power law that can approximate in most cases the boundary scattering term, and make more obvious the effect of the magnon-phonon interaction compared to that. Thus the boundary scattering magnonic thermal conductivity it was found to be

proportional to T^n, where for the stripy phase $n = 1.506$ in both κ_{xx} and κ_{yy} directions, in ferromagnetic phase the corresponding powers were $n_{xx} = 1.515$ in κ_{xx} direction, and $n_{yy} = 1.509$ in κ_{yy} direction as well. Continuing in the zig-zag phase $n = 2.004$ in both directions, and in the Neel phase,the power law seems to change with temperature, and only for very low temperatures the exponents where found to be $n_{xx} = 2.42$ and $n_{yy} = 2.33$ in κ_{xx} direction, and κ_{yy} directions respectively.

As we are going from the ballistic to the diffusive regime and as the temperature is increased, the initial anisotropy of the magnonic thermal conductivity tensor at the boundary scattering regime, fades out, and at the diffusive regime and at higher temperatures becomes isotropic.

In conclusion, we can say that the greater differences in magnonic thermal conductivities between different phases appear at the boundary scattering regime, where their differences between their corresponding magnon bands are reflected more clearly. Going in the magnon-phonon dominated regime, they seem to approximately follow some temperature power laws, but after they start losing their distinct features.

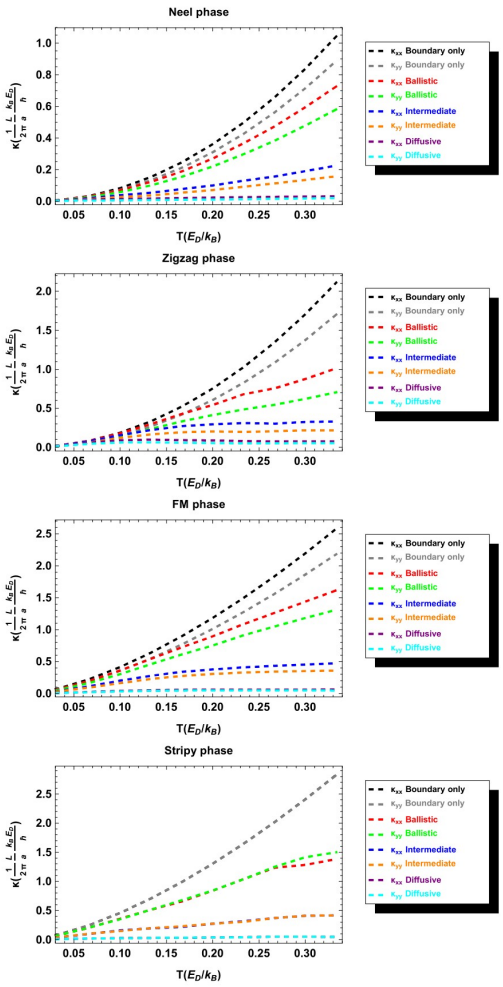

Figure 2.9: Magnon dominated transport: κ_{xx} and κ_{yy} component of the magnonic thermal conductivity per unit area, for each ordered phase, for three different subregimes: ballistic, intermediate and diffusive (see the legend of each subfigure) as well as pure boundary scattering, versus temperature. The spatial directions x and y are defined as in Fig.A.1, Appendix A.

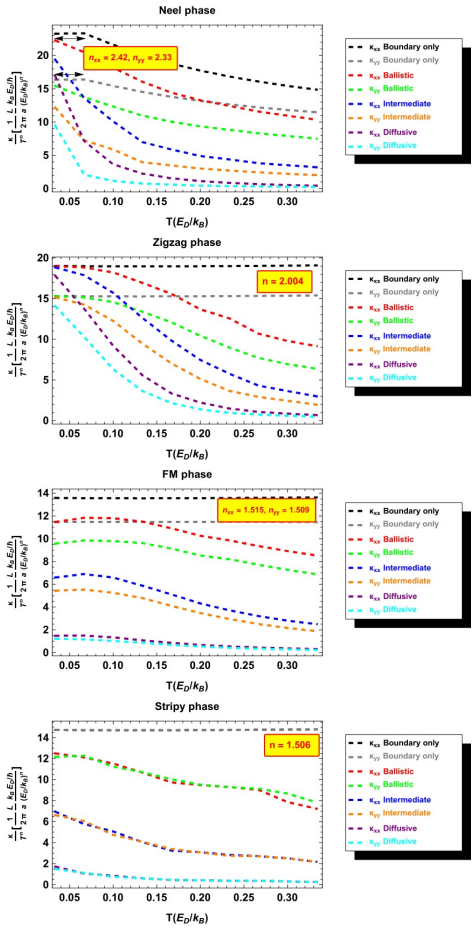

Figure 2.10: Magnon dominated transport: κ_{xx}/T^n and κ_{yy}/T^n component of the magnonic thermal conductivity per unit area, for each ordered phase, for three different subregimes: ballistic, intermediate and diffusive (see the legend of each subfigure) as well as pure boundary scattering, versus temperature. The appropriate temperature exponent n that should divide κ_{xx} and κ_{yy} such that the pure boundary scattering results are represented by horizontal straight lines (at least at low temperatures) is given in the nearby yellow inset. The exponents can slightly vary for the spatial directions x and y, as defined in Fig.A.1, Appendix A.

Chapter 3

Mixing of t_{2g}-e_g orbitals in 4d and 5d transition metal oxides

This chapter is organized as follows. In Sec. 3.1 we summarize the effects of a local cubic crystal field on the d-orbital level structure of a transition metal ion. In Sec. 3.2 we provide the details of the Hamiltonian with and without t_{2g}-e_g mixing in the presence of spin-orbit coupling. In Sec. 3.3 and Sec. 3.4 we describe the interaction terms and conserved quantities of the full system we study, and in Sec. 3.5 we present the results of our exact diagonalization studies for all electron fillings. Again, as in chapter 2, the main conclusions are left to be summarized all together in chapter 4.

3.1 Octahedral crystal fields

A transition metal ion in free space has rotational symmetry SO(3) and therefore five-fold degenerate d-orbitals. Frequently, transition metal ions in crystals are held inside regular octahedral cages, surrounded by ligands. A common type of these ligands is oxygen, which form the large class of transition metal oxides. When a free ion is placed inside an octahedral cage, the symmetry is reduced from the full rotational SO(3) symmetry of the d-orbital states

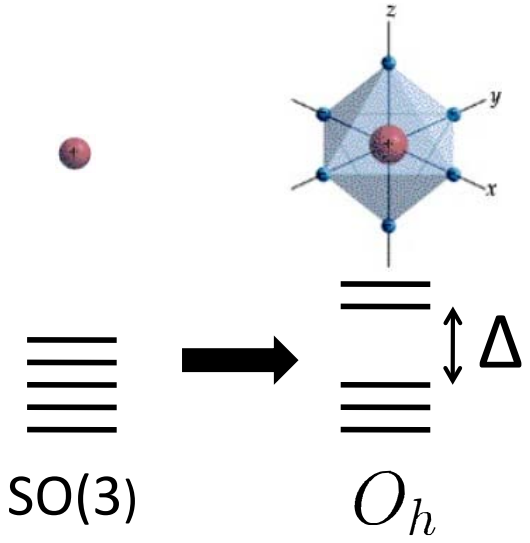

Figure 3.1: Symmetry lowering and level splitting in a cubic crystal field environment. A transition metal ion in free space has a full rotational SO(3) symmetry reduced to octahedral symmetry O_h. The five-fold degenerate d-levels in the vacuum split into a lower-lying triply degenerate t_{2g}, and a higher-lying doubly degenerate e_g set of levels, with an energy difference Δ (called the crystal field splitting) between them.

in the free space, to the symmetry group of the octahedron, SO(3)$\rightarrow O_h$. This consists of all the rotations which take the octahedron into itself. Thus, O_h is a subgroup of the rotation group: $O_h \subset$SO(3). Hence, any representation of SO(3) provides a representation of O_h. However, irreducible representations of SO(3) will become reducible representations of O_h. Thus, the fivefold degeneracy of the d-states is lifted by the crystal field and the d-levels are split into a higher-lying two-fold degenerate e_g and a lower-lying three-fold degenerate t_{2g} manifold, as seen in Fig.3.1, where Δ is the energy difference between them. The oxygen ligands are approximated as point charges siting in the corners of

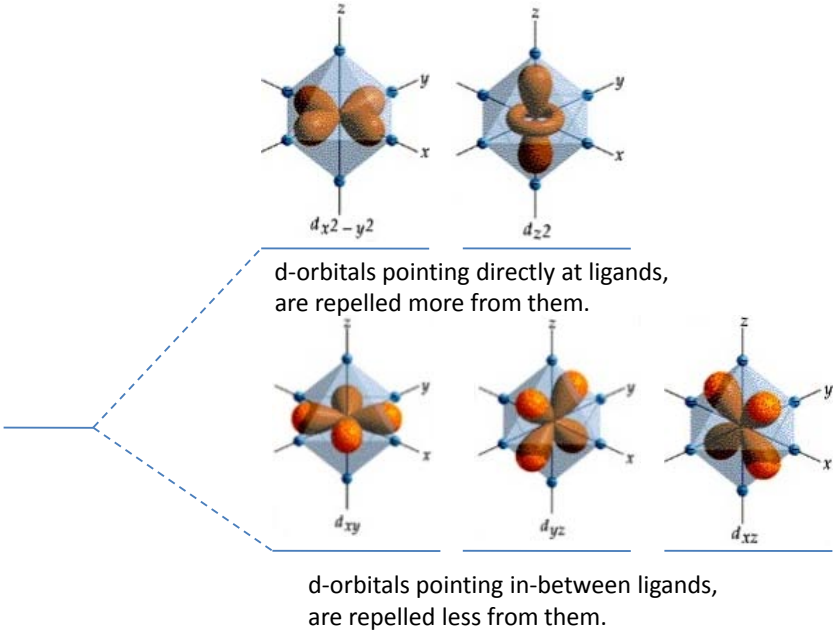

Figure 3.2: The t_{2g} wavefunctions have electron clouds pointing in between the point charges of the ligands, thus they repel less and have lower energy, compared to the e_g states which point towards the oxygen ligands.

the octahedral cages. The t_{2g} d-orbital charge distributions point in between the point charges of the oxygens, and the e_g states point towards the point charges, raising their energy relative to the t_{2g} levels, as shown in Fig. 3.2.

The t_{2g} and e_g orbitals are formed by linear combinations[69] of the spherical harmonics Y_l^m, with the orbital angular momentum $l = 2$. The magnetic quantum number m takes values from $-l$ to l. For t_{2g} these orbitals

states are:

$$
\begin{aligned}
d_{yz} &= -\frac{1}{i\sqrt{2}}(Y_2^1 + Y_2^{-1}), \\
d_{zx} &= -\frac{1}{i\sqrt{2}}(Y_2^1 - Y_2^{-1}), \\
d_{xy} &= \frac{1}{i\sqrt{2}}(Y_2^2 - Y_2^{-2}),
\end{aligned}
\tag{3.1}
$$

and for e_g they are:

$$
\begin{aligned}
d_{3z^2-r^2} &= Y_2^0, \\
d_{x^2-y^2} &= \frac{1}{\sqrt{2}}(Y_2^2 + Y_2^{-2}).
\end{aligned}
\tag{3.2}
$$

The crystal field term in the Hamiltonian, H_{CF}, can be written in a diagonal form as (taking the energy of the t_{2g} states as the zero of energy),

$$
\begin{aligned}
H_{\mathrm{CF}} = \sum_{\sigma=\pm 1/2} & \Delta(|3z^2 - r^2, \sigma\rangle\langle 3z^2 - r^2, \sigma| \\
& + |x^2 - y^2, \sigma\rangle\langle x^2 - y^2, \sigma|),
\end{aligned}
\tag{3.3}
$$

where $\sigma = \pm 1/2$ refers to the spin of the electron in a given orbital state.

3.2 Spin-orbit coupling in a crystal field

The spin-orbit coupling strength is comparable to other energy scales in heavy transition metal oxides.[107, 85, 88] In its presence the orbital angular momentum and spin angular momentum are no longer independently conserved quantities. Moreover, the spin-orbit coupling can also induce mixing between the t_{2g} and e_g manifolds.

The matrix elements of orbital angular momentum l for a single electron in the basis of the t_{2g}, Eq. (3.1), and e_g, Eq.(3.2), states: $\{d_{yz}, d_{zx}, d_{xy}, d_{3z^2-r^2}, d_{x^2-y^2}\}$,

and that of a single electron in atomic p-orbitals in the basis $\{p_x, p_y, p_z\}$ are:[95]

$$l_x = \left[\begin{array}{ccc|cc} 0 & 0 & 0 & -\sqrt{3}i & -i \\ 0 & 0 & i & 0 & 0 \\ 0 & -i & 0 & 0 & 0 \\ \hline \sqrt{3}i & 0 & 0 & 0 & 0 \\ i & 0 & 0 & 0 & 0 \end{array}\right], l'_x = \begin{pmatrix} 0 & 0 & 0 \\ 0 & 0 & -i \\ 0 & i & 0 \end{pmatrix}, \tag{3.4}$$

$$l_y = \left[\begin{array}{ccc|cc} 0 & 0 & -i & 0 & 0 \\ 0 & 0 & 0 & \sqrt{3}i & -i \\ i & 0 & 0 & 0 & 0 \\ \hline 0 & -\sqrt{3}i & 0 & 0 & 0 \\ 0 & i & 0 & 0 & 0 \end{array}\right], l'_y = \begin{pmatrix} 0 & 0 & i \\ 0 & 0 & 0 \\ -i & 0 & 0 \end{pmatrix}, \tag{3.5}$$

$$l_z = \left[\begin{array}{ccc|cc} 0 & i & 0 & 0 & 0 \\ -i & 0 & 0 & 0 & 0 \\ 0 & 0 & 0 & 0 & 2i \\ \hline 0 & 0 & 0 & 0 & 0 \\ 0 & 0 & -2i & 0 & 0 \end{array}\right], l'_z = \begin{pmatrix} 0 & -i & 0 \\ i & 0 & 0 \\ 0 & 0 & 0 \end{pmatrix}. \tag{3.6}$$

By comparing the matrix elements of l in the t_{2g} states with those in the p-states in free atoms, one can map the former $l = 2$ t_{2g}-states onto the latter p-states with $l = 1$ using the relation:

$$\boldsymbol{l}(t_{2g}) = -\boldsymbol{l}(p). \tag{3.7}$$

This relation is called the T-P equivalence, [95, 28] according to which the orbital angular momentum in t_{2g} states is partially quenched from $l = 2$ to $l = 1$. When the cubic crystal field splitting is large, one can neglect the off-diagonal elements between t_{2g} and e_g manifolds and the T-P equivalence can be conveniently used. Note, however, that the spin-orbit coupling generally mixes the t_{2g} and e_g states so if the spin-orbit coupling is large enough compared to

the crystal field splitting (and we will see it can be enhanced by electron-electron interactions) then the mixing may have non-negligible effects.

Using the expression of the orbital angular momentum $\boldsymbol{l}$ of Eqs.(3.4)-(3.6) and the Pauli matrices, we can construct the spin-orbit interaction matrix. Written in the basis $\Psi^\dagger = \{d^\dagger_{xz\uparrow}, d^\dagger_{yz\uparrow}, d^\dagger_{xy\downarrow}, d^\dagger_{3z^2-r^2\downarrow}, d^\dagger_{x^2-y^2\downarrow},$
$d^\dagger_{xz\downarrow}, d^\dagger_{yz\downarrow}, d^\dagger_{xy\uparrow}, d^\dagger_{3z^2-r^2\uparrow}, d^\dagger_{x^2-y^2\uparrow}\}$ it becomes,

$$H_{\mathrm{SOC}} = \frac{\zeta}{2}\Psi^\dagger A \Psi, \tag{3.8}$$

where $\Psi^\dagger$ is a row vector, and Ψ is the complex conjugate column vector, and

$$A = \left(\begin{array}{ccc|cc|ccc|cc}
0 & -i & i & \sqrt{3} & -1 & & & & & \\
i & 0 & -1 & -i\sqrt{3} & -i & & & & & \\
-i & -1 & 0 & 0 & -2i & & & 0 & & \\
\hline
\sqrt{3} & i\sqrt{3} & 0 & 0 & 0 & & & & & \\
-1 & i & 2i & 0 & 0 & & & & & \\
\hline
 & & & & & 0 & i & i & -\sqrt{3} & 1 \\
 & & & & & -i & 0 & 1 & -i\sqrt{3} & -i \\
 & & 0 & & & -i & 1 & 0 & 0 & 2i \\
\hline
 & & & & & -\sqrt{3} & i\sqrt{3} & 0 & 0 & 0 \\
 & & & & & 1 & i & -2i & 0 & 0
\end{array}\right), \tag{3.9}$$

expresses the spin-orbit coupling in the full 10 states of the t_{2g} and e_g manifolds, including spin. The matrix elements are split into terms that act only on the t_{2g}-subspace, $H^{t_{2g}}_{\mathrm{SOC}}$, terms that acts only one the e_g subspace, $H^{e_g}_{\mathrm{SOC}}$, and terms that have matrix elements between t_{2g} and e_g states, $H^{t_{2g}-e_g}_{\mathrm{SOC}}$. The angular momentum matrix elements in the e_g states are zero. Thus, the matrix elements of the $H^{e_g}_{\mathrm{SOC}}$ are zero as well.

The full Hamiltonian of the one-electron states is

$$H = H_{\rm SOC} + H_{\rm CF}. \tag{3.10}$$

In the T-P equivalence one neglects the off-diagonal matrix elements of the angular momentum, $H_{\rm SOC}^{t_{2g}-e_g}$ that connect the t_{2g}-e_g subspaces,

$$H_{\rm TP} = H_{\rm SOC}^{t_{2g}} + H_{\rm SOC}^{e_g} + H_{\rm CF}, \tag{3.11}$$

which is given from the expressions above without the $t_{2g} - e_g$ mixing. Diagonalizing Eq.(3.11), the states evolve as shown in Fig. 3.3 via the green lines. In particular, the e_g states are not affected by the spin-orbit coupling, and are separated from the t_{2g} states by an energy difference Δ. On the other hand, the t_{2g} states are split into eigenstates of energy $\epsilon_{J_{\rm eff}=\frac{1}{2}} = \zeta$:

$$\begin{aligned} |J_{\rm eff} = \frac{1}{2}, m = -\frac{1}{2}\rangle &= \frac{1}{\sqrt{3}}|d_{yz\uparrow}\rangle - \frac{i}{\sqrt{3}}|d_{xz\uparrow}\rangle - \frac{1}{\sqrt{3}}|d_{xy\downarrow}\rangle, \\ |J_{\rm eff} = \frac{1}{2}, m = \frac{1}{2}\rangle &= \frac{1}{\sqrt{3}}|d_{yz\downarrow}\rangle + \frac{i}{\sqrt{3}}|d_{xz\downarrow}\rangle + \frac{1}{\sqrt{3}}|d_{xy\uparrow}\rangle, \end{aligned} \tag{3.12}$$

and eigenstates of energy $\epsilon_{J_{\rm eff}=\frac{3}{2}} = -\frac{\zeta}{2}$:

$$\begin{aligned} |J_{\rm eff} = \frac{3}{2}, m = -\frac{3}{2}\rangle &= \frac{1}{\sqrt{2}}|d_{yz\downarrow}\rangle - \frac{i}{\sqrt{2}}|d_{xz\downarrow}\rangle, \\ |J_{\rm eff} = \frac{3}{2}, m = \frac{3}{2}\rangle &= -\frac{1}{\sqrt{2}}|d_{yz\uparrow}\rangle - \frac{i}{\sqrt{2}}|d_{xz,\uparrow}\rangle, \\ |J_{\rm eff} = \frac{3}{2}, m = -\frac{1}{2}\rangle &= \frac{1}{\sqrt{6}}|d_{yz\uparrow}\rangle - \frac{i}{\sqrt{6}}|d_{xz\uparrow}\rangle + \sqrt{\frac{2}{3}}|d_{xy\downarrow},\rangle \\ |J_{\rm eff} = \frac{3}{2}, m = \frac{1}{2}\rangle &= -\frac{1}{\sqrt{6}}|d_{yz\downarrow}\rangle - \frac{i}{\sqrt{6}}|d_{xz\downarrow}\rangle + \sqrt{\frac{2}{3}}|d_{xy\uparrow}\rangle. \end{aligned} \tag{3.13}$$

The results in Eq.(3.12) and Eq.(3.13) are commonly used in the literature. Beyond the T-P equivalence one needs to consider the neglected mixing of the

t_{2g}-e_g subspaces of the spin-orbit coupling $H_{\rm SOC}^{t_{2g}-e_g}$. Here, we consider it as a perturbation $H_1 = H_{\rm SOC}^{t_{2g}-e_g}$ to the $H_0 = H_{\rm TP}$ T-P equivalence terms of Eq. (3.11).

Writing $H_0 + H_1$ in the diagonal basis of H_0, we have in the basis

$\Phi^\dagger = \{|\frac{1}{2}, -\frac{1}{2}\rangle, |\frac{3}{2}, +\frac{3}{2}\rangle, |d_{3z^2-r^2}, -\frac{1}{2}\rangle, |\frac{3}{2}, -\frac{1}{2}\rangle,$
$|d_{x^2-y^2}, -\frac{1}{2}\rangle, |\frac{1}{2}, +\frac{1}{2}\rangle, |\frac{3}{2}, -\frac{3}{2}\rangle, |d_{3z^2-r^2}, +\frac{1}{2}\rangle, |\frac{3}{2}, +\frac{1}{2}\rangle,$
$|d_{x^2-y^2}, +\frac{1}{2}\rangle\}$,

$$H_0 + H_1 = \frac{\zeta}{2}\Phi^\dagger B \Phi \tag{3.14}$$

where $\Phi^\dagger$ is a row vector, and Φ is a complex conjugate column vector,

$$B = \left(\begin{array}{ccccc|ccccc} 2 & 0 & 0 & 0 & 0 & & & & & \\ \hline 0 & -1 & i\sqrt{6} & 0 & 0 & & & & & \\ 0 & -i\sqrt{6} & \delta & 0 & 0 & & & 0 & & \\ \hline 0 & 0 & 0 & -1 & -i\sqrt{6} & & & & & \\ 0 & 0 & 0 & i\sqrt{6} & \delta & & & & & \\ \hline & & & & & 2 & 0 & 0 & 0 & 0 \\ & & & & & \hline 0 & -1 & -i\sqrt{6} & 0 & 0 \\ & & 0 & & & 0 & i\sqrt{6} & \delta & 0 & 0 \\ & & & & & \hline 0 & 0 & 0 & -1 & i\sqrt{6} \\ & & & & & 0 & 0 & 0 & -i\sqrt{6} & \delta \end{array}\right), \tag{3.15}$$

where $\delta = 2\Delta/\zeta$. Note that H_0 are the diagonal matrix elements, and H_1 are the non-diagonal ones, of the B-matrix, Eq.(3.15). One sees that there are no matrix elements involving $|J_{\rm eff} = \frac{1}{2}, m = \pm\frac{1}{2}\rangle$ states. Thus they remain unaffected. However, the $|J_{\rm eff} = \frac{3}{2}\rangle$ and e_g subspaces are mixed. Thus, going beyond the T-P equivalence involves mixing the upper and the lower states as seen in Fig. 3.3 indicated with red lines. Hence the evolution of the t_{2g}

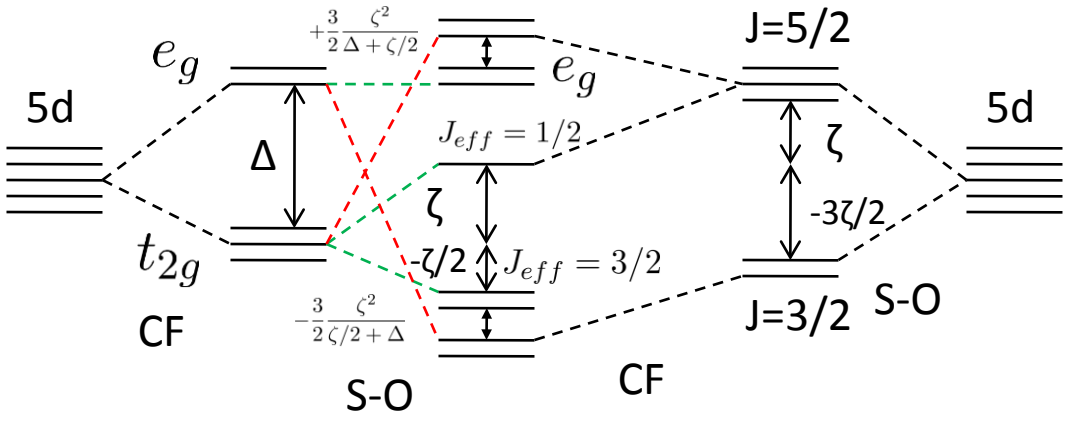

Figure 3.3: Evolution of d-orbital states under a cubic crystal field and spin-orbit coupling. The green lines correspond to the commonly used T-P equivalence that neglects t_{2g}-e_g mixing by spin-orbit coupling. The red lines indicate an extra mixing contribution going beyond TP equivalence, of the $J_{\text{eff}} = 3/2$ by a factor of $\pm i\sqrt{\frac{3}{2}}\frac{\zeta}{\zeta/2+\Delta}|e_g\rangle$, and to the upper quartet e_g by the same factor of $J_{\text{eff}} = 3/2$ states, as shown in Eqs. (3.16),(3.17). The energies of the lower quartet is shifted down by $-\frac{3}{2}\frac{\zeta^2}{\zeta/2+\Delta}$, and of the upper quartet is shifted up by $+\frac{3}{2}\frac{\zeta^2}{\zeta/2+\Delta}$. Notice that the $J_{\text{eff}} = 1/2$ states are not affected.

and e_g states in the presence of spin-orbit coupling is more complex than the commonly used T-P equivalence assumes.

To first order in the wavefunctions, the lower quartet is modified by

$$\begin{aligned} |J_{\text{eff}} = \frac{3}{2}, m = \pm\frac{3}{2}\rangle &\pm i\sqrt{\frac{3}{2}}\frac{\zeta}{\zeta/2+\Delta}|d_{3z^2-r^2}, \mp\frac{1}{2}\rangle, \\ |J_{\text{eff}} = \frac{3}{2}, m = \pm\frac{1}{2}\rangle &\pm i\sqrt{\frac{3}{2}}\frac{\zeta}{\zeta/2+\Delta}|d_{x^2-y^2}, \pm\frac{1}{2}\rangle, \end{aligned} \tag{3.16}$$

and to second order in energy we find a shift by $-\frac{3}{2}\frac{\zeta^2}{\zeta/2+\Delta}$. The upper quartet

is modified by

$$
\begin{aligned}
&|d_{3z^2-r^2}, \mp\frac{1}{2}\rangle \pm i\sqrt{\frac{3}{2}}\frac{\zeta}{\Delta+\zeta/2}|J_{\text{eff}}=\frac{3}{2}, m=\pm\frac{3}{2}\rangle, \\
&|d_{x^2-y^2}, \pm\frac{1}{2}\rangle \pm i\sqrt{\frac{3}{2}}\frac{\zeta}{\Delta+\zeta/2}|J_{\text{eff}}=\frac{3}{2}, m=\pm\frac{1}{2}\rangle,
\end{aligned}
\tag{3.17}
$$

with shifts in energies of $+\frac{3}{2}\frac{\zeta^2}{\Delta+\zeta/2}$. Note for $\zeta = 0.5eV$, $\Delta = 3eV$ typical values for 5d systems, the mixing is $\sqrt{\frac{3}{2}}\frac{\zeta}{\zeta/2+\Delta} \approx 0.19$, a 20% effect.

3.3 Inclusion of Electron-electron interaction

Having treated the octahedral crystal field H_{CF} in Sec. 3.1 and the spin-orbit interaction H_{SOC} in Sec. 3.2, we are now ready to add the electron-electron interactions, $H_{\text{e-e}}$. We are especially interested in how electron-electron interactions will interplay with the t_{2g}-e_g mixing highlighted in the previous section. This mixing is often ignored in the literature.

3.3.1 T-P equivalence in 3d systems

In the presence of electron-electron interactions, the Hamiltonian of the ion is

$$H = H_{\text{CF}} + H_{\text{SOC}} + H_{\text{e-e}}, \tag{3.18}$$

which contains the crystal field part H_{CF}, the spin-orbit part H_{SOC}, and the interacting part $H_{\text{e-e}}$. Within the crystal field approximation several different cases arise: weak, intermediate, and strong crystal field.[28, 112] The simplest is the weak crystal field case,

$$H_{\text{e-e}} >> H_{\text{CF}} > H_{\text{SOC}},$$

where the interacting part $H_{\mathrm{e-e}}$ is much larger than the crystal field terms H_{CF}, and the spin-orbit coupling is smaller still. The intermediate crystal field case is

$$H_{\mathrm{e-e}} > H_{\mathrm{CF}} > H_{\mathrm{SOC}},$$

which follows the same order, but the crystal fields are no longer much weaker than the electron-electron interactions.

In 3d systems, the on-site Coulomb interaction is on the order of U= 3-10 eV, crystal fields are Δ=1.5-2 eV, Hund's coupling is J_H=0.8-0.9 eV, and the spin-orbit coupling is in the order of 0.01eV-0.1eV (λ=0.02 eV for Ti, and λ= 0.07 eV for heavier Co).[69] Thus, 3d systems fall into the weak and intermediate crystal field regimes.

Following the above scheme from the most dominant term to the weakest, we have the interacting Hamiltonian, which is rotationally invariant with spin independent (Coulomb) interactions. Thus, the orbital angular momentum L and spin S are conserved quantum numbers and can be used to label the states. The next important term, the crystal field, is not rotationally invariant and mixes different L terms. Because the energy difference of different L terms is 3-10 eV, and the crystal field is 1.5-2 eV, as a first approximation we neglect the mixing of different L values, and we consider the effect of crystal field splitting within the ground state manifold of the L term, following the conventions of the field. The smallest term in the hierarchy, the spin-orbit coupling, mixes states of different crystal field levels (t_{2g} and e_g in our case),

and terms of different L levels as well, but we neglect those and only include the splitting within the ground state multiplet of crystal field split levels.

Since the electron-electron interaction is the most dominant term in the above hierarchy and the crystal field mixes states within a given (L, S) term, Hund's first and second rule are valid even in the presence of crystal fields. This means that 3d ions can form high spin structures, where the 4^{th} and 5^{th} electrons go into the e_g orbitals, as indicated from Hund's first rule of maximal spin. The condition for the low-spin to high-spin transition where the 4^{th} electron prefers to go into the e_g orbitals is approximately $\Delta_{\mathrm{CF}} \approx 3J_H$ (larger J_H favors a high-spin configuration, smaller J_H a low-spin configuration). Since Δ_{CF}=1.5-2 eV and J_H=0.8-0.9eV, this condition is satisfied. However, since crystal fields dominate over the spin-orbit coupling, Hund's third rule ceases to apply. This means that though L and S remain valid quantum numbers, and their values are still given by Hund's first and second rule, the total angular momentum J is no longer a good quantum number.

In the case of strong crystal fields,

$$H_{\mathrm{CF}} \geq H_{\mathrm{e-e}} > H_{\mathrm{SOC}},$$

the crystal fields are comparable to (or larger than) the electron-electron interaction giving rise to Hund's first and second rule. Thus, they even mix states belonging to different (L, S) terms. It is quite usual to find strong crystal fields in 4d and 5d transition metal compounds. On the other hand, there are only rare instances of insulating solids where 3d ions are subject to such

strong crystal fields that even Hund's first rule is put out of action. In next section we will more extensively discuss the case of 4d and 5d systems.

Regardless of the particular energy hierarchy that is relevant, one has

$$[H_{\mathrm{e-e}} + H_{\mathrm{CF}}, \boldsymbol{S}^2] = 0,\ [H_{\mathrm{e-e}} + H_{\mathrm{CF}}, S^z] = 0, \tag{3.19}$$

so that $\boldsymbol{S}^2$ and S^z commute with $H_{\mathrm{e-e}}$ and H_{CF} since they are spin independent. As a consequence, $H_{\mathrm{e-e}} + H_{CF}$ has a ground state with well defined spin quantum number. This holds for arbitrary strength of the Coulomb interaction (including none at all).

Summarizing, the ground state multiplet of $H_{e-e} + H_{\mathrm{CF}}$ is only t_{2g} (for up to 6 electrons) if the ion is in the low spin configuration. For finite spin-orbit coupling, S and S^z are no longer good quantum numbers. As discussed in Sec. 3.2, H_{SOC} splits into $H_{\mathrm{SOC}}^{t_{2g}} + H_{\mathrm{SOC}}^{t_{2g}-e_g}$ ($H_{\mathrm{SOC}}^{e_g} = 0$). Since in 3d systems the spin-orbit coupling is on the order of 0.02-0.07 eV and crystal fields $\Delta = 1.5 - 2\mathrm{eV}$, the mixing of t_{2g} and e_g states in the low-spin configuration will be on the order of $\zeta/\Delta \approx 0.02eV/2eV = 1/100$ and can be neglected to first order. Consequently, it is a good approximation in 3d systems to neglect the off-diagonal matrix elements of angular momentum in t_{2g} systems and use the T-P equivalence. This is no longer the case for the heavier transition elements.

3.3.2 Limitations of the T-P equivalence in 4d and 5d systems

As one moves from 3d to 4d to 5d transition metals the outermost electronic wavefunctions become more and more extended, and thus scale of

the typical Hubbard U becomes smaller, reaching down to U=0.5-3eV in 5d elements. The Hund's coupling is reduced as well, to J_H=0.6-0.7 eV in 4d elements and to J_H=0.5eV in 5d elements. Similarly, the larger spatial extent of the outermost electronic states increase the crystal field splitting to Δ=1-5eV in 5d elements. Heavier elements have larger spin-orbit coupling, and its value is increased to $\zeta = 0.1 - 1$eV in 5d elements. These values bring the 4d/5d elements into the strong crystal field scenario mentioned in the previous section, where the energy scale of the crystal fields is greater than or comparable to the electron interactions.

Since $H_{e-e} \approx H_{\mathrm{CF}}$ there is mixing of (L, S) terms. Due to stronger crystal fields and smaller Hund's coupling J_H, even Hund's first rule of maximal spin is violated in 4d and 5d systems. Since $\Delta < 3J_H$ (the approximate criterion with $\Delta = 3$eV,J_H=0.5eV) is not satisfied, a low-spin t_{2g} ground state configurations are preferred. However, a crucial difference of 4d/5d systems relative to their 3d counterparts is the strong spin-orbit coupling.

To help understand the relevant physics, it is useful to briefly consider 4f systems where,

$$H_{\mathrm{e-e}} > H_{\mathrm{SOC}} > H_{\mathrm{CF}},$$

since the spin-orbit coupling is greater than crystal fields, Hund's third rule, takes precedence over lattice effects. Crystal field mixing of different J-manifolds are dropped in a first approximation and crystal field effects are considered only within a given J-manifold.

Returning to 5d systems, we have the following hierarchy:

$$H_{\mathrm{CF}} \approx H_{\mathrm{e-e}} \gtrapprox H_{\mathrm{SOC}}.$$

In this scenario, which occurs mainly in 5d systems and is intermediate to 3d systems and 4f systems, all energy scales are comparable, with spin-orbit coupling smaller, but still the same order of magnitude as the others. None of the approximations used in 3d and 4f systems work in this regime. Therefore, in order to study this regime in detail we turn to an exact diagonalization study.

As mentioned in Sec.3.2, the off-diagonal elements of spin-orbit coupling mix the t_{2g} and e_g states. In 5d systems spin-orbit coupling is an order of magnitude greater than 3d systems, and although crystal fields are larger as well, they remain of the same order of magnitude. Thus, the first order correction in perturbation theory of the wavefunction due to t_{2g}-e_g mixing is of the order of $\zeta/\Delta \approx 0.5/3 = 1/6$. Therefore, it is not as small as in 3d systems and neglecting the e_g states by using the T-P equivalence will result in more dramatic differences from the full t_{2g}-e_g space of states.

3.4 Model and calculations

To study the mixing between t_{2g} and e_g orbitals, we use a five-orbital model, taking in account all the d-orbitals. Depending on the electron filling, we compare the five-orbital model with a three-orbital t_{2g}-only model, or to a two-orbital e_g-only model. We compute various observables as a function

of the mixing parameter (of t_{2g} and e_g states), which is the bare spin-orbit coupling strength, ζ. We do this for every electron filling, from one electron to nine electrons.

We model the electron-electron interaction with the Kanamori Hamiltonian,[69]

$$\begin{aligned} & H^{(Kanamori)} \\ & = U \sum_m \hat{n}_{m\uparrow}\hat{n}_{m\downarrow} + U' \sum_{m\neq m'} \hat{n}_{m\uparrow}\hat{n}_{m'\downarrow} \\ & + (U' - J_H) \sum_{m<m',\sigma} \hat{n}_{m\sigma}\hat{n}_{m'\sigma} - J \sum_{m\neq m'} d^\dagger_{m\uparrow} d_{m\downarrow} d^\dagger_{m'\downarrow} d_{m'\uparrow} \\ & + J_H \sum_{m\neq m'} d^\dagger_{m\uparrow} d^\dagger_{m\downarrow} d_{m'\downarrow} d_{m'\uparrow}, \end{aligned} \tag{3.20}$$

where $d(d^\dagger)$ is the electron annihilation(creation) operator, $d_{yz}, d_{zx}, d_{xy}, d_{3z^2-r^2}, d_{x^2-y^2}$ are associated with labels $m, m' = 1, 2, 3, 4, 5$ respectively, and $\hat{n}_{m\sigma} \equiv d^\dagger_{m\sigma} d_{m\sigma}$. For the three orbital t_{2g}-only model $m, m' = 1, 2, 3$ and for the two orbital e_g-only model $m, m' = 4, 5$. We assume that the relation $U = U' + 2J_H$ is satisfied, which is a good approximation for many materials.[69] We take $U' = 1$eV in all calculations, leaving only one free parameter, the Hund's coupling J_H. For the five-orbital model, Eq.(3.20) is supplemented by $H_{\rm CF}$, which is given in the Eq. (3.3). The full Hamiltonian we consider is then

$$H = H^{(Kanamori)} + H_{\rm CF} + H_{\rm SOC}, \tag{3.21}$$

with m, m' =1-5. For the three-orbital t_{2g}-only model $H = H^{(Kanamori)} + H^{t_{2g}}_{\rm SOC}$ with $m, m' = 1, 2, 3$, and for the two-orbital e_g-only model $H = H^{(Kanamori)}$ with $m, m' = 4, 5$. Using exact diagonalization we will compare the results

of the full Hamiltonian in Eq.(3.21) with the t_{2g}-only model and the e_g-only model.

We calculate expectation values of different operators $\hat{O}$, $O \equiv \langle\psi_0|\hat{O}|\psi_0\rangle$, where ψ_0 is the ground state of the many-electron system. We compute the expectation value of the total spin angular momentum $\boldsymbol{S}^2$, the total orbital angular momentum $\boldsymbol{L}^2$, the zero, the single, and the double occupancies of different orbitals defined by[71]

$$\hat{Z}_i \equiv 1 - n_{i\uparrow} - n_{i\downarrow} + n_{i\uparrow}n_{i\downarrow}, \tag{3.22}$$

$$\hat{S}_i \equiv n_{i\uparrow} + n_{i\downarrow} - 2n_{i\uparrow}n_{i\downarrow}, \tag{3.23}$$

$$\hat{D}_i \equiv n_{i\uparrow}n_{i\downarrow}, \tag{3.24}$$

where i stands for the orbital index. The amplitudes of the spin, orbital, and total angular magnetic moments, respectively, are defined by $M_s/\mu_B = |\sum_i s_z^i|$, $M_l/\mu_B = |\sum_i l_z^i|$, and $M_{tot}/\mu_B = |\sum_i (l_z^i + s_z^i)|$, where s_z^i and l_z^i are the z components of the spin and orbital angular momenta of the i^{th} electron respectively, and the effective spin-orbit interaction is

$$\overline{\zeta} = -\frac{1}{\zeta} H_{\mathrm{SOC}}, \tag{3.25}$$

$$\overline{\zeta}_{t_{2g}} = -\frac{1}{\zeta} H_{\mathrm{SOC}}^{t_{2g}}, \tag{3.26}$$

$$\overline{\zeta}_{t_{2g}-e_g} = -\frac{1}{\zeta} H_{\mathrm{SOC}}^{t_{2g}-e_g}, \tag{3.27}$$

where $\overline{\zeta}$ is in units of $\hbar^2$.

We note that the effective spin-orbit coupling can be probed experimentally through X-ray absorption spectroscopy (XAS) measurements.[99, 98, 103]

Core electrons from the occupied states $2p_{1/2}$ and $2p_{3/2}$ are excited to the unoccupied states $5d_{3/2}$ and $5d_{5/2}$, respectively, since these are allowed from the selection rules $\Delta J = 0, \pm 1$. These absorption processes are referred to as the intensity peaks I_{L_2} and I_{L_3}, respectively. Van de Laan and Thole[99, 98, 103] have shown that the ratio of the integrated intensities (area) of the peaks, $BR = I_{L_3}/I_{L_2}$ [called the branching ratio (BR)] is directly related to the ground state expectation value of the spin-orbit coupling $\langle \boldsymbol{L} \cdot \boldsymbol{S} \rangle$ (which we call $\overline{\zeta}$), through the relation $BR = (2 + r)/(1 - r)$, where $r = \langle \boldsymbol{L} \cdot \boldsymbol{S} \rangle / \langle n_h \rangle$, and $\langle n_h \rangle$ is the average number of holes in the unoccupied d-states (including the full five d orbitals).

When the spin-orbit coupling is zero, the J=3/2 and J=5/2 d-states are degenerate (see right side of Fig. 3.3), and the ratio of the intensities I_{L_3}/I_{L_2} is equal to the ratio of the occupied states $2p_{3/2}$ and $2p_{1/2}$ which is 2:1. This yields a branching ratio of $BR = I_{L_3}/I_{L_2} = 2$. A deviation from this value is a clear indication of strong spin-orbit coupling, and can give information on the nature of the ground state.

Since the effective spin-orbit coupling is a local property of the ion, a single-site calculation is expected to capture the essential physics of the experimental measurements. In our exact diagonalization (ED) calculations, we place an infinitesimal magnetic field in the z-direction, H^z of the order of 10^{-6} eV, in order to lift the degeneracy of the ground state, and obtain a unique expression for the eigenvectors of the ground state. We have verified this small value does not numerically change the expectation values we compute.

3.5 Exact Diagonalization Results

3.5.1 Comparison of t_{2g}-e_g model with t_{2g} only model

For electron filling from one to six electrons, we will compare the results of the full t_{2g}-e_g model with the t_{2g} only model.

3.5.1.1 1 electron

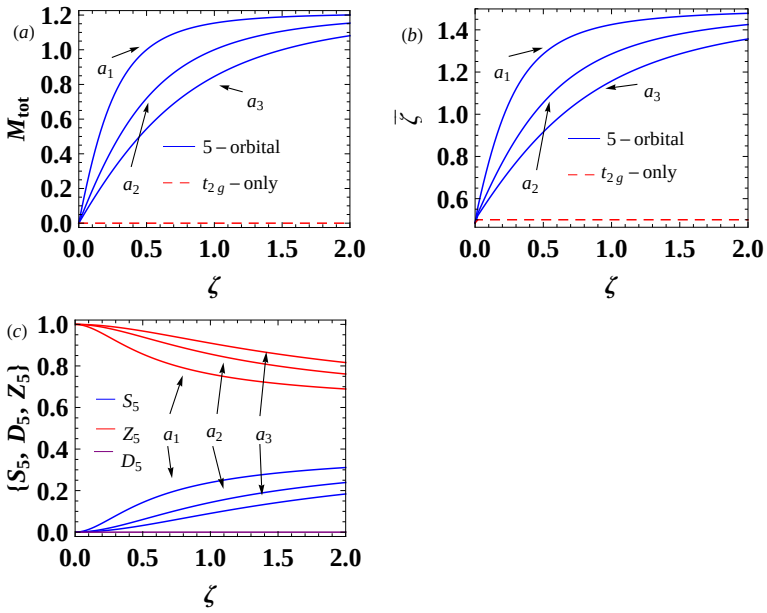

Figure 3.4: Exact diagonalization 1 electron results. (a) Total magnetic moment, M_{tot}, (b) effective spin-orbit coupling, $\bar{\zeta}$, (c) single S_5, zero Z_5, and double D_5 occupancies of the e_g $d_{x^2-y^2}$-orbital, for different crystal field values $a_1 : \Delta = 1$ eV,$a_2 : \Delta = 2$ eV, and $a_3 : \Delta = 3$ eV. Note there is substantial enhancement of the total magnetic moment and effective spin-orbit coupling in the t_{2g}-e_g model relative to the t_{2g} only model.

In the t_{2g}-only model, we have $l = 1$ for the orbital angular momentum, and s=1/2. Thus, there is no magnetic moment M=-l+2s=0, since due to spin-

orbit coupling, orbital angular momentum and spin angular momentum favor an antiparallel alignment. This is what we see in Fig.3.4(a). However, the quenching of the orbital angular momentum is overestimated in the t_{2g}-only model. As we see in the 5-orbital model (for which $l = 2$), the restoration of orbital angular momentum due to spin-orbit coupling becomes significant. We compute the total magnetic moment for crystal field energy $\Delta = 1, 2, 3$ eV and find it is reduced as the crystal field splitting is increased. A significant moment remains, for example, for $\Delta = 3$ eV and $\zeta = 0.5$ eV.

As shown in Sec. 3.2 using perturbation theory for a single electron, the off diagonal t_{2g}-e_g matrix elements of the spin-orbit coupling creates a small occupancy of e_g-orbitals in the ground state. This is seen in Fig.3.4(b), with the single, zero, and double e_g-occupancy of the e_g $x^2 - y^2$-orbital, for three different crystal field energies $\Delta = 1, 2, 3$ eV (the single, zero, and double e_g-occupancy of the $3z^2 - r^2$-orbital are zero). As expected, the occupancies are reduced as the crystal field energy is increased, and they are increased as the spin-orbit coupling strength is increased. In Fig.3.4(c) we see for the t_{2g} only model $\overline{\zeta}_{t_{2g}} = 0.5$, coming from $\frac{1}{\zeta}\langle H_{SO}^{t_{2g}}\rangle$ in the $|J = 3/2\rangle$ ground state. In the 5-orbital model, by using Eq.(3.16) in calculating the extra contribution from $\frac{1}{\zeta}\langle H_{SO}^{t_{2g}-e_g}\rangle$ of the off-diagonal matrix elements of matrix B in Eq.(3.15), we get $\frac{1}{\zeta}\langle H_{SO}^{t_{2g}-e_g}\rangle = 3\frac{\zeta}{\zeta/2+\Delta}$, thus $\overline{\zeta} \equiv -\frac{1}{\zeta}\langle H_{SO}\rangle = -\frac{1}{\zeta}\langle H_{SO}^{t_{2g}}\rangle - \frac{1}{\zeta}\langle H_{SO}^{t_{2g}-e_g}\rangle = 0.5 + 3\frac{\zeta}{\zeta/2+\Delta}$ which gives the correct trend shown in Fig.3.4(c), explaining the missing part not captured from the t_{2g}-only model.

3.5.1.2 2 electrons

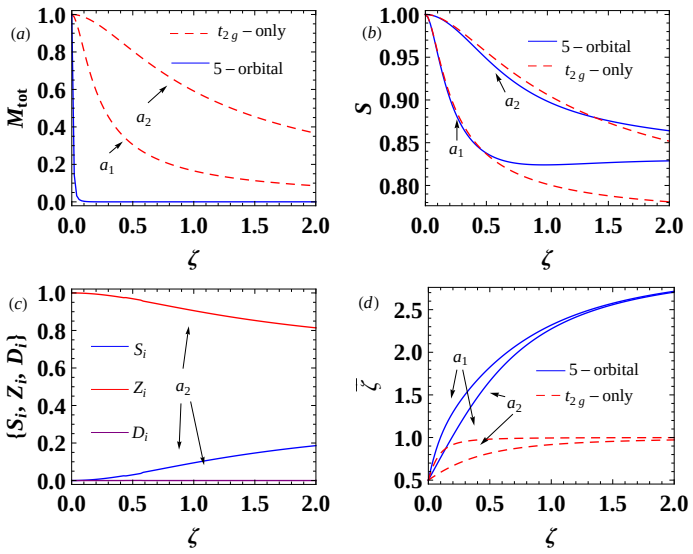

Figure 3.5: Exact diagonalization 2 electron results for crystal field splitting $\Delta = 3$ eV. (a) Total magnetic moment M_{tot}, (b) spin quantum number S, (c) single S_i, zero Z_i, double D_i occupancy per e_g-orbital, (d) effective spin-orbit coupling $\overline{\zeta}$. Different Hund's coupling parameters $a_1 : J_H = 0.1eV, a_2 : J_H = 0.5eV$ are used.

In the t_{2g}-only model, for zero spin-orbit coupling ($\zeta = 0$) $l = 1$ and $s = 1$. Thus, a non-zero magnetic moment $M_{tot} = -l + 2s = 1$ is achieved. However, for $\zeta = 0$ the 5-orbital model gives $l = 2.7$ because the crystal field mixes different (L, S) terms (with the same $s = 1$ as the t_{2g}-only model, following Hund's first rule) as discussed in Sec. 3.3.2. At $\zeta = 0$ one has the same total magnetic moment as with the t_{2g}-only model, $M_{tot} = l_z + 2s_z = 1$.

However, when the spin-orbit coupling is turned on, $l_z = 0$ and $s_z = 0$, so the magnetic moment abruptly plunges to zero, consistent with the approximate rule $l \approx 2$, $s = 1$, $M_{tot} = -l + 2s = 0$. In Fig.3.5(a) we see for

the t_{2g}-only model with $J_H = 0.1$ eV the magnetic moment is reduced as the spin-orbit coupling is increased. This can be understood as a competition with the Hund's coupling aligning the spins of the electrons, while the spin-orbit coupling "unaligns" them as it tries to align the spin with the orbital motion. Thus, for $J_H = 0.5$ eV where Hund's coupling is stronger, the effect of the spin-orbit coupling is weaker.

In Fig.3.5(b) we see the spin quantum number S, for $J_H = 0.1, 0.5$ eV for the t_{2g}-only and for the 5-orbital model as a function of the spin-orbit coupling. We see that for the smaller Hund's coupling the reduction of the spin is greater, due to the same explanation given for the magnetic moment. The two models match for small spin-orbit coupling, but for $J_H = 0.1$ eV a deviation between them appears for $\zeta > 0.5$ eV. In Fig. 3.5(c) we see the single, zero and double e_g occupancy per e_g orbital, for crystal field energy $\Delta = 3$ eV and $J_H = 0.5$ eV is increased as the spin-orbit coupling is increased. While the curves are similar to the one-electron case, the total result is roughly doubled since it is per e_g-orbital.

In Fig.3.5(d) the effective spin-orbit coupling $\overline{\zeta}$ is shown for $J_H = 0.1, 0.5$ eV for the t_{2g}-only model and for the 5-orbital model. As the Hund's coupling is increased, the effective spin-orbit coupling is decreased. As the crystal field is increased, the results from the two models approach each other. However, $\overline{\zeta}$ is quite robust even for $\Delta = 3$ eV, $\zeta = 0.5$ eV, and $J_H = 0.1$ eV where the t_{2g}-only model gives $\overline{\zeta} \approx 1$ and the 5-orbital model gives $\overline{\zeta} \approx 1.8$.

We can understand these results qualitatively using a single particle

analysis. By taking the ground state to be a tensor product of the single-particle eigenstates given in Sec. 3.2 for the t_{2g}-only model and the 5-orbital model, we get for two electrons, $\overline{\zeta} \equiv -\frac{1}{\zeta}\langle H_{SO}\rangle = -\frac{1}{\zeta}\langle H_{SO}^{t_{2g}}\rangle - \frac{1}{\zeta}\langle H_{SO}^{t_{2g}-e_g}\rangle = 1 + 2 \times 3\frac{\zeta}{\zeta/2+\Delta}$. The weaker the electronic correlations (*i.e.* $J_H = 0.1$ eV), the closer one gets to this single electron result. Using this result for the t_{2g}-only model gives $\overline{\zeta}_{t_{2g}} = -\frac{1}{\zeta}\langle H_{SO}^{t_{2g}}\rangle = 1$ and the 5-orbital model gives an extra contribution $\overline{\zeta}_{t_{2g}-e_g} = -\frac{1}{\zeta}\langle H_{SO}^{t_{2g}-e_g}\rangle = 2 \times 3\frac{\zeta}{\zeta/2+\Delta}$, which for reasonable values in the 5d elements ($i.e\ \Delta = 3\ eV, \zeta = 0.5$ eV), gives for the 5-orbital model $\overline{\zeta}_{5-orbital} = \overline{\zeta}_{t_{2g}} + \overline{\zeta}_{t_{2g}-e_g} = 1 + 0.96 = 1.96$ close to what is observed in Fig.3.5(d). We also see that the two models match at $\zeta < 0.1$. Thus, for 3d systems the T-P equivalence is a good approximation even for the most dramatically different expectation value, the effective spin-orbit coupling.

3.5.1.3 3 electrons

For zero spin-orbit coupling for the t_{2g}-only model we have $l = 0$, and $s = 3/2$, while for the 5-orbital model $l = 3$ and $s = 3/2$, as predicted from Hund's first rule for maximal spin. With this in mind, we turn our attention first to the total magnetic moment, which we expect to reduce with increasing spin-orbit coupling because the spin-orbit coupling tends to "unalign" the spins. This will be true for both models. However, comparing our results for the total magnetic moment with Ref. [71] where a t_{2g}-only model was used, we find a significant difference using a 5-orbital model, as seen in Fig.3.6(a). Thus, the quenching of orbital angular momentum is underestimated in the

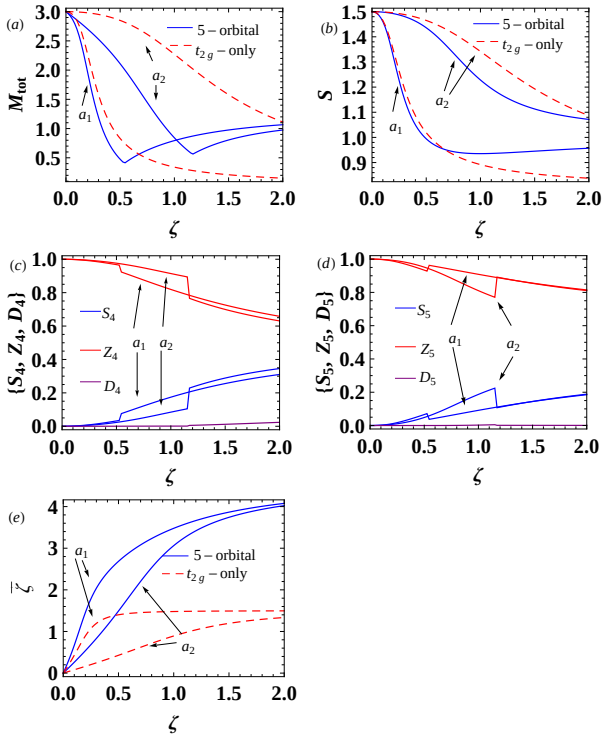

Figure 3.6: Exact diagonalization 3 electron results for crystal field splitting $\Delta = 3$ eV. (a) Total magnetic moment M_{tot}. (b) Spin quantum number S. (c) Single S_4, zero Z_4, and double D_4 occupancies of the $d_{3z^2-r^2}$ orbitals. (d) Single S_5, zero Z_5, and double D_5 occupancies of the $d_{x^2-y^2}$ orbitals. (e) Effective spin-orbit coupling, $\bar{\zeta}$. Different Hund's coupling parameters a_1 : $J_H = 0.1eV, a_2 : J_H = 0.5eV$.

t_{2g}-only model. There is an increased l_z and decreased s_z in the 5-orbital model compared to the t_{2g}-only model. When ($\zeta > J_H$) the magnetic moment is reduced rapidly with spin-orbit coupling. For $J_H = 0.1$, when ζ becomes greater than J_H ($\zeta > J_H$) spin-orbit coupling overcomes the aligning of the spins caused from Hund's coupling. For $J_H = 0.1$ eV there is a transition at $\zeta \approx 0.5$ eV, and for $J_H = 0.5$ eV at $\zeta \approx 1.2$ eV. The transitions can be

seen from the discontinuity in the e_g occupancies where some small electron occupancy is transferred from one e_g orbital to the other (the average e_g-occupancy remains constant). There is also some transfer of double occupancy from two t_{2g} orbitals to the third one, where the average t_{2g}-occupancy remains constant as well.

As one increases the spin-orbit coupling strength, the total spin is more affected compared to the two-electron system, because it is tightly connected to the orbital angular momentum. The S of the t_{2g} and 5-orbital models begin to deviate with increasing strength of the spin-orbit coupling, as seen in the Fig.3.9(b). For small Hund's coupling this deviation is small, and for larger Hund's coupling this deviation is larger.

For the effective spin-orbit coupling, there is a more dramatic difference between the two models compared to the two-electron system, where for $\zeta =$ 0.5 eV and $\Delta = 3$ eV we have $\overline{\zeta}_{t_{2g}-only}$=1.5 for the t_{2g}-only model, while for the 5-orbital model $\overline{\zeta}_{5-orbital}$=2.8. Using a single particle analysis similar to that of two-electron filling, we get $\overline{\zeta}_{t_{2g}} = 1.5, \overline{\zeta}_{5-orbital} = 1.5 + 3 \times 3\frac{\zeta}{\zeta/2+\Delta}$, which is very close to what we observe in Fig.3.6(e) for $J_H = 0.1$ eV, while for $J_H = 0.5$ eV a significant decrease occurs in the effective spin-orbit coupling.

3.5.1.4 4 electrons

For four electrons the total magnetic moment is zero in both models: $l_z, s_z = 0$. In the t_{2g}-only model, $l = 1,\ s = 1$ and $J = 0$ as indicated from the $J = -l + s$ law of the T-P equivalence. In the five-orbital model there is

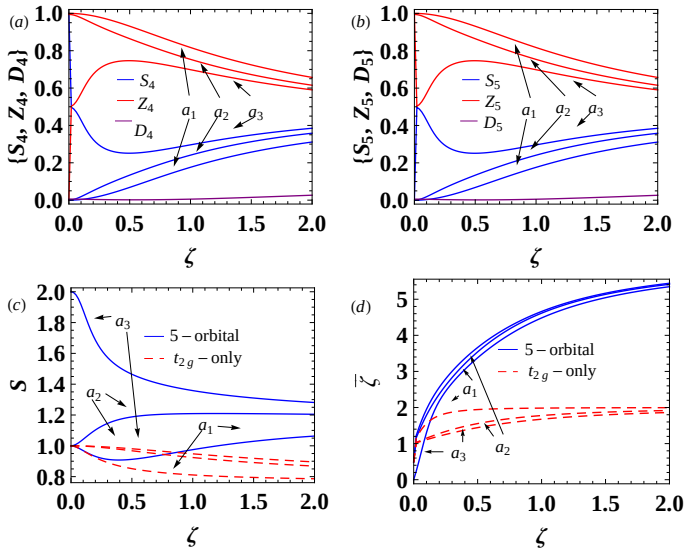

Figure 3.7: Exact diagonalization 4 electron results for crystal field splitting $\Delta = 3eV$. (a) Single S_4, zero Z_4, and double D_4 occupancies of the $d_{3z^2-r^2}$ orbitals. (b) Single S_5, zero Z_5, and double D_5 occupancies of the $d_{x^2-y^2}$ orbitals. (c) Spin quantum number, S. (d) Effective spin-orbit coupling, ζ. Different Hund's coupling parameters $a_1 : J_H = 0.1eV, a_2 : J_H = 0.5eV$, $a_3 : J_H = 0.7eV$.

a low-spin to high-spin transition. For $\Delta = 3$ eV at zero spin-orbit coupling and $J_H = 0.5$ eV, we find $l = 4$, and $s = 1$ (low-spin). While at $J_H = 0.7$ eV there is a transition to a high-spin state with $l = 2$, and $s = 2$. This can be seen in Fig.3.7 (c) and Fig.3.7(a). For $J_H = 0.7$ eV the fourth electron is shared between the e_g-orbitals and the t_{2g}-orbitals in a non-monotonic way as a function of spin-orbit coupling.

In Fig.3.7 (c), for $J_H = 0.1$ eV (low-spin) at $\zeta = 0$, $s = 1$ for both models. However, they start to deviate for $\zeta > 0.5$ eV. For $J_H = 0.5$ eV there is a significant deviation between the two models even at small spin-orbit

coupling. At $J_H = 0.7$ eV there is a high-spin transition, $s = 2$, but there is a rapid reduction of the spin quantum number as a function of spin-orbit coupling, approaching the low-spin value for large ζ.

The effective spin-orbit coupling is seen in Fig.3.7(d). We see that the effect of Hund's coupling is weak within each model, although the models show the strong quantitative differences with respect to each other observed at smaller electron numbers. The single electron approach used in smaller electron fillings gives here $\overline{\zeta}_{t_{2g}}$=2, and $\overline{\zeta}_{t_{2g}-e_g} = 4 \times 3\frac{\zeta}{\zeta/2+\Delta}$, giving for the t_{2g}-only model $\overline{\zeta}_{t_{2g}-only}$=2, and for $\Delta = 3$ eV, and $\zeta = 0.5$ eV, giving for the 5-orbital model $\overline{\zeta}_{5-orbital} = \overline{\zeta}_{t_{2g}} + \overline{\zeta}_{t_{2g}-e_g} = 2+4\times 3\frac{\zeta}{\zeta/2+\Delta} = 3.85$, close to what observed in the figure.

3.5.1.5 5 electrons

At zero spin-orbit coupling with $\Delta = 2.7$ in the five-electron configuration, Fig.3.8(a) shows a low-spin configuration $s = 1/2$ for $J_H = 0.1$ eV and $J_H = 0.5$ eV, and a high-spin $s = 5/2$ configuration for $J_H = 0.6$ eV. Both the high and low-spin configurations evolve continuously as a function of ζ, approaching the same asymptotic value of $s = 1$.

The high-spin to low-spin transition is also seen in the e_g-occupancies, S_i, Z_i, D_i, where i stands for either of the e_g-orbitals, plotted in Fig.3.8(b). For $J_H = 0.6$ eV, at zero spin-orbit coupling each e_g orbital is singly occupied. As the spin-orbit coupling is increased, there is a rapid decrease in the e_g-occupancies, indicating a high-spin to low-spin transition. However, even in

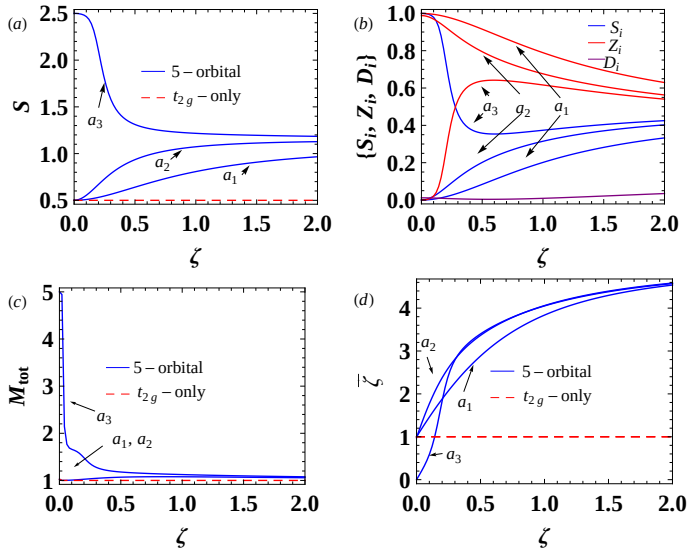

Figure 3.8: Exact diagonalization 5 electron results for crystal field splitting $\Delta = 2.7$ eV. (a) Spin quantum number S. (b) Single S_i, zero Z_i, and double D_i occupancies per e_g-orbital. (c) Total magnetic moment M_{tot}. (d) Effective spin-orbit coupling $\bar{\zeta}$. Different Hund's coupling parameters $a_1 : J_H = 0.1eV, a_2 : J_H = 0.5eV$, $a_3 : J_H = 0.6eV$.

the low-spin case with $J_H = 0.5$ eV and $\zeta = 0.5$ eV (typical values of 5d systems), there is $S_i = 0.2$ single occupancy per e_g orbital, giving a total of 0.4 electrons in the e_g-orbitals and an equivalent depletion from the t_{2g}-orbitals which cannot be captured from the t_{2g}-only model.

Fig.3.8(c) shows the total magnetization which stays very close to 1.0, except for the case of $J_H = 0.6$ eV for very small spin-orbit coupling. The t_{2g}-only model gives $M_{tot} = 1\mu_B$. In the five-orbital model the low-spin state $J_H = 0.5$ eV, $\Delta = 2.7$ eV gives a value very close to that, with slightly reduced l_z and increased s_z. The high-spin configuration $J_H = 0.6$ eV, $\Delta = 2.7$ eV which at $\zeta = 0$ has 5 parallel spins, one in each of the 5-orbitals, starts from

$M_{tot} = 5\mu_B$, but rapidly reduces to $M_{tot} = 1\mu_B$ as the spin-orbit induced high-low spin transition occurs. Thus the state ($J_H = 0.6$ eV, ζ=0.5eV, $\Delta = 2.7$ eV) which has 0.8 electrons in the e_g-orbitals, the state ($J_H = 0.5$ eV, $\zeta = 0.5$ eV $\Delta = 2.7$ eV) which has 0.4 electrons in the e_g-orbitals, and the t_{2g}-only state all share the same total magnetic moment $M_{tot} = 1\mu_B$. Therefore in this example, the magnetic moment is not a good quantity to distinguish between them.

In Fig.3.8(d) we see the effective spin-orbit coupling $\overline{\zeta}$. The t_{2g}-only model, for which $J_{\text{eff}} = 1/2$, gives a contribution of $\overline{\zeta}_{t_{2g}}$=1. However in Ref.[[24]], experiments using X-ray absorption spectroscopy in iridium-based compounds in oxygen octahedral fields ($J_H = 0.5\ eV,\ \Delta = \ 3eV,\ \zeta = 0.5$ eV), a branching ratio BR=6.9 was reported. This gives an effective spin-orbit coupling $\overline{\zeta} = 3.1$, which is what we find as well within the five-orbital model.

The authors of Ref.[24] emphasize that they find large branching ratios in all Ir compounds studied, with little or no dependence on chemical composition, crystal structure, or electronic state and speculate that unusually strong spin-orbit coupling effects maybe a common feature of all the iridates, or at least those possessing an octahedral local crystal field environment. These properties are explained well by our model. First, the effective spin-orbit coupling is a local ion property. Second, an octahedral field environment such as the one studied here shows that the large branching ratio should be a common feature to all the iridates compared.

The authors of Ref.[24] interpret their experimental results as an indica-

tion of a $J_{\text{eff}} = 1/2$ pure state, which has been put forward to explain[54, 53] the insulating properties of Sr_2IrO_4, and Na_2IrO_3. In the $J_{\text{eff}} = 1/2$ scenario, the $J_{\text{eff}} = 3/2$ band derived from the $J = 3/2$ states will be completely occupied, effectively prohibiting any L_2 transitions ($2p_{1/2} \rightarrow 5d_{3/2}$) and only L_3 transitions will be allowed processes ($2p_{3/2} \rightarrow 5d_{3/2,5/2}$), since the $J_{\text{eff}} = 1/2$ is separated from the $J = 5/2$ states (the lowest unoccupied states). Hence $I_{L_2} \approx 0$, explaining the large branching ratio observed. Whereas in the $S_{\text{eff}} = 1/2$ scenario, on the other hand, the lowest unoccupied state possesses mixed $J = 3/2$ and $J = 5/2$ character that allows both L_2 and L_3 transitions, having lower a BR. (Recall the $BR = I_{L_3}/I_{L_2}$.) The authors of Ref.[24] suggested that the difference between the two BR can distinguish between the two scenarios, and reveal the nature of the ground state.

However, in the first case the e_g states have been assumed to be infinitely separated from the t_{2g} ones, which gives pure $J_{\text{eff}} = 3/2$ and $J_{\text{eff}} = 1/2$ but as we see in Fig.3.3 going beyond the T-P equivalence from the strong spin-orbit coupling side, the octahedral crystal field mixes $J = 3/2$ and $J = 5/2$, which are not mixed at zero octahedral crystal field.

The reported tetragonal distortions of the octahedral oxygen cages mixes $J_{\text{eff}} = 1/2$ and $J_{\text{eff}} = 3/2$ and takes one away from the pure $J_{\text{eff}} = 1/2$ scenario. We show in this work that even at large crystal fields of $\Delta = 3$ eV, the mixing between t_{2g} and e_g manifolds is not negligible. Accounting for it can explain the remarkably large BR in a more natural, and more general way, for all the Ir-compounds in an octahedral field. Foyevtsova *et al.*,[29]

study Na_2IrO_3 using DFT calculations with and without spin-orbit coupling. To compare the results of their proposed molecular orbital scenario with experiments, they report $\overline{\zeta} = 1.91$ by including the e_g orbitals and $\overline{\zeta} = 0.73$ by keeping only the t_{2g} in their calculations, supporting a non-pure $J_{\text{eff}} = 1/2$ state. Others have reached similar conclusions regarding the admixture of e_g orbitals.[66, 18, 104]

Measurements of XAS on $BaIrO_3$,[61] report a BR=4, which gives a $\overline{\zeta} = 2.1$–double the canonical value for the $J_{\text{eff}} = 1/2$ state that gives $\overline{\zeta} = 1$–and they attribute the larger value to the mixing with the e_g states. Katukuri *et al.*[47, 49] using quantum chemistry calculations for several iridate oxides report $\overline{\zeta} \approx 2$ where they considered hybridization between e_g orbitals and neighboring oxygen ligands, which reduces the value of $\overline{\zeta}$. In addition, they report that such large deviations from the canonical value of $\overline{\zeta} = 1$ of the t_{2g}-only model of $J_{\text{eff}} = 1/2$ cannot be accounted for without the mixing with the e_g states. In Ref. [35] XAS measurements for Sr_2IrO_4 report a BR=4.1 which gives $\overline{\zeta} = 2.1$ and the deviation from $\overline{\zeta} = 1$ is attributed to the mixing of t_{2g} and e_g states. In Ref. [15] x-ray resonant magnetic scattering (XRMS) measurements on $BaIrO_3$ gives a BR=5.45, which gives $\overline{\zeta} = 2.67$.

Closing this discussion of the effective spin-orbit coupling in the literature, and coming back to our calculations, a single particle analysis captures well the observed trend, giving $\overline{\zeta}_{5-orbital} = 1 + 4 \times 3\frac{\zeta}{\zeta/2+\Delta} = 3.03$ for $\zeta = 0.5$ eV and $\Delta = 2.7$ eV. In Fig.3.8(d) in the vicinity of $\zeta = 0.5$ the effect of Hund's coupling is to increase the effective spin-orbit coupling. Also, for $J_H = 0.6$ eV,

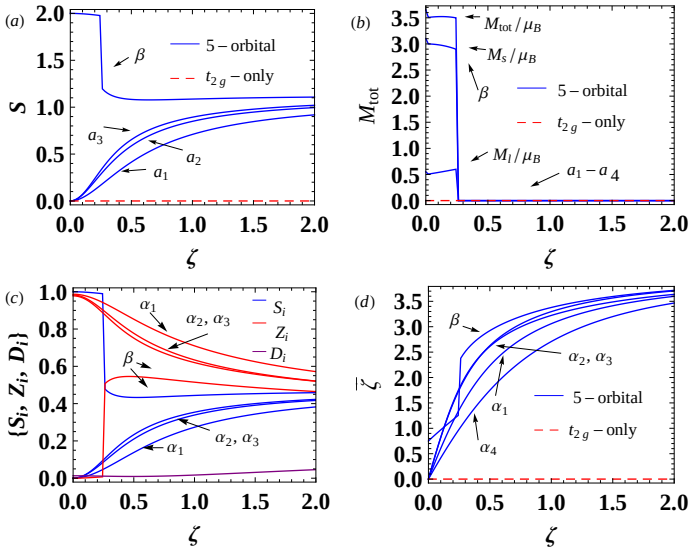

Figure 3.9: Exact diagonalization 6 electron results. (a) Spin quantum number S. (b) Total magnetic moment M_{tot}). (c) Single S_i, zero Z_i, and double D_i occupancy per e_g orbital. (d) Effective spin-orbit coupling $\overline{\zeta}$. Parameters for predominately low-spin configurations: $a_1 : \Delta = 3eV, J_H = 0.5eV, a_2 : \Delta = 2.5eV, J_H = 0.5eV, a_3 : \Delta = 3eV, J_H = 0.7eV, a_4 : \Delta = 3eV, J_H = 0.1eV$. Parameters for predominately high spin-configurations $\beta : \Delta = 2.5eV, J_H = 0.7eV$.

$\overline{\zeta}$ starts from zero because in this high-spin configuration $l = 0$ and $s = 5/2$ for $\zeta = 0$.

3.5.1.6 6 electrons

The six-electron results are shown in Fig.3.9. For the t_{2g}-only model the results are trivial: The spin, total magnetic moment, effective spin-orbital coupling are all zero, since we have 6 electrons completely occupying all the t_{2g} orbitals. However, adding two more orbitals changes the picture. As we see from Fig.3.9 (a), the spin quantum number at zero spin-orbit coupling

is $S = 0$, but for finite spin-orbit coupling it deviates from that, reaching $S \approx 0.5$ around $\zeta = 0.5eV$ for the configurations that have $S = 0$ at $\zeta = 0$. The low-spin configurations have completely filled t_{2g} orbitals at $\zeta = 0$. These configurations are $a_1 : \Delta = 3eV, J_H = 0.5eV, a_2 : \Delta = 2.5eV, J_H = 0.5eV, a_3 : \Delta = 3eV, J_H = 0.7eV, a_4 : \Delta = 3eV, J_H = 0.1eV$.

Comparing these cases, one sees that when the ratio J_H/Δ is increased the spin quantum number increases with increasing spin-orbit coupling. If we continue increasing this ratio to the configuration $\beta : \Delta = 2.5eV, J_H = 0.7eV$, the system will transition to a high-spin state at zero spin-orbit coupling. However, for the high-spin configuration β, at $\zeta = 0.25eV$ spin-orbit coupling creates a high-spin to intermediate-spin transition, going from $S = 2$ to approximately $S = 1$.

Turning our attention now to Fig.3.9(b), we see that only the high-spin β configuration has a net magnetic moment, while all other configurations give a zero total magnetic moment. The total magnetic moment of the β high-spin configuration is M_{tot}/μ_B=3.5, where M_S/μ_B=3 and M_l/μ_B=0.5. But at $\zeta = 0.25eV$ where the spin-orbit coupling induces the high-spin to intermediate-spin transition, the magnetic moment vanishes. The transition is also reflected in the single and zero occupancies per e_g-orbital, shown in Fig.3.9(c). For the β configuration and $\zeta < 0.25$ there are 2 electrons, 1 per e_g-orbital, while for $\zeta > 0.25$ there is 1 electron, 1/2 per e_g-orbital. Also, for the low-spin configurations a_1-a_3 there are 0.4 electrons in the e_g orbitals, 0.2 to each orbital.

The effective spin-orbit coupling is shown in Fig. 3.9 (d). The effect of the Hund's coupling is to increase $\overline{\zeta}$ in the intermediate spin-orbit coupling region. The spin-orbit induced transition from high-spin to intermediate-spin of the β configuration, by a jump at $\zeta = 0.25eV$, doubles its value from $\overline{\zeta} = 1.2$ to $\overline{\zeta} = 2.4$. The single particle perturbative description gives $\overline{\zeta} = 4 \times 3\frac{\zeta}{\zeta/2+\Delta}$, and as it is expected to work well at small correlation, it is compared to $J_H = 0.1eV$, and for $\zeta = 0.5eV$ and $\Delta = 3eV$ gives a value of $\overline{\zeta} = 1.83$, where the exact result gives $\overline{\zeta} = 1.81$.

3.5.2 Comparison of t_{2g}-e_g model with e_g only model

For filling from seven to nine electrons, we will compare the results of the full t_{2g}-e_g model with e_g-only model. The matrix elements of orbital angular momentum are completely quenched in the e_g-only model, and thus the spin-orbit coupling as well.

3.5.2.1 7 electrons

For the seven-electron configuration, we have for the e_g-only model a single electron in the e_g-orbital, which gives $S = 1/2$ as seen in Fig.3.10(a). At zero spin-orbit coupling for the configurations $\alpha_1 : \Delta = 2.5eV, J_H = 0.5eV$ and $\alpha_2 : \Delta = 2.5eV, J_H = 0.5eV$, $S = 1/2$ there is a single electron in the $d_{3z^2-r^2}$ orbital and the rest completely occupy the t_{2g} orbitals, as seen from Fig.3.10(c), (d). As a function of the spin-orbit coupling, there is a depletion of the t_{2g} orbitals, and an increase in the single occupancy of the $d_{x^2-y^2}$ orbital

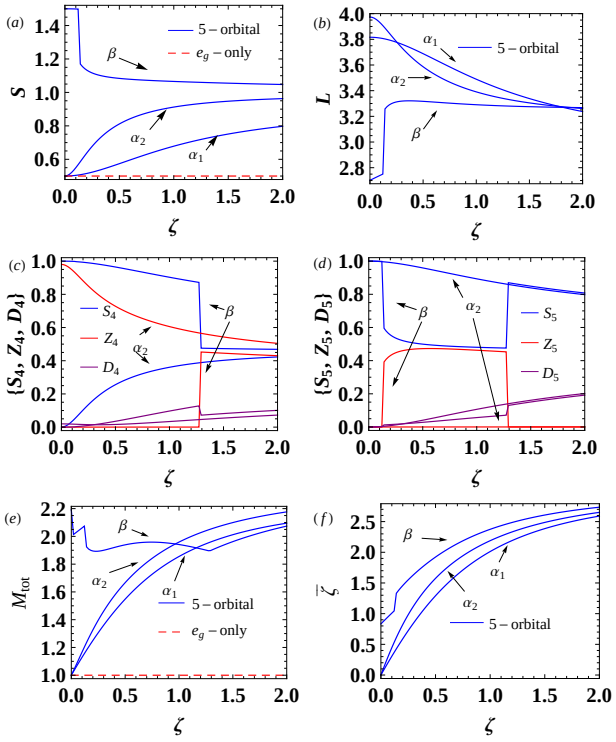

Figure 3.10: Exact diagonalization 7 electron results. (a) Spin quantum number S. (b) Angular momentum quantum number L. (c) Single, double, zero occupancies of the $d_{3z^2-r^2}$ orbital (S_4, D_4, Z_4). (d) Single, double, zero occupancies of the $d_{x^2-y^2}$ orbital (S_5, D_5). (e) Total magnetic moment M_{tot}. (f) Effective spin-orbit coupling $\overline{\zeta}$ for $\alpha_1 : \Delta = 3eV, J_H = 0.1eV$, $\alpha_2 : \Delta = 2.5eV, J_H = 0.5eV$, $\beta : \Delta = 2.5eV, J_H = 0.7eV$ configurations.

as seen in Fig.3.10(d). This causes an analogous increase in the spin quantum number, as seen in Fig.3.10 (a). When one increases Hund's coupling at zero spin-orbit coupling, there is a low-spin to high-spin transition. In Fig. 3.10(a) the configurations $\alpha_1 : \Delta = 3eV, J_H = 0.1eV$ and $\alpha_2 : \Delta = 2.5eV, J_H = 0.5eV$ give $S = 1/2$. When the Hund's coupling is increased in the configuration $\beta : \Delta = 2.5eV, J_H = 0.5eV$, we get $S = 3/2$ giving two electrons in the e_g-

orbitals and leaving one hole in the t_{2g} orbitals. This is shown in Fig.3.10 (c), (d) for the e_g-occupancies. At spin-orbit coupling $\zeta = 0.12$ the high-spin β configuration undergoes an intermediate-spin transition from $S = 3/2$ to $S \approx 1.1$ and a subsequent depletion of the $d_{x^2-y^2}$ orbital from 1 electron to 0.5 electron, giving a total 1.5 electrons in the e_g-orbitals. At spin-orbit coupling $\zeta = 1.3$ eV there is a second transition, interchanging the occupancies between the two e_g orbitals, while keeping the total occupancy of 1.5 electrons in the e_g orbitals constant. In Fig.3.10(b) we see the total angular momentum in $\alpha_1, \alpha_2, \beta$ configurations capturing these transitions as well.

In Fig.3.10(e) the total magnetic moment is shown. For the configurations α_1, α_2 there is a significant deviation from the e_g-only model in which the orbital angular momentum is completely quenched. The total moment is only spin. In the five-orbital model $M_{tot} \approx 1.5\mu_B$ for $\zeta = 0.5$, with the difference coming from the orbital magnetic moment M_l, since the spin magnetic moment has small deviation from $M_S \approx 1\mu_B$ as a function of spin-orbit coupling. For the β configuration there are two transitions as a function of spin-orbit coupling, which are seen as discontinuities in the M_{tot} Fig.3.10(e).

The effective spin-orbit coupling is shown in Fig.3.10(f) for three characteristic cases of the low-spin configurations $\alpha_1(\Delta = 3eV, J_H = 0.1eV)$, $\alpha_2(\Delta = 2.5eV, J_H = 0.5eV)$ spin, and the high-spin $\beta(\Delta = 2.5eV, J_H = 0.7eV)$ configuration. The single-electron perturbation result gives $\overline{\zeta} = \frac{3}{4}\frac{\zeta^2}{(\zeta/2+\Delta)^2} + 3\times 3\frac{\zeta}{\zeta/2+\Delta}$ which is close to what is observed in the α_1 configuration. Note that the e_g-only model gives $\overline{\zeta} = 0$, so in 4d and 5d systems with a d^7 configuration,

a finite effective spin-orbit coupling can be measured.

3.5.2.2 8 electrons

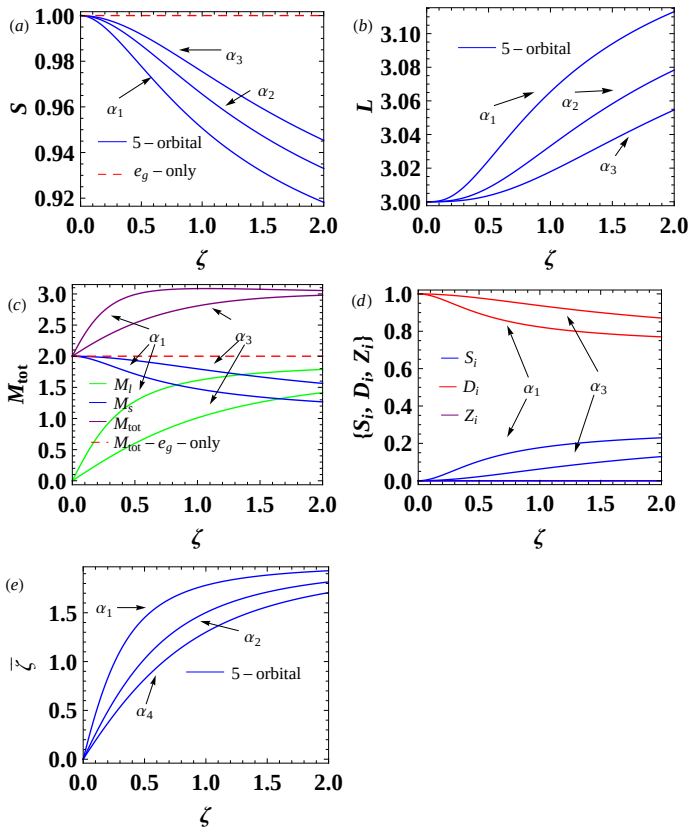

Figure 3.11: Exact diagonalization 8 electron results. (a) Spin quantum number S. (b) Angular momentum quantum number L. (c) Total magnetic moment M_{tot}, orbital magnetic moment M_l, and spin magnetic moment M_S. (d) Single S_i, double D_i, and zero occupancies Z_i per t_{2g}-orbital. (e) Effective spin-orbit coupling $(\bar{\zeta})$ for $\alpha_1 : \Delta = 1eV, J_H = 0.5eV$, $\alpha_2 : \Delta = 2eV, J_H = 0.5eV$, $\alpha_3 : \Delta = 3eV, J_H = 0.5eV$, $\alpha_4 : \Delta = 3eV, J_H = 0.1eV$ configurations.

For eight electrons, we naively expect two electrons in the e_g orbitals and the rest are in the completely filled t_{2g} shell. In Fig.3.11(a),(b) we see the

spin S, and orbital angular momentum L quantum numbers, for three different values of the crystal fields, $\alpha_1 : \Delta = 1eV, \alpha_2 : \Delta = 2eV, \alpha_3 : \Delta = 3eV$, all at $J_H = 0.5eV$. The deviation from $S = 1$, and $L = 3$ is small as a function of spin-orbit coupling. In Fig.3.11(c) the total magnetic moment M_{tot}, the orbital magnetic moment M_l, and the spin magnetic moment M_S are plotted, for α_1 and α_3 configurations. At zero spin-orbit coupling, the orbital angular momentum is completely quenched, as predicted from the e_g-only model. However, spin-orbit coupling gives rise to a significant amount of orbital angular momentum; the smaller the crystal field (α_1), the greater the restoration compared to the larger crystal field configuration α_3. Spin-orbit coupling causes a small reduction in the spin magnetic moment, and as a result the difference in the total magnetic moment between the five-orbital model and the e_g-only model is mainly from the orbital magnetic moment M_l. In Fig.3.11(d) the single S_i, double D_i, and zero Z_i occupancies per t_{2g}-orbital are plotted. The main effect is that there is depletion of the t_{2g} orbitals as a function of the spin-orbit coupling, with a greater effect for smaller crystal fields.

In Fig.3.11(e), the effective spin-orbit coupling is plotted. The smaller the crystal field, the less the quenching of the orbital angular moment. Consequently, the effective spin-orbit coupling is larger. The single particle perturbative description gives $\overline{\zeta} = \frac{3}{2}\frac{\zeta^2}{(\zeta/2+\Delta)^2} + 2 \times 3\frac{\zeta}{\zeta/2+\Delta}$, which compared to the least interacting $\alpha_4 : \Delta = 3eV, J_H = 0.1eV$ configuration gives a good qualitative description, of $\overline{\zeta} \approx 0.9$ for $\Delta = 3$ eV and $\zeta = 0.5$ eV.

3.5.2.3 9 electrons

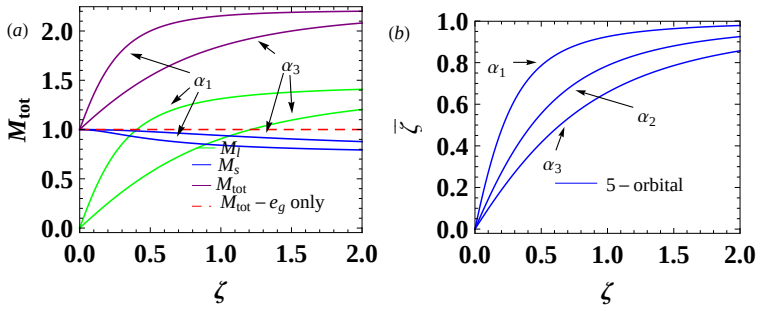

Figure 3.12: Exact diagonalization 9 electron results. (a) Total magnetic moment M_{tot}, orbital magnetic moment M_l, and spin magnetic moment M_S. (b) Effective spin-orbit coupling ($\bar{\zeta}$) for $\alpha_1 : \Delta = 1eV$, $\alpha_2 : \Delta = 2eV$, $\alpha_3 : \Delta = 3eV$ configurations.

For the case of nine electrons one has $S = 1/2$ and $L = 2$. The angular momentum at $\zeta = 0$ is completely quenched giving a total magnetic moment $M_{tot} = 1\mu_B$. Spin-orbit coupling gives rise to finite orbital angular momentum. For $\Delta = 1$ eV and $\zeta = 0.5$ eV one has an extra contribution $M_l = 1\mu_B$, and at $\Delta = 3$ eV and $\zeta = 0.5$ eV one has an extra contribution of $M_l = 0.5\mu_B$, as seen in Fig.3.12(a). The spin magnetic moment M_S is only weakly affected by spin-orbit coupling and remains very close to $M_S = 1\mu_B$. The effective spin-orbit coupling is shown in Fig.3.12(b) for different values of crystal field, $\alpha_1 : \Delta = 1eV, \alpha_1 : \Delta = 2eV, \alpha_3 : \Delta = 3eV$. As the crystal field strength increases, the orbital angular momentum and the effective spin-orbit coupling $\bar{\zeta}$ decreases. The single electron perturbation result gives $\bar{\zeta} = 3 \times \frac{3}{4} \frac{\zeta^2}{(\zeta/2+\Delta)^2} + 3\frac{\zeta}{\zeta/2+\Delta}$, giving for $\Delta = 3eV, \zeta = 0.5eV$ $\bar{\zeta} = 0.51$, capturing what we see in Fig. 3.12 (b) in $\alpha_3 : \Delta = 3eV$. Also there is some small depletion of t_{2g}-occupancy due to

the $t_{2g} - e_g$ mixing of the off diagonal elements of the spin-orbit coupling interaction.

Chapter 4

Summary and future work

In summary, in chapter 2 we studied the thermal conductivity of electrically insulating local moment models with strong spin-orbit coupling. As a specific example, we studied the nearest-neighbor Heisenberg-Kitaev model on the honeycomb lattice, whose ground state properties (magnetic orders) are well established. In particular, for different model parameters, Néel, stripy, zig-zag, and ferromagnetic phases are realized. The richness of the phase diagram originates in the spin-orbit coupling. For these four magnetic phases, the magnon spectra were initially computed within the linear spin wave approximation. Then, using Fermi's Golden rule in conjunction with the magnon and the phonon spectra, the scattering rates for the lowest order magnon-phonon scattering processes, the two-magnon one-phonon processes, were calculated. Finally, the kinetic Boltzmann equation within the relaxation time approximation was employed for the calculation of the magnonic and the phononic thermal conductivities. The evaluation of the scattering rates was among the most technically challenging aspects of this work, and we had to innovate in order to find an efficient method of computing these rates for the multiple magnon branches. The procedure we followed and described in this work can be generalized to any two-dimensional magnon-phonon system.

Several results and qualitative conclusions for the magnon dominated and the phonon dominated heat transport are contained in Sec.2.4. We emphasize again that each of the previous regimes is further broken down into three main transport subregimes: the ballistic, the diffusive, and the intermediate subregime. We have also included some discussion of how to estimate which regime may be most relevant to a particular material of a given size. A central result of this analysis is that the effect of the strong spin orbit coupling on the magnetic degrees of freedom, which is to induce anisotropies in the band structures of the low energy magnetic excitations, can most efficiently be probed by measuring the ballistic thermal conductivity of a material whose heat transport is magnon dominated.

When the phonon energy dominates the magnon energy, the thermal conductivity primarily reflects the spatially isotropic phonon band structure. In this case, the the thermal conductivity tensor remains isotropic, and in the ballistic subregime, at low temperatures, follows a quadratic temperature power law (reminiscent of the 2D Debye model). On the other side, when the magnon energy dominates the phonon energy, the thermal conductivity tensor of the various phases shows significant anisotropic behavior that is strongest within the ballistic subregime. In addition to this, the thermal conductivity of different magnetic phases are found to follow different temperature dependences, even at very low temperatures.

By carefully analyzing the low temperature dependence and the degree of anisotropy of the thermal conductivity tensor, one may be able to use

thermal transport to infer important features of the magnetic order and excitation spectrum that are not easily obtained by other means. For example, the large neutron absorption cross-section of iridium makes measurements of the magnon spectrum even in bulk iridates difficult. The small signal from resonant inelastic X-ray scattering in a two-dimensional system also makes determination of magnetic order and excitations challenging. Thus, thermal transport may offer a window into the magnetic degrees of freedom where other methods present challenges. On the experimental side, measurements of the thermal conductivity of the SOC-induced Mott insulator Sr_2IrO_4 were recently reported [94], which by comparison with the thermal conductivity of the La_2CuO_4 antiferromagnet, led to the conclusion that the thermal conductivity of the former is highly suppressed due to strong magnon-phonon coupling, and this effect was then correlated with strong spin-orbit coupling of the iridate.

We hope this work will help stimulate future theoretical and experimental work on thermal transport in insulating local moment systems with strong-spin orbit coupling, since the methodology followed in this work opens a new window to study systems which previously were technically unapproachable. Particularly, magnetically insulating systems that cannot be approached analytically as far as the magnon-phonon interaction problem is concerned, can be numerically approached by the above methodology which relies on the use of a general numerical Bogoliubov transformation for the derivation of the magnon-phonon interaction Hamiltonian and the calculation of magnon-phonon transport relaxation times, even in the presence of anisotropic magnon

bands. These anisotropies are commonplace within the newly discovered field of magnonics, as well as among materials with strong-spin orbit coupling. Such materials may be relevant to applications in spin caloritronics and other spin-based energy, computing, and communications applications. Finally, we note that theoretical estimates of the magnon-phonon relaxation times, that are possible within the above methodology, could be useful to experimentalists who want to know (approximately) the strength of the magnon-phonon relaxation time in their specific systems of study (to the extent that the heat transport is dominated by the mechanisms studied in this work).

In chapter 3, we have carried out an exact diagonalization study of interacting d-orbital electrons in a cubic crystal field environment for all electron fillings. We have focused on mixing effects of the t_{2g} and e_g orbitals induced by the spin-orbit coupling and compared our results to the t_{2g}-only and e_g-only models commonly used in the literature. For realistic interaction parameters in Eq.(3.20), crystal field splitting and spin-orbit coupling Eq.(3.14), we find the mixing effects can be significant. These mixing effects can be important in the interpretation of the branching ratio measured in spectroscopic measurements, which is often used to determine the effective strength of the spin-orbit coupling. If one assumes a t_{2g}-only model (neglecting t_{2g} and e_g mixing) for iridates, for example, one would infer an effective spin-orbit coupling value smaller than the one for the full t_{2g}-e_g model.

For the various electron fillings we calculated the spin S, orbital angular momentum L, total magnetic moment $M_{\rm tot}$, the single S_i, zero Z_i, and double

D_i occupancy of the i^{th} orbital, and the effective spin-orbit coupling strength $\bar{\zeta}$. In general, these quantities can show a complex evolution with the strength of the crystal field splitting Δ and the bare spin-orbit coupling strength ζ. For certain electron fillings, crystal field splittings Δ and Hund's coupling J_H, we observe high-spin to low-spin transitions as a function of ζ. An intermediate spin state may also be realized. The most important results are summarized in Figs.3.4-3.12.

The results we have obtained here should be useful in helping to derive more realistic models of local moment interactions in the 4d and 5d transition metal oxides. These local moment models could then be used to predict what type of magnetic phases and magnetic excitations might be expected in the heavy transition metal oxides. Our local moment results could also be used as a starting point for non-equilibrium (Floquet) studies as well since they include an enlarged Hilbert space and can better capture the response of a periodic drive. These are directions for future research.

Appendices

Appendix A

Linear spin wave dispersion relations and one phonon-two magnon scattering amplitudes for the nn Heisenberg-Kitaev Hamiltonian

In this appendix, we sketch out the derivation of the linear spin wave dispersion relations and the lowest order magnon-phonon scattering amplitudes for the four collinear ordered phases of the Heisenberg-Kitaev model, depending on the relative strength of the Heisenberg and Kitaev couplings through the angle φ (see Fig. 2.2 and Eq.(2.2)). The spin wave analysis of the zig-zag and the stripy state requires the use of four magnetic sublattices, labelled as A, B, C, D, and the magnetic unit cell is the rectangular unit cell (gray-shaded rectangle defined by the translation vectors $\boldsymbol{a}$ and $\boldsymbol{b}$) shown in Fig.A.1. The Néel and the ferromagnetic states require only two magnetic sublattices, and the magnetic unit cell coincides with the chemical unit cell of the honeycomb lattice (see the dashed parallelogram whose edges are defined by the translation vectors $\boldsymbol{t_1}$ and $\boldsymbol{t_2}$ in Fig.A.1). Notice that in all the following analysis the spatial gradients of the Heisenberg and the Kitaev exchange couplings are denoted as $\vec{J}^{(1)}$ and $\vec{K}^{(1)}$ respectively.

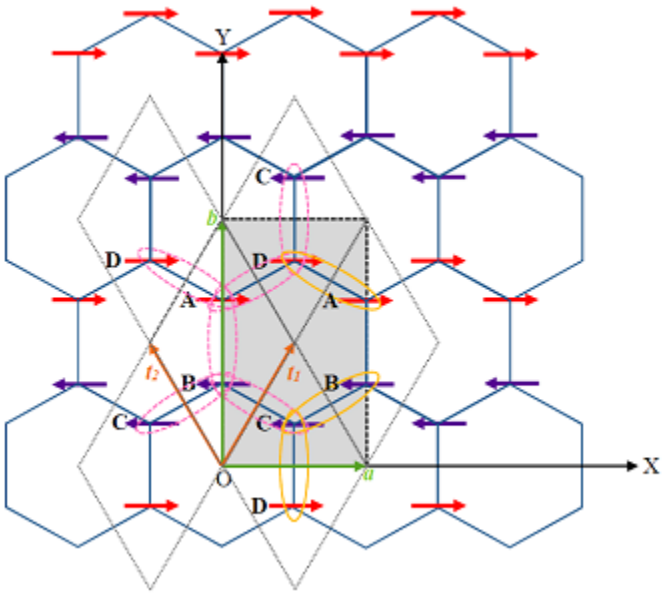

Figure A.1: Zig-zag magnetic phase: A magnetic unit cell consists of four magnetic moments labelled as A, B, C and D, and is represented by the gray-shaded rectangle shown in the figure. The translation vectors of the periodic magnetic structure are the vectors $\boldsymbol{a}$ and $\boldsymbol{b}$. The translation vectors of the chemical periodic structure are the vectors $\boldsymbol{t_1}$ and $\boldsymbol{t_2}$, and a chemical unit cell is represented by any dashed parallelogram. For the Néel and the ferromagnetic states the magnetic unit cell coincides with the chemical unit cell (that is common to all phases).

A.1 Zig-zag phase

As already noted, for the zig-zag phase the magnetic unit cell is defined by the gray-shaded rectangle with sides of length a (along the global X-axis) and b (along the global Y-axis), and consists of four magnetic moments A, B, C and D, with A and D pointing along the positive X-axis, and B and C pointing along the negative X-axis. Choosing the positive spin quantization axis along the negative X-axis, at the sites A and D we employ the bosonization given by

the Eqs.(2.17)-(2.19), while at the sites B and C we employ the bosonization given by the Eqs.(2.14)-(2.16). Each magnetic site has three nearest neighbors (nn) shown as encircled bonds in Fig.A.1. To avoid double counting of the nn interactions, only *the dashed pink encircled bonds* (see Fig.A.1) are taken into account. The Kitaev term couples the z-spin components along the AB and the CD bond, the x-spin components along the upper right AD and the lower left BC bond, and the y-spin components along the upper left AD and the lower right BC bond. Using the representation of the x- and y-spin components in terms of the ladder spin operators to write the total Hamiltonian in terms of the $S_i^{||}$, S_i^+ and S_i^- operators, performing the bosonization as elaborated above, and Fourier transforming according to the convention of Eqs.(2.20) and (2.21), ones finds the classical ground state energy $\mathcal{H}_{classical} = \frac{NS^2}{2}(J - 2K)$, and the following *spin wave mode matrix* $M(\boldsymbol{k})$ (reference to Eq.(2.22) and the notation thereof):

$$M(\boldsymbol{k}) = \begin{bmatrix} A & 0 & 0 & D(\boldsymbol{k}) & 0 & B(\boldsymbol{k}) & 0 & C(\boldsymbol{k}) \\ 0 & A & D^*(\boldsymbol{k}) & 0 & B^*(\boldsymbol{k}) & 0 & C^*(\boldsymbol{k}) & 0 \\ 0 & D(\boldsymbol{k}) & A & 0 & 0 & C(\boldsymbol{k}) & 0 & B(\boldsymbol{k}) \\ D^*(\boldsymbol{k}) & 0 & 0 & A & C^*(\boldsymbol{k}) & 0 & B^*(\boldsymbol{k}) & 0 \\ 0 & B(\boldsymbol{k}) & 0 & C(\boldsymbol{k}) & A & 0 & 0 & D(\boldsymbol{k}) \\ B^*(\boldsymbol{k}) & 0 & C^*(\boldsymbol{k}) & 0 & 0 & A & D^*(\boldsymbol{k}) & 0 \\ 0 & C(\boldsymbol{k}) & 0 & B(\boldsymbol{k}) & 0 & D(\boldsymbol{k}) & A & 0 \\ C^*(\boldsymbol{k}) & 0 & B^*(\boldsymbol{k}) & 0 & D^*(\boldsymbol{k}) & 0 & 0 & A \end{bmatrix}, \tag{A.1}$$

where we defined the following parameters (in this appendix the parameter A appearing in the spin wave mode matrix M should never be confused with the magnetic energy scale defined in Eq.(2.2))

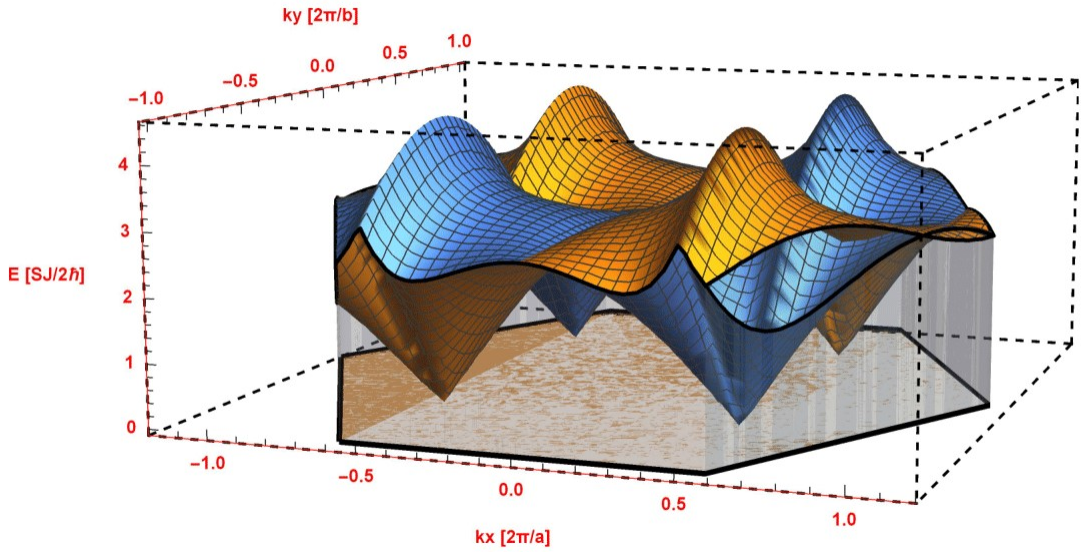

Figure A.2: Lower spin wave dispersion relations of the zigzag phase, as given by Eqs.(A.2). The yellow surface corresponds to $\omega_1(\boldsymbol{k})$ and the blue surface to $\omega_2(\boldsymbol{k})$. Notice that the magnon wavevector components k_x and k_y are measured in units of $\frac{2\pi}{a}$ and $\frac{2\pi}{b}$ respectively and the spin wave energy is measured in units of $\frac{SJ}{2\hbar}$. The shaded hexagon within the Oxy plane is the first Brillouin zone (1BZ) of the honeycomb lattice. The plot is for $K/J = -2.65$ and $\alpha = 2\pi/3$.

$$
\begin{aligned}
A &= J(\vec{\delta}_1) - J(\vec{\delta}_2) - J(\vec{\delta}_3) + 2K(\vec{\delta}_1) = -J + 2K, \\
B(\boldsymbol{k}) &= J(\vec{\delta}_1)e^{-i\vec{k}\cdot\vec{\delta}_1} = J\eta^{-2}, \\
C(\boldsymbol{k}) &= K(\vec{\delta}_3)e^{-i\vec{k}\cdot\vec{\delta}_3} - K(\vec{\delta}_2)e^{-i\vec{k}\cdot\vec{\delta}_2} = 2iK\eta\sin(\pi h), \\
D(\boldsymbol{k}) &= \left(J(\vec{\delta}_3) + K(\vec{\delta}_3)\right)e^{-i\vec{k}\cdot\vec{\delta}_3} \\
&+ \left(J(\vec{\delta}_2), +K(\vec{\delta}_2)\right)e^{-i\vec{k}\cdot\vec{\delta}_2} = 2(J+K)\eta\cos(\pi h),
\end{aligned}
$$

in combination with the following definitions

$$
\begin{aligned}
&a = \alpha\sqrt{3}, \quad \alpha = \text{hexagon side } = \text{interionic distance},\\
&\vec{\delta}_1 = \frac{1}{3}\boldsymbol{b} = \frac{1}{3}b\hat{\boldsymbol{e}}_Y, \quad b = 3\alpha\\
&\vec{\delta}_2 = \frac{1}{2}\boldsymbol{a} - \frac{1}{6}\boldsymbol{b} = \frac{1}{2}a\hat{\boldsymbol{e}}_X - \frac{1}{6}b\hat{\boldsymbol{e}}_Y,\\
&\vec{\delta}_3 = -\frac{1}{2}\boldsymbol{a} - \frac{1}{6}\boldsymbol{b} = -\frac{1}{2}a\hat{\boldsymbol{e}}_X - \frac{1}{6}b\hat{\boldsymbol{e}}_Y,\\
&\boldsymbol{k} = \left(h\frac{2\pi}{a},\ k\frac{2\pi}{b}\right) = h\frac{2\pi}{a}\hat{\boldsymbol{e}}_X + k\frac{2\pi}{b}\hat{\boldsymbol{e}}_Y, \quad h,k \in \mathbb{Z}\\
&\zeta = e^{i\pi h} = \zeta^{-1} \quad (\zeta^2 = 1 = \zeta\zeta^{-1}), \quad \eta = e^{ik\pi/3},\\
&\boldsymbol{t_1} = \frac{1}{2}(\boldsymbol{a} + \boldsymbol{b}), \quad \boldsymbol{t_2} = \frac{1}{2}(\boldsymbol{b} - \boldsymbol{a}),
\end{aligned}
$$

where it is more convenient to measure the components of the magnon wavevector $\boldsymbol{k}$ in units of the reciprocal lattice of the magnetic lattice, i.e. in units of $\frac{2\pi}{a}$ and $\frac{2\pi}{b}$ respectively. As far as the parameters A, $B(\boldsymbol{k})$, $C(\boldsymbol{k})$ and $D(\boldsymbol{k})$ are concerned, it was assumed that the exchange couplings J and K are bond independent (i.e. the same for each nn bond), as a result of which the bond direction dependence was then dropped.

Diagonalizing the dynamical matrix $D = I_- M$ as described in Eq.(2.27) of Sec.2.2, we obtain the following *magnon normal modes*:

$$\omega_1 = \sqrt{\Omega_3 - \sqrt{\Omega_4}}, \quad \omega_2 = \sqrt{\Omega_1 - \sqrt{\Omega_2}}, \tag{A.2}$$

$$\omega_3 = \sqrt{\Omega_3 + \sqrt{\Omega_4}}, \quad \omega_4 = \sqrt{\Omega_1 + \sqrt{\Omega_2}}, \tag{A.3}$$

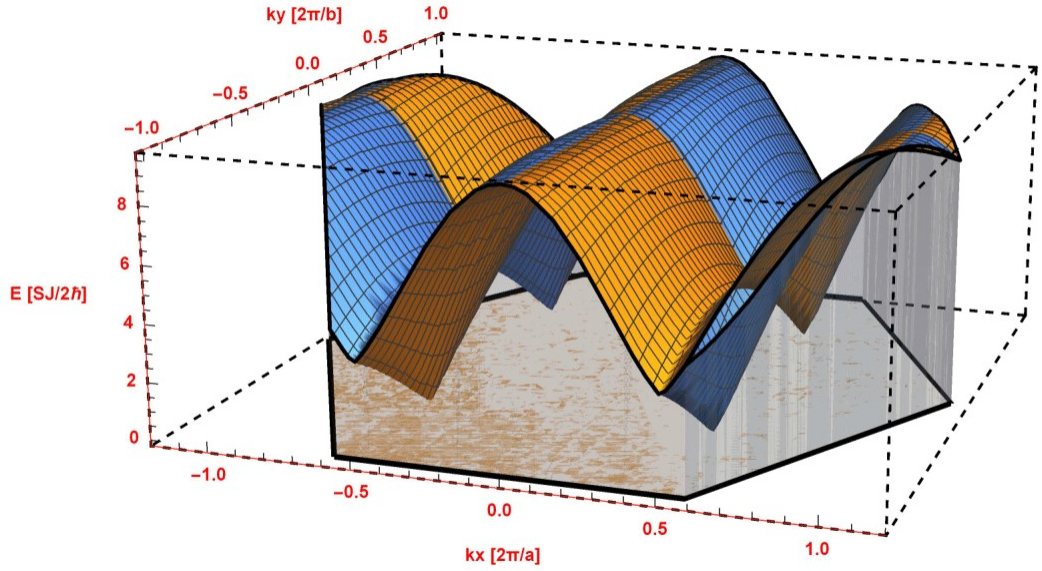

Figure A.3: Upper spin wave dispersion relations of the zigzag phase, as given by Eqs.(A.3). The yellow surface corresponds to $\omega_3(\boldsymbol{k})$ and the blue surface to $\omega_4(\boldsymbol{k})$. Notice that the magnon wavevector components k_x and k_y are measured in units of $\frac{2\pi}{a}$ and $\frac{2\pi}{b}$ respectively and the spin wave energy is measured in units of $\frac{SJ}{2\hbar}$. The shaded hexagon within the Oxy plane is the 1BZ of the honeycomb lattice. The plot is for $K/J = -2.65$ and $\alpha = 2\pi/3$.

where the following parameters were used

$$\Omega_1 = A^2 + |D|^2 - |B - C|^2,$$

$$\Omega_2 = 4A^2|D|^2 - |D(B^* - C^*) - D^*(B - C)|^2,$$

$$\Omega_3 = A^2 + |D|^2 - |B + C|^2,$$

$$\Omega_4 = 4A^2|D|^2 - |D(B^* + C^*) - D^*(B + C)|^2.$$

The spin wave dispersions of Eq.(A.2) are plotted in Fig.A.2 and those of Eq.(A.3) are plotted in Fig.A.3. At low enough temperatures, as far as the magnon-phonon interaction is concerned, only the parts of the spin wave spec-

tra around the *spin wave valleys* are of interest, whose exact $\boldsymbol{k}$-space positions are found from the conditions that $\omega_i = 0$, $i = 1, 2, 3, 4$. From Eqs.(A.2) and (A.3) it is not hard to see that $\omega_i = 0$ implies that either the whole argument of the big (outer) square root is zero, or all the Ω_j parameters on the respective RHS are simultaneously zero. One can check that the spin wave dispersions of Eqs.(A.2) and (A.3) have the following symmetry properties

$$\omega_i(k_x, k_y) = \omega_i(-k_x, -k_y) \ \ (\textit{time reversal symmetry}),$$
$$\omega_i(k_x, -k_y) = \omega_i(-k_x, k_y),$$

for $i = 1, 2, 3, 4$, which can be employed to simplify the calculations. As far as the magnon phonon scattering matrix is concerned, the $\Lambda'(\boldsymbol{k}, \boldsymbol{q})$ matrix on the RHS of Eq.(2.31) has the following form

$$\Lambda'(\boldsymbol{k}, \boldsymbol{q}) = \begin{bmatrix} A'(\boldsymbol{q}) & 0 & 0 & D'(\boldsymbol{k}, \boldsymbol{q}) & 0 & B'(\boldsymbol{k}, \boldsymbol{q}) & 0 & C'(\boldsymbol{k}, \boldsymbol{q}) \\ 0 & A'(\boldsymbol{q}) & D'(-\boldsymbol{k}, \boldsymbol{q}) & 0 & B'(-\boldsymbol{k}, \boldsymbol{q}) & 0 & C'(-\boldsymbol{k}, \boldsymbol{q}) & 0 \\ 0 & D'(\boldsymbol{k}, \boldsymbol{q}) & A'(\boldsymbol{q}) & 0 & 0 & C'(\boldsymbol{k}, \boldsymbol{q}) & 0 & B'(\boldsymbol{k}, \boldsymbol{q}) \\ D'(-\boldsymbol{k}, \boldsymbol{q}) & 0 & 0 & A'(\boldsymbol{q}) & C'(-\boldsymbol{k}, \boldsymbol{q}) & 0 & B'(-\boldsymbol{k}, \boldsymbol{q}) & 0 \\ 0 & B'(\boldsymbol{k}, \boldsymbol{q}) & 0 & C'(\boldsymbol{k}, \boldsymbol{q}) & A'(\boldsymbol{q}) & 0 & 0 & D'(\boldsymbol{k}, \boldsymbol{q}) \\ B'(-\boldsymbol{k}, \boldsymbol{q}) & 0 & C'(-\boldsymbol{k}, \boldsymbol{q}) & 0 & 0 & A'(\boldsymbol{q}) & D'(-\boldsymbol{k}, \boldsymbol{q}) & 0 \\ 0 & C'(\boldsymbol{k}, \boldsymbol{q}) & 0 & B'(\boldsymbol{k}, \boldsymbol{q}) & 0 & D'(\boldsymbol{k}, \boldsymbol{q}) & A'(\boldsymbol{q}) & 0 \\ C'(-\boldsymbol{k}, \boldsymbol{q}) & 0 & B'(-\boldsymbol{k}, \boldsymbol{q}) & 0 & D'(-\boldsymbol{k}, \boldsymbol{q}) & 0 & 0 & A'(\boldsymbol{q}) \end{bmatrix}, \tag{A.4}$$

and further, for *long-wavelength acoustic phonons* it is

$$\begin{aligned} A'(\boldsymbol{q}) &= i\Big[\left(\hat{e}_{\boldsymbol{qs}} \cdot \vec{J}^{(1)}(\vec{\delta}_1)\right) \left(\vec{q} \cdot \vec{\delta}_1\right) - \left(\hat{e}_{\boldsymbol{qs}} \cdot \vec{J}^{(1)}(\vec{\delta}_2)\right) \left(\vec{q} \cdot \vec{\delta}_2\right) \\ &- \left(\hat{e}_{\boldsymbol{qs}} \cdot \vec{J}^{(1)}(\vec{\delta}_3)\right) \left(\vec{q} \cdot \vec{\delta}_3\right) + 2 \left(\hat{e}_{\boldsymbol{qs}} \cdot \vec{K}^{(1)}(\vec{\delta}_1)\right) \left(\vec{q} \cdot \vec{\delta}_1\right) \Big] \\ &= i\frac{4\pi n}{3} \left(\hat{e}_{\boldsymbol{qs}} \cdot \vec{J}^{(1)} + \hat{e}_{\boldsymbol{qs}} \cdot \vec{K}^{(1)}\right), \end{aligned}$$

$$\begin{aligned} B'(\boldsymbol{k}, \boldsymbol{q}) &= i \left(\hat{e}_{\boldsymbol{qs}} \cdot \vec{J}^{(1)}(\vec{\delta}_1)\right) \left(\vec{q} \cdot \vec{\delta}_1\right) e^{-i\vec{k} \cdot \vec{\delta}_1} \\ &= i\frac{2\pi n}{3} \left(\hat{e}_{\boldsymbol{qs}} \cdot \vec{J}^{(1)}\right) \eta^{-2}, \end{aligned}$$

$$C'(\boldsymbol{k},\boldsymbol{q}) = i\Big[\Big(\hat{e}_{\boldsymbol{q}s}\cdot\vec{K}^{(1)}(\vec{\delta}_3)\Big)\Big(\vec{q}\cdot\vec{\delta}_3\Big)\,e^{-i\vec{k}\cdot\vec{\delta}_3}$$
$$-\Big(\hat{e}_{\boldsymbol{q}s}\cdot\vec{K}^{(1)}(\vec{\delta}_2)\Big)\Big(\vec{q}\cdot\vec{\delta}_2\Big)\,e^{-i\vec{k}\cdot\vec{\delta}_2}\Big]$$
$$= -2im\pi\Big(\hat{e}_{\boldsymbol{q}s}\cdot\vec{K}^{(1)}\Big)\,\zeta\eta,$$

$$D'(\boldsymbol{k},\boldsymbol{q}) = i\Bigg(\Big[\Big(\hat{e}_{\boldsymbol{q}s}\cdot\vec{J}^{(1)}(\vec{\delta}_2)\Big)+\Big(\hat{e}_{\boldsymbol{q}s}\cdot\vec{K}^{(1)}(\vec{\delta}_2)\Big)\Big]$$
$$\Big(\vec{q}\cdot\vec{\delta}_2\Big)\,e^{-i\vec{k}\cdot\vec{\delta}_2}+\Big[\Big(\hat{e}_{\boldsymbol{q}s}\cdot\vec{J}^{(1)}(\vec{\delta}_3)\Big)+\Big(\hat{e}_{\boldsymbol{q}s}\cdot\vec{K}^{(1)}(\vec{\delta}_3)\Big)\Big]$$
$$\Big(\vec{q}\cdot\vec{\delta}_3\Big)\,e^{-i\vec{k}\cdot\vec{\delta}_3}\Bigg) = -i\frac{2\pi n}{3}\Big(\hat{e}_{\boldsymbol{q}s}\cdot\vec{J}^{(1)}+\hat{e}_{\boldsymbol{q}s}\cdot\vec{K}^{(1)}\Big)\,\zeta\eta,$$

where

$$\boldsymbol{q} = m\frac{2\pi}{a}\hat{\boldsymbol{e}}_X + n\frac{2\pi}{b}\hat{\boldsymbol{e}}_Y,\quad a=\alpha\sqrt{3},\ b=3\alpha,\quad m,n\in\mathbb{Z},$$

and also, $\zeta = e^{i\pi h} = \zeta^{-1}$ and $\eta = e^{ik\pi/3}$. Notice that in the calculation of the parameters $B'(\boldsymbol{k},\boldsymbol{q})$, $C'(\boldsymbol{k},\boldsymbol{q})$ and $D'(\boldsymbol{k},\boldsymbol{q})$ above, the substitution $\boldsymbol{k}\to-\boldsymbol{k}$ implies the substitution $(h,k)\to(-h,-k)$ (i.e. switch the sign of the magnon wavector components; see the definitions prior to Eqs.(A.2) and (A.3)), and further, it was assumed that the exchange couplings $\vec{J}^{(1)}$ and $\vec{K}^{(1)}$ are bond independent, as a result of which the bond direction dependence was dropped.

A.2 Stripy phase

For the stripy phase the magnetic unit cell is again defined by the gray rectangle of sides a and b shown in Fig. A.1, consisting of four magnetic moments A, B, C and D, with A and B pointing along the positive X-axis, and C and D pointing along the negative X-axis. Choosing the positive spin quantization axis along the negative X-axis again, at the sites A and B we employ

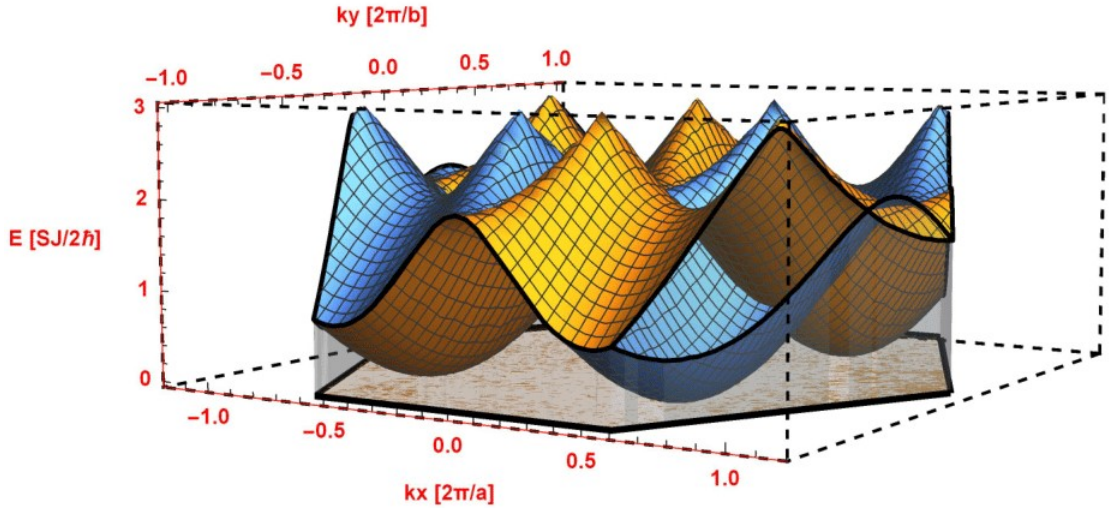

Figure A.4: Lower spin wave dispersion relations of the stripy phase, as given by Eqs.(A.6). The yellow surface corresponds to $\omega_1(\boldsymbol{k})$ and the blue surface to $\omega_2(\boldsymbol{k})$. Notice that the magnon wavevector components k_x and k_y are measured in units of $\frac{2\pi}{a}$ and $\frac{2\pi}{b}$ respectively and the spin wave energy is measured in units of $\frac{SJ}{2\hbar}$. The shaded hexagon within the Oxy plane is the 1BZ of the honeycomb lattice. The plot is for $K/J = -1$ and $\alpha = 2\pi/3$.

the bosonization given by the Eqs.(2.17)-(2.19), while at the sites C and D we employ the bosonization given by the Eqs.(2.14)-(2.16). The nn bonds that interact through the Hamiltonian of Eq. (2.1) as well as the Kitaev couplings are the same as in the case of the zig-zag phase. Using the representation of the x- and y-spin components in terms of the ladder spin operators to write the total Hamiltonian in terms of the $S_i^{||}$, S_i^+ and S_i^- operators, performing the bosonization as elaborated above, and Fourier transforming according to the convention of Eqs.(2.20) and (2.21), ones finds the classical ground state energy $\mathcal{H}_{classical} = \frac{NS^2}{2}(-J + 2K)$, and the following *spin wave mode matrix*

$M(\boldsymbol{k})$ (reference to Eq.(2.22) and the notation thereof):

$$M(\boldsymbol{k}) = \begin{bmatrix} A & B^*(\boldsymbol{k}) & 0 & C^*(\boldsymbol{k}) & 0 & 0 & 0 & D^*(\boldsymbol{k}) \\ B(\boldsymbol{k}) & A & C(\boldsymbol{k}) & 0 & 0 & 0 & D(\boldsymbol{k}) & 0 \\ 0 & C^*(\boldsymbol{k}) & A & B^*(\boldsymbol{k}) & 0 & D^*(\boldsymbol{k}) & 0 & 0 \\ C(\boldsymbol{k}) & 0 & B(\boldsymbol{k}) & A & D(\boldsymbol{k}) & 0 & 0 & 0 \\ 0 & 0 & 0 & D^*(\boldsymbol{k}) & A & B^*(\boldsymbol{k}) & 0 & C^*(\boldsymbol{k}) \\ 0 & 0 & D(\boldsymbol{k}) & 0 & B(\boldsymbol{k}) & A & C(\boldsymbol{k}) & 0 \\ 0 & D^*(\boldsymbol{k}) & 0 & 0 & 0 & C^*(\boldsymbol{k}) & A & B^*(\boldsymbol{k}) \\ D(\boldsymbol{k}) & 0 & 0 & 0 & C(\boldsymbol{k}) & 0 & B(\boldsymbol{k}) & A \end{bmatrix}, \tag{A.5}$$

where we defined the following parameters

$$\begin{aligned} A &= J - 2K, \\ B(\boldsymbol{k}) &= Je^{-i\vec{k}\cdot\vec{\delta}_1} = J\eta^{-2}, \\ C(\boldsymbol{k}) &= K\left(e^{-i\vec{k}\cdot\vec{\delta}_3} - e^{-i\vec{k}\cdot\vec{\delta}_2}\right) = 2iK\eta\sin(\pi h), \\ D(\boldsymbol{k}) &= (J+K)\left(e^{-i\vec{k}\cdot\vec{\delta}_3} + e^{-i\vec{k}\cdot\vec{\delta}_2}\right) = 2(J+K)\eta\cos(\pi h). \end{aligned}$$

and as previously it is

$$\zeta = e^{i\pi h} = \zeta^{-1} \quad (\zeta^2 = 1 = \zeta\zeta^{-1}), \quad \eta = e^{ik\pi/3}.$$

Diagonalizing the dynamical matrix $D = I_- M$ as described in Eq.(2.27) in Sec.2.2, we obtain the following *magnon normal modes*:

$$\omega_1 = \sqrt{\Omega_1 - \sqrt{\Omega_2}}, \quad \omega_2 = \sqrt{\Omega_3 - \sqrt{\Omega_4}} \tag{A.6}$$

$$\omega_3 = \sqrt{\Omega_1 + \sqrt{\Omega_2}}, \quad \omega_4 = \sqrt{\Omega_3 + \sqrt{\Omega_4}}, \tag{A.7}$$

where the following parameters were used

$$\Omega_1 = A^2 - |D|^2 + |B - C|^2,$$
$$\Omega_2 = 4|A(B - C)|^2 - |D(B^* - C^*) - D^*(B - C)|^2,$$
$$\Omega_3 = A^2 - |D|^2 + |B + C|^2,$$
$$\Omega_4 = 4|A(B + C)|^2 - |D(B^* + C^*) - D^*(B + C)|^2.$$

The spin wave dispersions of Eq.(A.6) are plotted in Fig.A.4 and those of Eq.(A.7) are plotted in Fig.A.5. As can be seen from Figs.A.4 and A.5 (vertical axis), the lower and the upper magnon bands are well-separated in energy from each other. At low enough temperatures, as far as the magnon-phonon interaction is concerned, only the parts of the spin wave spectra around the *spin wave valleys*, and in this case the lower magnon bands are of interest. The lower energy magnon valley $\boldsymbol{k}$-space positions are found from the conditions that $\omega_i = 0$, $i = 1, 2$, which can be solved as was detailed in the previous section. One can check that the spin wave dispersions of Eqs.(A.6) and (A.7) have the symmetry properties: $\omega_i(k_x, k_y) = \omega_i(-k_x, -k_y)$ (*time reversal symmetry*), as well as $\omega_i(k_x, -k_y) = \omega_i(-k_x, k_y)$, for $i = 1, 2, 3, 4$, which can further be employed to simplify the calculations. As far as the magnon phonon scattering matrix is concerned, the $\Lambda'(\boldsymbol{k}, \boldsymbol{q})$ matrix on the RHS of Eq.(2.31) has the following form

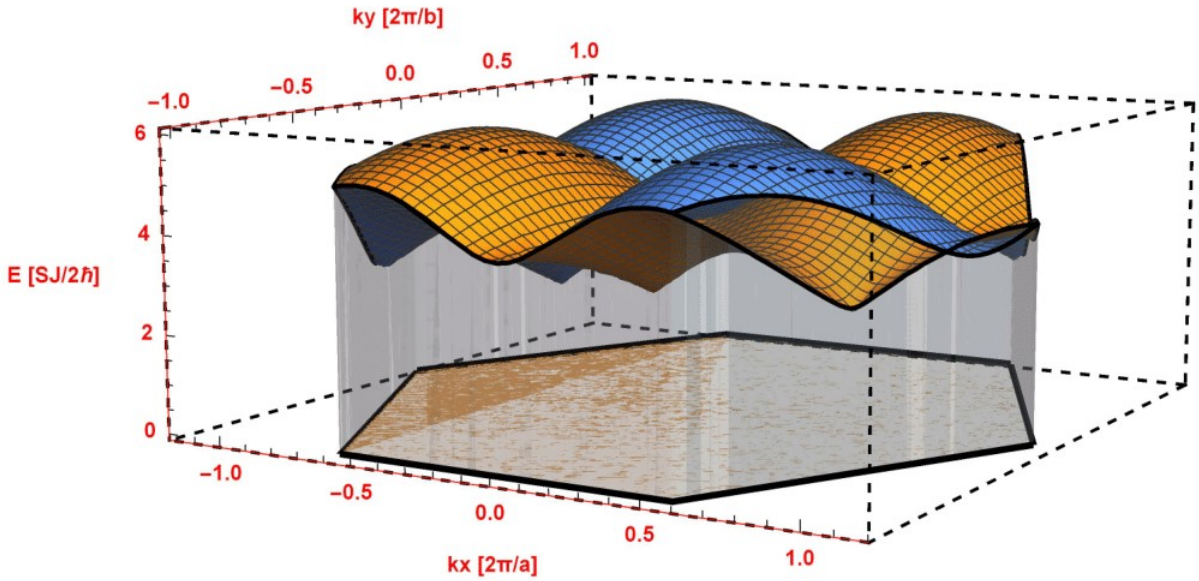

Figure A.5: Upper spin wave dispersion relations of the stripy phase, as given by Eqs.(A.7). The yellow surface corresponds to $\omega_3(\boldsymbol{k})$ and the blue surface to $\omega_4(\boldsymbol{k})$. Notice that the magnon wavevector components k_x and k_y are measured in units of $\frac{2\pi}{a}$ and $\frac{2\pi}{b}$ respectively and the spin wave energy is measured in units of $\frac{SJ}{2\hbar}$. The shaded hexagon within the Oxy plane is the 1BZ of the honeycomb lattice. The plot is for $K/J = -1$ and $\alpha = 2\pi/3$.

$$\Lambda'(\boldsymbol{k},\boldsymbol{q}) = \begin{bmatrix} A'(\boldsymbol{q}) & B'(-\boldsymbol{k},\boldsymbol{q}) & 0 & C'(-\boldsymbol{k},\boldsymbol{q}) & 0 & 0 & 0 & D'(-\boldsymbol{k},\boldsymbol{q}) \\ B'(\boldsymbol{k},\boldsymbol{q}) & A'(\boldsymbol{q}) & C'(\boldsymbol{k},\boldsymbol{q}) & 0 & 0 & 0 & D'(\boldsymbol{k},\boldsymbol{q}) & 0 \\ 0 & C'(-\boldsymbol{k},\boldsymbol{q}) & A'(\boldsymbol{q}) & B'(-\boldsymbol{k},\boldsymbol{q}) & 0 & D'(-\boldsymbol{k},\boldsymbol{q}) & 0 & 0 \\ C'(\boldsymbol{k},\boldsymbol{q}) & 0 & B'(\boldsymbol{k},\boldsymbol{q}) & A'(\boldsymbol{q}) & D'(\boldsymbol{k},\boldsymbol{q}) & 0 & 0 & 0 \\ 0 & 0 & 0 & D'(-\boldsymbol{k},\boldsymbol{q}) & A'(\boldsymbol{q}) & B'(-\boldsymbol{k},\boldsymbol{q}) & 0 & C'(-\boldsymbol{k},\boldsymbol{q}) \\ 0 & 0 & D'(\boldsymbol{k},\boldsymbol{q}) & 0 & B'(\boldsymbol{k},\boldsymbol{q}) & A'(\boldsymbol{q}) & C'(\boldsymbol{k},\boldsymbol{q}) & 0 \\ 0 & D'(-\boldsymbol{k},\boldsymbol{q}) & 0 & 0 & 0 & C'(-\boldsymbol{k},\boldsymbol{q}) & A'(\boldsymbol{q}) & B'(-\boldsymbol{k},\boldsymbol{q}) \\ D'(\boldsymbol{k},\boldsymbol{q}) & 0 & 0 & 0 & C'(\boldsymbol{k},\boldsymbol{q}) & 0 & B'(\boldsymbol{k},\boldsymbol{q}) & A'(\boldsymbol{q}) \end{bmatrix}, \tag{A.8}$$

where the parameters $B'(\boldsymbol{k},\boldsymbol{q})$, $C'(\boldsymbol{k},\boldsymbol{q})$ and $D'(\boldsymbol{k},\boldsymbol{q})$ are defined exactly as in the zig-zag phase, with the following modification for the $A'(\boldsymbol{q})$

parameter

$$A'(\boldsymbol{q}) = -i\frac{4\pi n}{3}\left(\hat{e}_{\boldsymbol{q}s}\cdot\vec{J}^{(1)} + \hat{e}_{\boldsymbol{q}s}\cdot\vec{K}^{(1)}\right),$$

and further,

$$\boldsymbol{q} = m\frac{2\pi}{a}\hat{\boldsymbol{e}}_X + n\frac{2\pi}{b}\hat{\boldsymbol{e}}_Y,\ \ a=\alpha\sqrt{3},\ b=3\alpha,\ \ m,n\in\mathbb{Z},$$

$\zeta = e^{i\pi h} = \zeta^{-1}$ and $\eta = e^{ik\pi/3}$. Notice again that in the calculation of the parameters $B'(\boldsymbol{k},\boldsymbol{q})$, $C'(\boldsymbol{k},\boldsymbol{q})$ and $D'(\boldsymbol{k},\boldsymbol{q})$ above, the substitution $\boldsymbol{k}\to-\boldsymbol{k}$ implies the substitution $(h,k)\to(-h,-k)$, and it was assumed that the exchange couplings J and K as well as the couplings $\vec{J}^{(1)}$ and $\vec{K}^{(1)}$ are bond independent, as a result of which the bond direction dependence was dropped.

A.3 Néel phase

For the Néel phase the magnetic unit cell coincides with the chemical unit cell defined by the parallelogram of sides $\boldsymbol{t_1}$ and $\boldsymbol{t_2}$ (see Fig. A.1), and consists of two magnetic moments A, B, with A pointing along the positive X-axis, and B pointing along the negative X-axis. Choosing the positive spin quantization axis along the negative X-axis again, at the site A we employ the bosonization given by the Eqs.(2.17)-(2.19), while at the site B we employ the bosonization given by the Eqs.(2.14)-(2.16). The bond dependent Kitaev couplings are defined as in the zig-zag phase, except that now only the nn bonds at sites A and B are taken into account leading to a total of three bonds. Using the representation of the x- and y-spin components in terms of the ladder spin operators to write the total Hamiltonian in terms of the

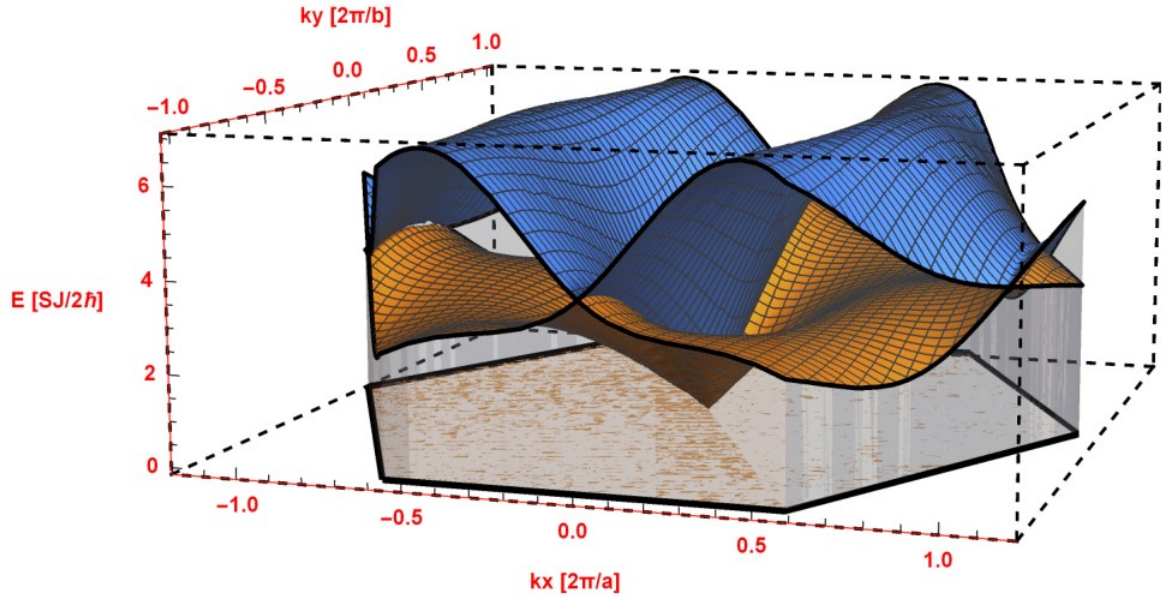

Figure A.6: Spin wave dispersion relations of the Néel phase, as given by Eqs.(A.10). The yellow surface corresponds to $\omega_1(\boldsymbol{k})$ and the blue surface to $\omega_2(\boldsymbol{k})$. Notice that the magnon wavevector components k_x and k_y are measured in units of $\frac{2\pi}{a}$ and $\frac{2\pi}{b}$ respectively and the spin wave energy is measured in units of $\frac{SJ}{2\hbar}$. The shaded hexagon within the Oxy plane is the 1BZ of the honeycomb lattice. The plot is for $K/J = 1$ and $\alpha = 2\pi/3$.

$S_i^{||}$, S_i^+ and S_i^- operators, performing the bosonization as elaborated above, and Fourier transforming according to the convention of Eqs.(2.20) and (2.21), ones finds the classical ground state energy $\mathcal{H}_{classical} = -\frac{NS^2}{2}(3J + 2K)$, and the following *spin wave mode matrix* $M(\boldsymbol{k})$ (reference to Eq.(2.22) and the notation thereof):

$$M(\boldsymbol{k}) = \begin{bmatrix} A & C(\boldsymbol{k}) & 0 & B(\boldsymbol{k}) \\ C^*(\boldsymbol{k}) & A & B^*(\boldsymbol{k}) & 0 \\ 0 & B(\boldsymbol{k}) & A & C(\boldsymbol{k}) \\ B^*(\boldsymbol{k}) & 0 & C^*(\boldsymbol{k}) & A \end{bmatrix}, \tag{A.9}$$

where we defined the following parameters

$$
\begin{aligned}
&A = 3J + 2K, \\
&B(\boldsymbol{k}) = J(\vec{\delta}_1)e^{-i\vec{k}\cdot\vec{\delta}_1} + \left(J(\vec{\delta}_3) + K(\vec{\delta}_3)\right) e^{-i\vec{k}\cdot\vec{\delta}_3} \\
&+ \left(J(\vec{\delta}_2) + K(\vec{\delta}_2)\right) e^{-i\vec{k}\cdot\vec{\delta}_2} = J\eta^{-2} + 2(J+K)\eta\cos(\pi h), \\
&C(\boldsymbol{k}) = K(\vec{\delta}_3)e^{-i\vec{k}\cdot\vec{\delta}_3} - K(\vec{\delta}_2)e^{-i\vec{k}\cdot\vec{\delta}_2} = 2iK\eta\sin(\pi h),
\end{aligned}
$$

in conjunction with the definitions

$$
\zeta = e^{i\pi h} = \zeta^{-1} \quad (\zeta^2 = 1 = \zeta\zeta^{-1}), \quad \eta = e^{ik\pi/3}.
$$

Diagonalizing the dynamical matrix $D = I_{-}M$ as described in Eq.(2.27) in Sec.2.2, we obtain the following *magnon normal modes*:

$$
\omega_1 = \sqrt{\Omega_1 - \sqrt{\Omega_2}},\ \omega_2 = \sqrt{\Omega_1 + \sqrt{\Omega_2}}, \tag{A.10}
$$

where the following parameters were used

$$
\begin{aligned}
&\Omega_1 = A^2 - |B|^2 + |C|^2, \\
&\Omega_2 = 4A^2\,|C|^2 + (B^*C - C^*B)^2.
\end{aligned}
$$

The spin wave dispersions of Eq.(A.10) are plotted in Fig.A.6. At low enough temperatures, as far as the magnon-phonon interaction is concerned, only the parts of the spin wave spectra around the *spin wave valleys* are of interest, which in this case are located at the Γ-point of the 1BZ (as opposed to the previous phases). The exact magnon valley $\boldsymbol{k}$-space positions are found from the conditions that $\omega_i = 0$, $i = 1, 2$, which can be solved as was detailed in the previous sections. One can check that the spin wave dispersions of Eq.(A.10) have

the symmetry properties: $\omega_i(k_x, k_y) = \omega_i(-k_x, -k_y)$ (*time reversal symmetry*) as well as $\omega_i(k_x, -k_y) = \omega_i(-k_x, k_y)$, for $i = 1, 2$, which can further be employed to simplify the calculations. As far as the magnon phonon scattering matrix is concerned, the $\Lambda'(\boldsymbol{k}, \boldsymbol{q})$ matrix on the RHS of Eq.(2.31) has the following form

$$\Lambda'(\boldsymbol{k}, \boldsymbol{q}) = \begin{bmatrix} A'(\boldsymbol{q}) & C'(\boldsymbol{k}, \boldsymbol{q}) & 0 & B'(\boldsymbol{k}, \boldsymbol{q}) \\ C'(-\boldsymbol{k}, \boldsymbol{q}) & A'(\boldsymbol{q}) & B'(-\boldsymbol{k}, \boldsymbol{q}) & 0 \\ 0 & B'(\boldsymbol{k}, \boldsymbol{q}) & A'(\boldsymbol{q}) & C'(\boldsymbol{k}, \boldsymbol{q}) \\ B'(-\boldsymbol{k}, \boldsymbol{q}) & 0 & C'(-\boldsymbol{k}, \boldsymbol{q}) & A'(\boldsymbol{q}) \end{bmatrix}, \tag{A.11}$$

where the parameters $A'(\boldsymbol{q})$, $B'(\boldsymbol{k}, \boldsymbol{q})$ and $C'(\boldsymbol{k}, \boldsymbol{q})$ are defined as below

$$\begin{aligned} A'(\boldsymbol{q}) &= i\frac{4\pi}{3}(\hat{e}_{\boldsymbol{qs}} \cdot \vec{K}^{(1)}), \\ B'(\boldsymbol{k}, \boldsymbol{q}) &= i\frac{2\pi n}{3}\left(\hat{e}_{\boldsymbol{qs}} \cdot \vec{J}^{(1)}\right)\eta^{-2} \\ &- i\frac{2\pi n}{3}\left(\hat{e}_{\boldsymbol{qs}} \cdot \vec{J}^{(1)} + \hat{e}_{\boldsymbol{qs}} \cdot \vec{K}^{(1)}\right)\zeta\eta, \\ C'(\boldsymbol{k}, \boldsymbol{q}) &= -2im\pi\left(\hat{e}_{\boldsymbol{qs}} \cdot \vec{K}^{(1)}\right)\zeta\eta, \end{aligned}$$

and further,

$$\boldsymbol{q} = m\frac{2\pi}{a}\hat{\boldsymbol{e}}_X + n\frac{2\pi}{b}\hat{\boldsymbol{e}}_Y, \quad a = \alpha\sqrt{3},\ b = 3\alpha, \quad m, n \in \mathbb{Z},$$

$\zeta = e^{i\pi h} = \zeta^{-1}$ and $\eta = e^{ik\pi/3}$. Notice that in the calculation of the parameters $B'(\boldsymbol{k}, \boldsymbol{q})$ and $C'(\boldsymbol{k}, \boldsymbol{q})$ above, the substitution $\boldsymbol{k} \to -\boldsymbol{k}$ implies the substitution $(h, k) \to (-h, -k)$, and it was assumed that the exchange couplings J and K as well as the couplings $\vec{J}^{(1)}$ and $\vec{K}^{(1)}$ are bond independent, as a result of which the bond direction dependence was dropped.

A.4 Ferromagnetic phase

For the ferromagnetic phase the magnetic unit cell again coincides with the chemical unit cell defined by the parallelogram of sides $\boldsymbol{t_1}$ and $\boldsymbol{t_2}$ (see Fig. A.1), and consists of two magnetic moments A, B, with A and B both pointing along the positive X-axis. Choosing the positive spin quantization axis along the negative X-axis again, at both sites we employ the bosonization given by the Eqs.(2.17)-(2.19). The nn bonds that interact through the Hamiltonian of Eq. (2.1) as well as the definition of the Kitaev couplings are the same as in the case of the Néel phase. Using the representation of the x- and y-spin components in terms of the ladder spin operators to write the total Hamiltonian in terms of the $S_i^{||}$, S_i^+ and S_i^- operators, performing the bosonization as elaborated above, and Fourier transforming according to the convention of Eqs.(2.20) and (2.21), ones finds the classical ground state energy $\mathcal{H}_{classical} = \frac{NS^2}{2}(3J + 2K)$, and the following *spin wave mode matrix* $M(\boldsymbol{k})$ (reference to Eq.(2.22) and the notation thereof):

$$M(\boldsymbol{k}) = \begin{bmatrix} A & B(\boldsymbol{k}) & 0 & C(\boldsymbol{k}) \\ B^*(\boldsymbol{k}) & A & C^*(\boldsymbol{k}) & 0 \\ 0 & C(\boldsymbol{k}) & A & B(\boldsymbol{k}) \\ C^*(\boldsymbol{k}) & 0 & B^*(\boldsymbol{k}) & A \end{bmatrix}, \tag{A.12}$$

where the parameters $B(\boldsymbol{k})$ and $C(\boldsymbol{k})$ are defined exactly as in the Néel phase, except for the parameter A which is modified as below

$$A = -3J - 2K. \tag{A.13}$$

Diagonalizing the dynamical matrix $D = I_- M$ as described in Eq.(2.27)

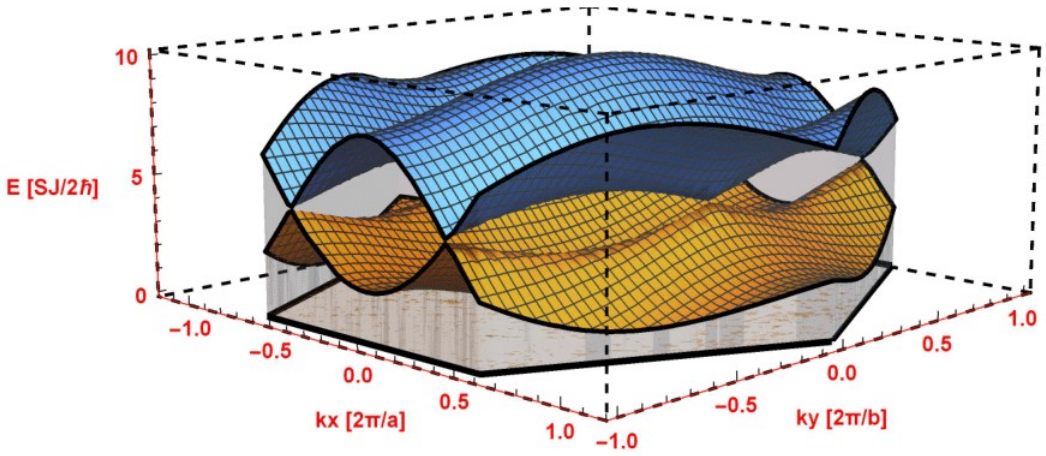

Figure A.7: Spin wave dispersion relations of the ferromagnetic phase, as given by Eqs.(A.14). The yellow surface corresponds to $\omega_1(\boldsymbol{k})$ and the blue surface to $\omega_2(\boldsymbol{k})$. Notice that the magnon wavevector components k_x and k_y are measured in units of $\frac{2\pi}{a}$ and $\frac{2\pi}{b}$ respectively and the spin wave energy is measured in units of $\frac{SJ}{2\hbar}$. The shaded hexagon within the Oxy plane is the 1BZ of the honeycomb lattice. The plot is for $K/J = 1$ and $\alpha = 2\pi/3$.

in Sec.2.2, we obtain the following *magnon normal modes*:

$$\omega_1 = \sqrt{\Omega_1 - \sqrt{\Omega_2}},\ \omega_2 = \sqrt{\Omega_1 + \sqrt{\Omega_2}}, \tag{A.14}$$

where the following parameters were used

$$\Omega_1 = A^2 - |C|^2 + |B|^2,$$
$$\Omega_2 = 4A^2\,|B|^2 + (B^*C - C^*B)^2.$$

The spin wave dispersions of Eq.(A.14) are plotted in Fig.A.7. At low enough temperatures, as far as the magnon-phonon interaction processes are concerned, only the part of the lower spin wave spectum around the *spin wave valley* is of interest, which in this case is again located at the Γ-point of the 1BZ. The

exact magnon valley $\boldsymbol{k}$-space position is found from the condition that $\omega_i = 0$, $i = 1$, which can be solved as was detailed in the previous sections. One can check that the spin wave dispersions of the ferromagnetic phase as well have the symmetry properties: $\omega_i(k_x, k_y) = \omega_i(-k_x, -k_y)$ (*time reversal symmetry*) as well as $\omega_i(k_x, -k_y) = \omega_i(-k_x, k_y)$, for $i = 1, 2$. It should be stressed that the spin wave dispersions of both the Néel and the ferromagnetic phase, in Figs.A.6 and A.7 respectively, are not exactly isotropic around the respective spin wave valleys. Lastly, for the magnon phonon scattering matrix $\Lambda'(\boldsymbol{k}, \boldsymbol{q})$ of the RHS of Eq.(2.31) it is

$$\Lambda'(\boldsymbol{k}, \boldsymbol{q}) = \begin{bmatrix} A'(\boldsymbol{q}) & B'(\boldsymbol{k}, \boldsymbol{q}) & 0 & C'(\boldsymbol{k}, \boldsymbol{q}) \\ B'(-\boldsymbol{k}, \boldsymbol{q}) & A'(\boldsymbol{q}) & C'(-\boldsymbol{k}, \boldsymbol{q}) & 0 \\ 0 & C'(\boldsymbol{k}, \boldsymbol{q}) & A'(\boldsymbol{q}) & B'(\boldsymbol{k}, \boldsymbol{q}) \\ C'(-\boldsymbol{k}, \boldsymbol{q}) & 0 & B'(-\boldsymbol{k}, \boldsymbol{q}) & A'(\boldsymbol{q}) \end{bmatrix}, \tag{A.15}$$

where the parameters $B'(\boldsymbol{k}, \boldsymbol{q})$ and $C'(\boldsymbol{k}, \boldsymbol{q})$ are defined exactly as in the Néel phase, with the following modification for the $A'(\boldsymbol{q})$ parameter

$$A'(\boldsymbol{q}) = -i\frac{4\pi}{3}(\hat{e}_{\boldsymbol{q}s} \cdot \vec{K}^{(1)}),$$

and further,

$$\boldsymbol{q} = m\frac{2\pi}{a}\hat{\boldsymbol{e}}_X + n\frac{2\pi}{b}\hat{\boldsymbol{e}}_Y, \quad a = \alpha\sqrt{3},\ b = 3\alpha, \quad m, n \in \mathbb{Z},$$

$\zeta = e^{i\pi h} = \zeta^{-1}$ and $\eta = e^{ik\pi/3}$. It is again noticed that in the calculation of the parameters $B'(\boldsymbol{k}, \boldsymbol{q})$ and $C'(\boldsymbol{k}, \boldsymbol{q})$ above, the substitution $\boldsymbol{k} \to -\boldsymbol{k}$ implies the substitution $(h, k) \to (-h, -k)$, and it was assumed that the exchange couplings J and K as well as the couplings $\vec{J}^{(1)}$ and $\vec{K}^{(1)}$ are bond independent, as a result of which the bond direction dependence was dropped.

Appendix B

Boltzmann kinetic equation and derivation of thermal conductivity formula in the relaxation time approximation

Consider the phase space of a multi-particle system of non-interacting particles, more generally non-interacting in the *mean field* sense. For such a case, instead of the multi-particle distribution function one can recourse to the so-called *reduced distribution functions* [82], and more specifically to the *single-particle distribution function* $f(\boldsymbol{r}, \boldsymbol{q}, t)$ without introducing any further approximations. Let us now focus on the motion of the particles whose phase space coordinates lie within the volume $d\boldsymbol{r}d\boldsymbol{q}$ around the phase space point $(\boldsymbol{r}, \boldsymbol{q})$ at time t. If no collisions occur, then at time $t + dt$ the phase space coordinates of all those particles flow into the region $d\boldsymbol{r}'d\boldsymbol{q}'$ around the point $(\boldsymbol{r}', \boldsymbol{q}')$, where obviously $\boldsymbol{r}' = \boldsymbol{r} + \dot{\boldsymbol{r}}dt$ and $\boldsymbol{q}' = \boldsymbol{q} + \dot{\boldsymbol{q}}dt$. Conservation of the number of particles (since no collisions occur) dictates that

$$f(\boldsymbol{r}, \boldsymbol{q}, t)d\boldsymbol{r}d\boldsymbol{q} = f(\boldsymbol{r}', \boldsymbol{q}', t + dt)d\boldsymbol{r}'d\boldsymbol{q}' = f(\boldsymbol{r} + \dot{\boldsymbol{r}}dt, \boldsymbol{q} + \dot{\boldsymbol{q}}dt, t + dt)d\boldsymbol{r}'d\boldsymbol{q}',$$

where $f(\boldsymbol{r}, \boldsymbol{q}, t)$ is the single-particle dynamical phase-space distribution function. Liouville's theorem states that $d\boldsymbol{r}d\boldsymbol{q} = d\boldsymbol{r}'d\boldsymbol{q}'$, implying that

$$f(\boldsymbol{r} + \dot{\boldsymbol{r}}dt, \boldsymbol{q} + \dot{\boldsymbol{q}}dt, t + dt) = f(\boldsymbol{r}, \boldsymbol{q}, t). \tag{B.1}$$

Furthemore,

$$f(\boldsymbol{r}+\dot{\boldsymbol{r}}dt, \boldsymbol{q}+\dot{\boldsymbol{q}}dt, t+dt) = f(\boldsymbol{r},\boldsymbol{q},t) + \frac{\partial f}{\partial \boldsymbol{r}}\dot{\boldsymbol{r}}dt + \frac{\partial f}{\partial \boldsymbol{q}}\dot{\boldsymbol{q}}dt + \frac{\partial f}{\partial t}dt. \quad \text{(B.2)}$$

Combining Eqs.(B.1), (B.2) we get

$$\frac{df}{dt} = \frac{f(\boldsymbol{r}+\dot{\boldsymbol{r}}dt, \boldsymbol{q}+\dot{\boldsymbol{q}}dt, t+dt) - f(\boldsymbol{r},\boldsymbol{q},t)}{dt} = \dot{\boldsymbol{r}}\frac{\partial f}{\partial \boldsymbol{r}} + \dot{\boldsymbol{q}}\frac{\partial f}{\partial \boldsymbol{q}} + \frac{\partial f}{\partial t} = 0. \quad \text{(B.3)}$$

Now, if collisions do occur during the infinitesimal time interval dt, some particles are scattered out (of the aforementioned multi-particle distribution function) whereas other particles are scattered in (the aforementioned multi-particle distribution function), upon flowing from the phase space point $(\boldsymbol{r},\boldsymbol{q})$ to the phase space point $(\boldsymbol{r}',\boldsymbol{q}')$, infinitesimally far away (within the phase space). As a result of it, the single-particle dynamical phase space distribution function does not satisfy Eq.(B.3), but instead it is (reducing the inscattering and outscattering from the multi-particle distribution function to a probability of inscattering and outscattering from the single-particle distribution function)

$$\frac{f(\boldsymbol{r}+\dot{\boldsymbol{r}}dt, \boldsymbol{q}+\dot{\boldsymbol{q}}dt, t+dt) - f(\boldsymbol{r},\boldsymbol{q},t)}{dt} = \left(\frac{df}{dt}\right)_{in} - \left(\frac{df}{dt}\right)_{out} \equiv \left(\frac{df}{dt}\right)_{coll}, \quad \text{(B.4)}$$

where the rightmost term accounts for the total change in the single-particle distribution function due to inscattering and outscattering processes, and is the so-called *collision term*. Combining Eqs. (B.3) and (B.4), to linear order in dt we get

$$\dot{\boldsymbol{r}}\frac{\partial f}{\partial \boldsymbol{r}} + \dot{\boldsymbol{q}}\frac{\partial f}{\partial \boldsymbol{q}} + \frac{\partial f}{\partial t} = \left(\frac{df}{dt}\right)_{coll}, \quad \text{(B.5)}$$

and this is the so-called *Boltzmann kinetic equation*. Now, let us apply the Boltzmann kinetic equation to the problem of heat transport. Let us focus on the low energy lattice degrees of freedom, which in the language of second quantization can be treated as non-interacting quasiparticles called *phonons*, and derive an expression for the thermal conductivity tensor.

When a temperature gradient (slowly varying in space, and time [82] in general) is present, phonons can be treated within the semiclassical approximation, i.e. they can be described by a semiclassical distribution function (from now on called *phonon distribution function*) whose dynamics obeys the Boltzmann kinetic equation. For heat transport, the phononic distribution function is actually non-uniform in real space only, due to the presence of a nonzero temperature gradient. As a result, the equation that governs the phase space variations of the phonon distribution function $f_s(\boldsymbol{r}, \boldsymbol{q}, t)$, for phonons of polarization s, has the following form

$$\boldsymbol{v}_s(\boldsymbol{q}) \frac{\partial f_s(\boldsymbol{r}, \boldsymbol{q}, t)}{\partial \boldsymbol{r}} + \frac{\partial f_s(\boldsymbol{r}, \boldsymbol{q}, t)}{\partial t} = \left(\frac{df_s}{dt} \right)_{coll}, \tag{B.6}$$

where $\boldsymbol{v}_s(\boldsymbol{q})$ is the group velocity of phonons of polarization s, given by $\boldsymbol{v}_s(\boldsymbol{q}) = \nabla_{\boldsymbol{q}} \omega_s(\boldsymbol{q})$. Taking into account the fact that the spatial non-uniformity of the phonon distribution function comes through the spatial variation of the temperature, in the so-called *stationary or steady state* case, one finds that

$$\boldsymbol{v}_s(\boldsymbol{q}) \cdot \nabla_{\boldsymbol{r}} T \frac{\partial f_s(\boldsymbol{q})}{\partial T} = \left(\frac{df_s}{dt} \right)_{coll}. \tag{B.7}$$

Eq.(B.7) is the *stationary Boltzmann equation* for phonons of polarization s. As was mentioned previously, in the phonon-dominated regime heat is mostly

carried by the phonons, which at low enough temperatures can be treated as non-interacting quasiparticles, which weakly interact with a bath which in this case is the magnons. Under those conditions we attempt to solve the stationary Boltzmann equation (B.7) within the so-called *relaxation time approximation*, and the current situation can be treated similarly to the impurity scattering of the electrons.

Quite generally, the collision term can be put into the following form (A denotes the area, and our analysis is adjusted to 2D)

$$\left(\frac{df_s}{dt}\right)_{coll} \equiv I[f_s] = \frac{1}{A}\sum_{\boldsymbol{q'}} \left(W_{\boldsymbol{q'}\to\boldsymbol{q}} - W_{\boldsymbol{q}\to\boldsymbol{q'}}\right), \tag{B.8}$$

where $W_{\boldsymbol{q'}\to\boldsymbol{q}}$ denotes the probability per unit time for a phonon to be scattered from $\boldsymbol{q'}$ to $\boldsymbol{q}$ in a given scattering process, which encompasses not only microscopic probabilities for quantum transitions but also the single-particle distribution function itself. More specifically, if the quantum transition probability per unit time, denoted as $w_{\boldsymbol{q'}\to\boldsymbol{q}}$ for a phononic scattering process from the state of wavevector $\boldsymbol{q'}$ to a state of wavevector $\boldsymbol{q}$ is known (this last quantity is directly related to the *magnon-phonon scattering matrix* of the analysis of the main text), then the probability $W_{\boldsymbol{q'}\to\boldsymbol{q}}$ can be expressed directly in terms of the microscopic probability $w_{\boldsymbol{q'}\to\boldsymbol{q}}$ and $f_s(\boldsymbol{r},\boldsymbol{q},t)$ (actually $f_s(\boldsymbol{q})$ for the stationary case that is of interest here). Furthermore, from Eq.(B.8) it is

$$\begin{aligned} I[f_s] &= \frac{1}{A}\sum_{\boldsymbol{q'}} \left(w_{\boldsymbol{q'}\to\boldsymbol{q}}\left(f_s(\boldsymbol{q})+1\right) - w_{\boldsymbol{q}\to\boldsymbol{q'}} f_s(\boldsymbol{q})\right) = \frac{1}{A}\sum_{\boldsymbol{q'}} w_{\boldsymbol{q'}\to\boldsymbol{q}}\left(f_s(\boldsymbol{q})+1\right) \\ &- \frac{1}{A}\sum_{\boldsymbol{q'}} w_{\boldsymbol{q}\to\boldsymbol{q'}} f_s(\boldsymbol{q}) \equiv I_{in}[f_s] - I_{out}[f_s], \end{aligned} \tag{B.9}$$

where in the rightmost term of Eq.(B.9) the collision term is decomposed into two parts, one related to inscattering and the other related to outscattering processes. Under thermal equilibrium conditions the inscattering and the outscattering processes should compensate each other leading to the result

$$w_{\boldsymbol{q'}\to\boldsymbol{q}}\left(f_s^0(\boldsymbol{q})+1\right)=w_{\boldsymbol{q}\to\boldsymbol{q'}}f_s^0(\boldsymbol{q}), \tag{B.10}$$

where $f_s^0(\boldsymbol{q})$ is the equilibrium distribution function. Assuming that the applied temperature gradient is such that the departure of the single-particle distribution function from its equilibrium value is small, i.e. $f_s(\boldsymbol{q})\approx f_s^0(\boldsymbol{q})+f_s^1(\boldsymbol{q})$, from Eqs.(B.9) and (B.10) to lowest order it is

$$\begin{aligned} I[f_s] &\approx -\left(\frac{1}{A}\sum_{\boldsymbol{q'}}\left(w_{\boldsymbol{q}\to\boldsymbol{q'}}-w_{\boldsymbol{q'}\to\boldsymbol{q}}\right)\right)f_s^1(\boldsymbol{q}) \\ &= -\left[\frac{1}{A}\sum_{\boldsymbol{q'}}\left(w_{\boldsymbol{q}\to\boldsymbol{q'}}-w_{\boldsymbol{q'}\to\boldsymbol{q}}\right)\right]\Big(f_s(\boldsymbol{q})-f_s^0(\boldsymbol{q})\Big), \end{aligned} \tag{B.11}$$

where we define the so-called *relaxation time* as below

$$\frac{1}{\tau_s(\boldsymbol{q})}=\frac{1}{A}\sum_{\boldsymbol{q'}}\left(w_{\boldsymbol{q}\to\boldsymbol{q'}}-w_{\boldsymbol{q'}\to\boldsymbol{q}}\right). \tag{B.12}$$

Notice that the result of Eq.(B.12) per unit area is directly related to Eqs.(2.40) and (2.41) that were derived in the phonon-dominated thermal transport regime. Notice also that the microscopic transition probabilities $w_{\boldsymbol{q}\to\boldsymbol{q'}}$ and $w_{\boldsymbol{q'}\to\boldsymbol{q}}$ do not necessarily balance each other (as happens in the problem of the elastic scattering of an electron from impurities), and more specifically, to ensure the *non-negativity* of the phonon relaxation time defined above it should

be true that $w_{\boldsymbol{q}\to\boldsymbol{q'}} \geq w_{\boldsymbol{q'}\to\boldsymbol{q}}$, and of course the quantity $\sum_{\boldsymbol{q'}} \left(w_{\boldsymbol{q}\to\boldsymbol{q'}} - w_{\boldsymbol{q'}\to\boldsymbol{q}}\right)$ should be bounded (not infinite). Under the aforementioned conditions, the weak interaction of phonons with the magnon bath (under a weak temperature gradient) can be described via the concept of the *phonon relaxation time*.

Combining Eqs.(B.7), (B.8), (B.11) and (B.12) we get (using again the approximation of $f_s(\boldsymbol{q}) \approx f_s^0(\boldsymbol{q}) + f_s^1(\boldsymbol{q})$)

$$\boldsymbol{v}_s(\boldsymbol{q}) \cdot \nabla T \frac{\partial f_s^0(\boldsymbol{q})}{\partial T} + \boldsymbol{v}_s(\boldsymbol{q}) \cdot \nabla T \frac{\partial f_s^1(\boldsymbol{q})}{\partial T} = -\frac{f_s^1(\boldsymbol{q})}{\tau_s(\boldsymbol{q})},$$

and neglecting on the LHS (left hand side) the term that depends on $f_s^1(\boldsymbol{q})$ (as being smaller compared to the other term on the LHS), to lowest order it is

$$f_s^1(\boldsymbol{q}) = -\tau_s(\boldsymbol{q}) \boldsymbol{v}_s(\boldsymbol{q}) \cdot \nabla T \frac{\partial f_s^0(\boldsymbol{q})}{\partial T},$$

or finally

$$f_s(\boldsymbol{q}) \approx f_s^0(\boldsymbol{q}) - \tau_s(\boldsymbol{q}) \boldsymbol{v}_s(\boldsymbol{q}) \cdot \nabla T \frac{\partial f_s^0(\boldsymbol{q})}{\partial T}. \tag{B.13}$$

Let us now connect the above results (of the stationary case) with the thermal conductivity tensor. The total heat current carried by phonons with single-particle distribution function $f_s(\boldsymbol{q})$, summing over all different phonon polarizations, is (adjusted to 2D)

$$\boldsymbol{j}_Q = \sum_s \int \frac{d^2\boldsymbol{q}}{(2\pi)^2} \hbar\omega_s(\boldsymbol{q}) \boldsymbol{v}_s(\boldsymbol{q}) f_s(\boldsymbol{q}). \tag{B.14}$$

Combining Eqs.(B.13) and (B.14) we find (the term containing the equilibrium distribution function of the phonons does not participate in the heat current

and is dropped)

$$\boldsymbol{j}_Q = -\sum_s \int \frac{d^2\boldsymbol{q}}{(2\pi)^2} \hbar\omega_s(\boldsymbol{q}) \boldsymbol{v}_s(\boldsymbol{q}) \tau_s(\boldsymbol{q}) \frac{\partial f_s^0(\boldsymbol{q})}{\partial T} \boldsymbol{v}_s(\boldsymbol{q}) \cdot \nabla T, \tag{B.15}$$

and recalling the definition of the thermal conductivity tensor κ via the Fourier law of heat transport (adjusted to a 2D system) which reads

$$\boldsymbol{j}_Q = -\kappa \nabla T, \tag{B.16}$$

we find for the *thermal conductivity tensor per unit area* the following expression (notice that in order to get the correct units we need to take into account the relaxation time per unit area as defined in Eq.(B.12))

$$\kappa_{\alpha\beta} = \sum_s \int \frac{d^2\boldsymbol{q}}{(2\pi)^2} \hbar\omega_s(\boldsymbol{q}) v_s^\alpha(\boldsymbol{q}) v_s^\beta(\boldsymbol{q}) \tau_s(\boldsymbol{q}) \frac{\partial f_s^0(\boldsymbol{q})}{\partial T}. \tag{B.17}$$

Before concluding this section, let us mention that all the aforementioned analysis can also be applied to magnons weakly interacting with a phonon bath, as happens in the magnon-dominated transport regime, of course with the appropriate modifications. The more general case in which both types of carriers participate significantly in the total thermal conductivity requires a more sophisticated treatment than the one given here.

Appendix C

Technical details for the computation of the line integrals of the various scattering rates

To calculate the line integrals (reduction comes upon using the property of the Dirac δ function mentioned in the main text) appearing in various scattering rates (magnonic or phononic), one needs to find the path of integration dictated by the energy conservation constraint. For instance, for the magnon scattering rates of the following general form

$$\left.\frac{1}{\tau_\lambda(\boldsymbol{k})}\right|_{mp} = \sum_{\lambda'} \int F(\boldsymbol{k},\boldsymbol{q},T)\delta(\epsilon_{\boldsymbol{k}\pm\boldsymbol{q},\lambda'} \pm \hbar\omega_{\boldsymbol{q}} \pm \epsilon_{\boldsymbol{k},\lambda})dl(\boldsymbol{q}), \tag{C.1}$$

for each given (k_x, k_y) point of interest, one needs to know all (q_x, q_y) points that satisfy the energy conservation constraint $\delta(\epsilon_{\boldsymbol{k}\pm\boldsymbol{q},\lambda'} \pm \hbar\omega_{\boldsymbol{q}} \pm \epsilon_{\boldsymbol{k},\lambda})$ first, and then perform the line-integral over these points numerically. Due to high non-linearity of the magnon dispersion relations simple analytical expressions are not possible. Thus, the energy constraint was graphically solved like this: For a specific temperature T, a grid of (k_x, k_y)-points were taken in the vicinity of the various magnon valleys, and for each one of those $\boldsymbol{k}$-points a contour plot of the energy constraint was created. From each contour plot, all the (q_x, q_y) points that satisfy the energy constraint for that fixed (k_x, k_y) point were extracted, and were then used to compute the reduced integral. This

way, the quantity $\frac{1}{\tau_\lambda(\boldsymbol{k},T)}$ for every (k_x, k_y)-point was calculated, and further, the whole previous calculation was repeated for each temperature of the chosen temperature window for this study. In the semiclassical Boltzmann approach to the thermal conductivity, the quantity $\frac{1}{\tau_\lambda(\boldsymbol{k},T)}$ enters within a second integral, this time over the magnon momentum space of interest (i.e. over the $\boldsymbol{k}$ space), whereby one finally gets the magnon thermal conductivity. A similar procedure is followed for the calculation of the phononic thermal conductivity.

As a last note, to get the constant energy surfaces for a fixed temperature value, for a given wavevector of the one quasiparticle type, the various points of the contour plot of the energy constraint were extracted using the following 'mathematica' command:

`List=Cases[Normal[ContourPlot_pic], Line[Data_]` $\rightarrow$ `Data,5]`.

Bibliography

[1] Robert Schaffer, Eric Kin-Ho Lee, Bohm-Jung Yang, and Yong Baek Kim, "Recent progress on correlated electron systems with strong spin-orbit coupling", arXiv:1512.02224.

[2] G. Bauer, E. Saitoh, and B. van Wees, Nat. Mat.11, 319(2012).

[3] Lucile Savary and T. Senthil, "Probing Hidden Orders with Resonant Inelastic X-Ray Scattering", arXiv:1506.04752.

[4] M. Xiao, "Theory of transformation for the diagonalization of quadratic Hamiltonians" (2009), arXiv:0908.0787v1.

[5] H. Adachi, K. ichi Uchida, E. Saitoh, and S. Maekawa. Theory of the spin seebeck effect. *Reports on Progress in Physics*, 76(3):036501, 2013.

[6] Z. Alpichshev, F. Mahmood, G. Cao, and N. Gedik. Confinement-deconfinement transition as an indication of spin-liquid-type behavior in na_2iro_3. *Phys. Rev. Lett.*, 114:017203, Jan 2015.

[7] L. J. P. Ament, M. van Veenendaal, T. P. Devereaux, J. P. Hill, and J. van den Brink. Resonant inelastic x-ray scattering studies of elementary excitations. *Rev. Mod. Phys.*, 83:705–767, Jun 2011.

[8] Y. Ando. Topological insulator materials. *Journal of the Physical Society of Japan*, 82(10):102001, 2013.

[9] N. W. Ashcroft and N. D. Mermin. *Solid State Physics*. Saunders College Publishing, Florida, 1976.

[10] A. Aurbach. *Interacting Electrons and Quantum Magnetism*. Soringer-Verlag, New York, 1994.

[11] J. G. Bednorz and K. A. Müller. Perovskite-type oxides¯the new approach to high-T_c superconductivity. *Rev. Mod. Phys.*, 60:585–600, Jul 1988.

[12] B. A. Bernevig, T. L. Hughes, and S.-C. Zhang. Quantum spin hall effect and topological phase transition in hgte quantum wells. *Science*, 314(5806):1757–1761, 2006.

[13] B. A. Bernevig and S.-C. Zhang. Quantum spin hall effect. *Phys. Rev. Lett.*, 96:106802, Mar 2006.

[14] A. Biffin, R. D. Johnson, S. Choi, F. Freund, S. Manni, A. Bombardi, P. Manuel, P. Gegenwart, and R. Coldea. Unconventional magnetic order on the hyperhoneycomb kitaev lattice in $\beta-\mathrm{li_2iro_3}$: Full solution via magnetic resonant x-ray diffraction. *Phys. Rev. B*, 90:205116, Nov 2014.

[15] S. Boseggia, R. Springell, H. C. Walker, H. M. Rønnow, C. Rüegg, H. Okabe, M. Isobe, R. S. Perry, S. P. Collins, and D. F. McMorrow. Ro-

bustness of basal-plane antiferromagnetic order and the J_{eff}=1/2 state in single-layer iridate spin-orbit mott insulators. *Phys. Rev. Lett.*, 110:117207, Mar 2013.

[16] J. c. v. Chaloupka, G. Jackeli, and G. Khaliullin. Kitaev-heisenberg model on a honeycomb lattice: Possible exotic phases in iridium oxides $A_2\text{iro}_3$. *Phys. Rev. Lett.*, 105:027204, Jul 2010.

[17] J. c. v. Chaloupka, G. Jackeli, and G. Khaliullin. Zigzag magnetic order in the iridium oxide na_2iro_3. *Phys. Rev. Lett.*, 110:097204, Feb 2013.

[18] L. C. Chapon and S. W. Lovesey. The magnetic motif and the wave-function of kramers ions in strontium iridate (sr 2 iro 4). *Journal of Physics: Condensed Matter*, 23(25):252201, 2011.

[19] Q. Chen, H.-H. Hung, X. Hu, and G. A. Fiete. Correlation effects in pyrochlore iridate thin films grown along the [111] direction. *Phys. Rev. B*, 92:085145, Aug 2015.

[20] G.-W. Chern, Y. Sizyuk, C. Price, and N. B. Perkins. Kitaev-heisenberg model in a magnetic field: Order-by-disorder and commensurate-incommensurate transitions. *Phys. Rev. B*, 95:144427, Apr 2017.

[21] A. L. Chernyshev and W. Brenig. Thermal conductivity in large $-j$ two-dimensional antiferromagnets: Role of phonon scattering. *Phys. Rev. B*, 92:054409, Aug 2015.

[22] A. L. Chernyshev and A. V. Rozhkov. Heat transport in spin chains with weak spin-phonon coupling. *Phys. Rev. Lett.*, 116:017204, Jan 2016.

[23] S. K. Choi, R. Coldea, A. N. Kolmogorov, T. Lancaster, I. I. Mazin, S. J. Blundell, P. G. Radaelli, Y. Singh, P. Gegenwart, K. R. Choi, S.-W. Cheong, P. J. Baker, C. Stock, and J. Taylor. Spin waves and revised crystal structure of honeycomb iridate na_2iro_3. *Phys. Rev. Lett.*, 108:127204, Mar 2012.

[24] J. P. Clancy, N. Chen, C. Y. Kim, W. F. Chen, K. W. Plumb, B. C. Jeon, T. W. Noh, and Y.-J. Kim. Spin-orbit coupling in iridium-based $5d$ compounds probed by x-ray absorption spectroscopy. *Phys. Rev. B*, 86:195131, Nov 2012.

[25] A. M. Cook, S. Matern, C. Hickey, A. A. Aczel, and A. Paramekanti. Spin-orbit coupled $j_{\text{eff}} = 1/2$ iridium moments on the geometrically frustrated fcc lattice. *Phys. Rev. B*, 92:020417, Jul 2015.

[26] T. Dietl and H. Ohno. Dilute ferromagnetic semiconductors: Physics and spintronic structures. *Rev. Mod. Phys.*, 86:187–251, Mar 2014.

[27] G. S. Dixon. Lattice thermal conductivity of antiferromagnetic insulators. *Phys. Rev. B*, 21:2851–2864, Apr 1980.

[28] P. Fazekas. *Lecture notes on electron correlation and magnetism*. World scientific, 1999.

[29] K. Foyevtsova, H. O. Jeschke, I. I. Mazin, D. I. Khomskii, and R. Valentí. Ab initio. *Phys. Rev. B*, 88:035107, Jul 2013.

[30] J. S. Gardner, M. J. P. Gingras, and J. E. Greedan. Magnetic pyrochlore oxides. *Rev. Mod. Phys.*, 82:53–107, Jan 2010.

[31] A. Go, W. Witczak-Krempa, G. S. Jeon, K. Park, and Y. B. Kim. Correlation effects on 3d topological phases: From bulk to boundary. *Phys. Rev. Lett.*, 109:066401, Aug 2012.

[32] H. Gretarsson, N. H. Sung, J. Porras, J. Bertinshaw, C. Dietl, J. A. N. Bruin, A. F. Bangura, Y. K. Kim, R. Dinnebier, J. Kim, A. Al-Zein, M. Moretti Sala, M. Krisch, M. Le Tacon, B. Keimer, and B. J. Kim. Persistent paramagnons deep in the metallic phase of $\mathrm{sr}_{2-x}\mathrm{la}_x\mathrm{iro}_4$. *Phys. Rev. Lett.*, 117:107001, Sep 2016.

[33] R. Hanson, L. P. Kouwenhoven, J. R. Petta, S. Tarucha, and L. M. K. Vandersypen. Spins in few-electron quantum dots. *Rev. Mod. Phys.*, 79:1217–1265, Oct 2007.

[34] M. Z. Hasan and C. L. Kane. Colloquium. *Rev. Mod. Phys.*, 82:3045–3067, Nov 2010.

[35] D. Haskel, G. Fabbris, M. Zhernenkov, P. P. Kong, C. Q. Jin, G. Cao, and M. van Veenendaal. Pressure tuning of the spin-orbit coupled ground state in $\mathrm{sr}_2\mathrm{iro}_4$. *Phys. Rev. Lett.*, 109:027204, Jul 2012.

[36] L. Hozoi, H. Gretarsson, J. P. Clancy, B.-G. Jeon, B. Lee, K. H. Kim, V. Yushankhai, P. Fulde, D. Casa, T. Gog, J. Kim, A. H. Said, M. H. Upton, Y.-J. Kim, and J. van den Brink. Longer-range lattice anisotropy strongly competing with spin-orbit interactions in pyrochlore iridates. *Phys. Rev. B*, 89:115111, Mar 2014.

[37] X. Hu, Z. Zhong, and G. A. Fiete. First principles prediction of topological phases in thin films of pyrochlore iridates. *Scientific Reports*, 5(11072), 2015.

[38] I. Žutić, J. Fabian, and S. Das Sarma. Spintronics: Fundamentals and applications. *Rev. Mod. Phys.*, 76:323–410, Apr 2004.

[39] M. Imada, A. Fujimori, and Y. Tokura. Metal-insulator transitions. *Rev. Mod. Phys.*, 70:1039–1263, Oct 1998.

[40] G. Jackeli and G. Khaliullin. Mott insulators in the strong spin-orbit coupling limit: From heisenberg to a quantum compass and kitaev models. *Phys. Rev. Lett.*, 102:017205, Jan 2009.

[41] H.-C. Jiang, Z.-C. Gu, X.-L. Qi, and S. Trebst. Possible proximity of the mott insulating iridate na_2iro_3 to a topological phase: Phase diagram of the heisenberg-kitaev model in a magnetic field. *Phys. Rev. B*, 83:245104, Jun 2011.

[42] C. L. Kane and E. J. Mele. Quantum spin hall effect in graphene. *Phys. Rev. Lett.*, 95:226801, Nov 2005.

[43] C. L. Kane and E. J. Mele. Z_2. *Phys. Rev. Lett.*, 95:146802, Sep 2005.

[44] M. Kargarian and G. A. Fiete. Topological crystalline insulators in transition metal oxides. *Phys. Rev. Lett.*, 110:156403, Apr 2013.

[45] M. Kargarian, A. Langari, and G. A. Fiete. Unusual magnetic phases in the strong interaction limit of two-dimensional topological band insulators in transition metal oxides. *Phys. Rev. B*, 86:205124, Nov 2012.

[46] M. Kargarian, J. Wen, and G. A. Fiete. Competing exotic topological insulator phases in transition-metal oxides on the pyrochlore lattice with distortion. *Phys. Rev. B*, 83:165112, Apr 2011.

[47] V. M. Katukuri. "quantum chemical approach to spinorbit excitations and magnetic interactions in iridium oxides", (2014),PhD Thesis, Techniche Universitat Dresden.

[48] V. M. Katukuri, S. Nishimoto, V. Yushankhai, A. Stoyanova, H. Kandpal, S. Choi, R. Coldea, I. Rousochatzakis, L. Hozoi, and J. van den Brink. Kitaev interactions between j = 1/2 moments in honeycomb na 2 iro 3 are large and ferromagnetic: insights from ab initio quantum chemistry calculations. *New Journal of Physics*, 16(1):013056, 2014.

[49] V. M. Katukuri, K. Roszeitis, V. Yushankhai, A. Mitrushchenkov, H. Stoll, M. van Veenendaal, P. Fulde, J. van den Brink, and L. Hozoi. Electronic structure of low-dimensional 4d5 oxides: Interplay of ligand distortions,

overall lattice anisotropy, and spin–orbit interactions. *Inorganic Chemistry*, 53(10):4833–4839, 2014. PMID: 24779549.

[50] V. M. Katukuri, H. Stoll, J. van den Brink, and L. Hozoi. Ab initio. *Phys. Rev. B*, 85:220402, Jun 2012.

[51] V. M. Katukuri, V. Yushankhai, L. Siurakshina, J. van den Brink, L. Hozoi, and I. Rousochatzakis. Mechanism of basal-plane antiferromagnetism in the spin-orbit driven iridate ba_2iro_4. *Phys. Rev. X*, 4:021051, Jun 2014.

[52] B. H. Kim, G. Khaliullin, and B. I. Min. Electronic excitations in the edge-shared relativistic mott insulator: na_2iro_3. *Phys. Rev. B*, 89:081109, Feb 2014.

[53] B. J. Kim, H. Jin, S. J. Moon, J.-Y. Kim, B.-G. Park, C. S. Leem, J. Yu, T. W. Noh, C. Kim, S.-J. Oh, J.-H. Park, V. Durairaj, G. Cao, and E. Rotenberg. Novel $J_{\text{eff}} = 1/2$ mott state induced by relativistic spin-orbit coupling in sr_2iro_4. *Phys. Rev. Lett.*, 101:076402, Aug 2008.

[54] B. J. Kim, H. Ohsumi, T. Komesu, S. Sakai, T. Morita, H. Takagi, and T. Arima. Phase-sensitive observation of a spin-orbital mott state in sr2iro4. *Science*, 323(5919):1329–1332, 2009.

[55] J. Kim, D. Casa, M. H. Upton, T. Gog, Y.-J. Kim, J. F. Mitchell, M. van Veenendaal, M. Daghofer, J. van den Brink, G. Khaliullin, and B. J. Kim. Magnetic excitation spectra of sr_2iro_4 probed by resonant inelastic x-ray

scattering: Establishing links to cuprate superconductors. *Phys. Rev. Lett.*, 108:177003, Apr 2012.

[56] J. Kim, A. H. Said, D. Casa, M. H. Upton, T. Gog, M. Daghofer, G. Jackeli, J. van den Brink, G. Khaliullin, and B. J. Kim. Large spin-wave energy gap in the bilayer iridate $sr_3ir_2o_7$: Evidence for enhanced dipolar interactions near the mott metal-insulator transition. *Phys. Rev. Lett.*, 109:157402, Oct 2012.

[57] I. Kimchi, R. Coldea, and A. Vishwanath. Unified theory of spiral magnetism in the harmonic-honeycomb iridates α, β, and γ li_2iro_3. *Phys. Rev. B*, 91:245134, Jun 2015.

[58] A. Kitaev. Anyons in an exactly solved model and beyond. *Annals of Physics*, 321(1):2 – 111, 2006. January Special Issue.

[59] J. Knolle, G.-W. Chern, D. L. Kovrizhin, R. Moessner, and N. B. Perkins. Raman scattering signatures of kitaev spin liquids in A_2iro_3 iridates with $a =$ Na or li. *Phys. Rev. Lett.*, 113:187201, Oct 2014.

[60] A. Kotani and S. Shin. Resonant inelastic x-ray scattering spectra for electrons in solids. *Rev. Mod. Phys.*, 73:203–246, Feb 2001.

[61] M. A. Laguna-Marco, D. Haskel, N. Souza-Neto, J. C. Lang, V. V. Krishnamurthy, S. Chikara, G. Cao, and M. van Veenendaal. Orbital magnetism and spin-orbit effects in the electronic structure of $bairo_3$. *Phys. Rev. Lett.*, 105:216407, Nov 2010.

[62] P. Laurell and G. A. Fiete. Topological magnon bands and unconventional superconductivity in pyrochlore iridate thin films. *Phys. Rev. Lett.*, 118:177201, Apr 2017.

[63] E. K.-H. Lee, J. G. Rau, and Y. B. Kim. Two iridates, two models, and two approaches: A comparative study on magnetism in three-dimensional honeycomb materials. *Phys. Rev. B*, 93:184420, May 2016.

[64] P. A. Lee, N. Nagaosa, and X.-G. Wen. Doping a mott insulator: Physics of high-temperature superconductivity. *Rev. Mod. Phys.*, 78:17–85, Jan 2006.

[65] S. Y. Li, L. Taillefer, C. H. Wang, and X. H. Chen. Ballistic magnon transport and phonon scattering in the antiferromagnet nd_2cuo_4. *Phys. Rev. Lett.*, 95:156603, Oct 2005.

[66] S. W. Lovesey and A. N. Dobrynin. Magnetic correlations in a layered iridate, na 2 iro 3. *Journal of Physics: Condensed Matter*, 24(38):382201, 2012.

[67] X. Lu, D. E. McNally, M. Moretti Sala, J. Terzic, M. H. Upton, D. Casa, G. Ingold, G. Cao, and T. Schmitt. Doping evolution of magnetic order and magnetic excitations in $(sr_{1-x}la_x)_3ir_2o_7$. *Phys. Rev. Lett.*, 118:027202, Jan 2017.

[68] J. Maciejko and G. A. Fiete. Fractionalized topological insulators. *Nat. Phys.*, 11:385, 2015.

[69] S. Maekawa, T. Tohyama, S. E. Barnes, and I. S. *Physics of Transition Metal Oxides*. Springer, Berlin, 2004.

[70] G. Mahan. *Many-Particle Physics*. Kluwer/Plenum, New York, 2000.

[71] H. Matsuura and K. Miyake. Effect of spin–orbit interaction on (4d)3- and (5d)3-based transition-metal oxides. *Journal of the Physical Society of Japan*, 82(7):073703, 2013.

[72] I. I. Mazin, H. O. Jeschke, K. Foyevtsova, R. Valentí, and D. I. Khomskii. na_2iro_3. *Phys. Rev. Lett.*, 109:197201, Nov 2012.

[73] O. N. Meetei, W. S. Cole, M. Randeria, and N. Trivedi. Novel magnetic state in d^4 mott insulators. *Phys. Rev. B*, 91:054412, Feb 2015.

[74] I. Mikhail, I. Ismail, and M. Ameen. Exact and model operators for magnon–phonon interactions in antiferromagnets. *Physica B: Condensed Matter*, 406(3):508 – 515, 2011.

[75] I. Mikhail, I. Ismail, and M. Ameen. Model calculation of thermal conductivity in antiferromagnets. *Physica B: Condensed Matter*, 476(Supplement C):29 – 36, 2015.

[76] S. Mohapatra, J. van den Brink, and A. Singh. Magnetic excitations in a three-orbital model for the strongly spin-orbit coupled iridates: Effect of mixing between the $j = \frac{1}{2}$ and $\frac{3}{2}$ sectors. *Phys. Rev. B*, 95:094435, Mar 2017.

[77] J. E. Moore. The birth of topological insulators. *Nature*, 464:194–198, 2010.

[78] M. Moretti Sala, S. Boseggia, D. F. McMorrow, and G. Monaco. Resonant x-ray scattering and the j_{eff}=1/2 electronic ground state in iridate perovskites. *Phys. Rev. Lett.*, 112:026403, Jan 2014.

[79] M. Moretti Sala, V. Schnells, S. Boseggia, L. Simonelli, A. Al-Zein, J. G. Vale, L. Paolasini, E. C. Hunter, R. S. Perry, D. Prabhakaran, A. T. Boothroyd, M. Krisch, G. Monaco, H. M. Rønnow, D. F. McMorrow, and F. Mila. Evidence of quantum dimer excitations in $sr_3ir_2o_7$. *Phys. Rev. B*, 92:024405, Jul 2015.

[80] N. B. Perkins, Y. Sizyuk, and P. Wölfle. Interplay of many-body and single-particle interactions in iridates and rhodates. *Phys. Rev. B*, 89:035143, Jan 2014.

[81] D. Pesin and L. Balents. Mott physics and band topology in materials with strong spin–orbit interaction. *Nat. Phys.*, 6:376, 2010.

[82] N. Pottier. *Nonequilibrium Statistical Physics*. Oxford university press, 2014.

[83] X.-L. Qi and S.-C. Zhang. Topological insulators and superconductors. *Rev. Mod. Phys.*, 83:1057–1110, Oct 2011.

[84] J. G. Rau, E. K.-H. Lee, and H.-Y. Kee. Generic spin model for the honeycomb iridates beyond the kitaev limit. *Phys. Rev. Lett.*, 112:077204, Feb 2014.

[85] J. G. Rau, E. K.-H. Lee, and H.-Y. Kee. Spin-orbit physics giving rise to novel phases in correlated systems: Iridates and related materials. *Annual Review of Condensed Matter Physics*, 7(1):195–221, 2016.

[86] J. Reuther, R. Thomale, and S. Rachel. Magnetic ordering phenomena of interacting quantum spin hall models. *Phys. Rev. B*, 86:155127, Oct 2012.

[87] I. Rousochatzakis, J. Reuther, R. Thomale, S. Rachel, and N. B. Perkins. Phase diagram and quantum order by disorder in the kitaev $K_1 - K_2$ honeycomb magnet. *Phys. Rev. X*, 5:041035, Dec 2015.

[88] R. Schaffer, E. K.-H. Lee, B.-J. Yang, and Y. B. Kim. Recent progress on correlated electron systems with strong spin–orbit coupling. *Reports on Progress in Physics*, 79(9):094504, 2016.

[89] A. Shitade, H. Katsura, J. Kuneš, X.-L. Qi, S.-C. Zhang, and N. Nagaosa. Quantum spin hall effect in a transition metal oxide na_2iro_3. *Phys. Rev. Lett.*, 102:256403, Jun 2009.

[90] Y. Singh, S. Manni, J. Reuther, T. Berlijn, R. Thomale, W. Ku, S. Trebst, and P. Gegenwart. Relevance of the heisenberg-kitaev model for the

honeycomb lattice iridates $A_2\mathrm{iro}_3$. *Phys. Rev. Lett.*, 108:127203, Mar 2012.

[91] Y. Sizyuk, C. Price, P. Wölfle, and N. B. Perkins. Importance of anisotropic exchange interactions in honeycomb iridates: Minimal model for zigzag antiferromagnetic order in $\mathrm{na}_2\mathrm{iro}_3$. *Phys. Rev. B*, 90:155126, Oct 2014.

[92] J. Sólyom. *Fundamentals of the physics of solids, Vol.1, Structure and dynamics*. Springer, Berlin Heidelberg, 2007.

[93] G. L. Stamokostas, P. E. Lapas, and G. A. Fiete. Thermal conductivity of local moment models with strong spin-orbit coupling. *Phys. Rev. B*, 95:064410, Feb 2017.

[94] Steckel, F., Matsumoto, A., Takayama, T., Takagi, H., Büchner, B., and Hess, C. Pseudospin transport in the jeff = 1/2 antiferromagnet sr2iro4. *EPL*, 114(5):57007, 2016.

[95] S. Sugano, Y. Tanabe, and H. Kamimura. *Multiplets of transition-metal ions in crystals*. Academic Press, 1970.

[96] C. Svoboda, M. Randeria, and N. Trivedi. Effective magnetic interactions in spin-orbit coupled d^4 mott insulators. *Phys. Rev. B*, 95:014409, Jan 2017.

[97] T. Takayama, A. Kato, R. Dinnebier, J. Nuss, H. Kono, L. S. I. Veiga, G. Fabbris, D. Haskel, and H. Takagi. Hyperhoneycomb iridate $\beta-\mathrm{li}_2\mathrm{iro}_3$

as a platform for kitaev magnetism. *Phys. Rev. Lett.*, 114:077202, Feb 2015.

[98] B. T. Thole and G. van der Laan. Branching ratio in x-ray absorption spectroscopy. *Phys. Rev. B*, 38:3158–3171, Aug 1988.

[99] B. T. Thole and G. van der Laan. Linear relation between x-ray absorption branching ratio and valence-band spin-orbit expectation value. *Phys. Rev. A*, 38:1943–1947, Aug 1988.

[100] Y. Tokura and N. Nagaosa. Orbital physics in transition-metal oxides. *Science*, 288(5465):462–468, 2000.

[101] Y. Tserkovnyak, A. Brataas, G. E. W. Bauer, and B. I. Halperin. Nonlocal magnetization dynamics in ferromagnetic heterostructures. *Rev. Mod. Phys.*, 77:1375–1421, Dec 2005.

[102] K. Uchida, M. Ishida, T. Kikkawa, A. Kirihara, T. Murakami, and E. Saitoh. Longitudinal spin seebeck effect: from fundamentals to applications. *Journal of Physics: Condensed Matter*, 26(34):343202, 2014.

[103] G. van der Laan and B. T. Thole. Local probe for spin-orbit interaction. *Phys. Rev. Lett.*, 60:1977–1980, May 1988.

[104] S. W, D. D. Khalyavin, P. Manuel, L. C. Chapon, G. Cao, and T. F. Qi. Magnetic symmetries in neutron and resonant x-ray bragg diffraction patterns of four iridium oxides. *Journal of Physics: Condensed Matter*, 24(49):496003, 2012.

[105] X. Wan, A. M. Turner, A. Vishwanath, and S. Y. Savrasov. Topological semimetal and fermi-arc surface states in the electronic structure of pyrochlore iridates. *Phys. Rev. B*, 83:205101, May 2011.

[106] S. C. Williams, R. D. Johnson, F. Freund, S. Choi, A. Jesche, I. Kimchi, S. Manni, A. Bombardi, P. Manuel, P. Gegenwart, and R. Coldea. Incommensurate counterrotating magnetic order stabilized by kitaev interactions in the layered honeycomb $\alpha-\mathrm{li_2iro_3}$. *Phys. Rev. B*, 93:195158, May 2016.

[107] W. Witczak-Krempa, G. Chen, Y. B. Kim, and L. Balents. Correlated quantum phenomena in the strong spin-orbit regime. *Annual Review of Condensed Matter Physics*, 5(1):57–82, 2014.

[108] W. Witczak-Krempa and Y. B. Kim. Topological and magnetic phases of interacting electrons in the pyrochlore iridates. *Phys. Rev. B*, 85:045124, Jan 2012.

[109] L. M. Woods. Magnon-phonon effects in ferromagnetic manganites. *Phys. Rev. B*, 65:014409, Nov 2001.

[110] Y. Yamaji, Y. Nomura, M. Kurita, R. Arita, and M. Imada. First-principles study of the honeycomb-lattice iridates $\mathrm{na_2iro_3}$ in the presence of strong spin-orbit interaction and electron correlations. *Phys. Rev. Lett.*, 113:107201, Sep 2014.

[111] B. Yuan, J. P. Clancy, A. M. Cook, C. M. Thompson, J. Greedan, G. Cao, B. C. Jeon, T. W. Noh, M. H. Upton, D. Casa, T. Gog, A. Paramekanti, and Y.-J. Kim. Determination of hund's coupling in $5d$ oxides using resonant inelastic x-ray scattering. *Phys. Rev. B*, 95:235114, Jun 2017.

[112] H. Zeiger and G. Pratt. *Magnetic interactions in solids.* Oxford university press, 1973.

[113] H. Zhang, K. Haule, and D. Vanderbilt. Effective j=1/2 insulating state in ruddlesden-popper iridates: An LDA+DMFT study. *Phys. Rev. Lett.*, 111:246402, Dec 2013.

[114] H. Zhang, K. Haule, and D. Vanderbilt. Metal-insulator transition and topological properties of pyrochlore iridates. *Phys. Rev. Lett.*, 118:026404, Jan 2017.